Research Partnership to Secure Energy for America

RPSEA

Phase I Final Report

10121-4204-01.Final1

Corrosion and Scale at Extreme Temperature and Pressure

10121-4204-01

September 16, 2013

Mason Tomson, Ph.D., P.E.
Principal Investigator
Brine Chemistry Solutions LLC
8285 El Rio Street, Suite 100
Houston, TX 77054

LEGAL NOTICE

This report was prepared *by Brine Chemistry Solutions LLC a*s an account of work sponsored by the Research Partnership to Secure Energy for America, RPSEA. Neither RPSEA members of RPSEA, the National Energy Technology Laboratory, the U.S. Department of Energy, nor any person acting on behalf of any of the entities:

a. MAKES ANY WARRANTY OR REPRESENTATION, EXPRESS OR IMPLIED WITH RESPECT TO ACCURACY, COMPLETENESS, OR USEFULNESS OF THE INFORMATION CONTAINED IN THIS DOCUMENT, OR THAT THE USE OF ANY INFORMATION, APPARATUS, METHOD, OR PROCESS DISCLOSED IN THIS DOCUMENT MAY NOT INFRINGE PRIVATELY OWNED RIGHTS, OR

b. ASSUMES ANY LIABILITY WITH RESPECT TO THE USE OF, OR FOR ANY AND ALL DAMAGES RESULTING FROM THE USE OF, ANY INFORMATION, APPARATUS, METHOD, OR PROCESS DISCLOSED IN THIS DOCUMENT.

THIS IS AN INTERIM REPORT. THEREFORE, ANY DATA, CALCULATIONS, OR CONCLUSIONS REPORTED HEREIN SHOULD BE TREATED AS PRELIMINARY.

REFERENCE TO TRADE NAMES OR SPECIFIC COMMERCIAL PRODUCTS, COMMODITIES, OR SERVICES IN THIS REPORT DOES NOT REPRESENT OR CONSTIITUTE AND ENDORSEMENT, RECOMMENDATION, OR FAVORING BY RPSEA OR ITS CONTRACTORS OF THE SPECIFIC COMMERCIAL PRODUCT, COMMODITY, OR SERVICE.

ABSTRACT

Brine Chemistry Solutions (BCS) and Rice University (Rice) performed work under this contract to develop reliable methodologies, evaluate different techniques, test various steel materials, and integrate prediction models for corrosion and scale at extreme high pressure and temperature conditions (xHPHT), up to 250 °C and 24,000 psig. In Phase I, experimental data and information was obtained to improve the capability of corrosion and scale predictive modeling and to mitigate environmental risk, human safety, and production security of the Gulf of Mexico (GOM). This report details the feasibility of the proposed test equipment and techniques for corrosion and scale research at xHPHT. Phase II of this project will continue to acquire reliable experimental data with more metal alloys, flow conditions, and additional solid phases, and expand predictive models for continuing research and data acquisition on corrosion, scale formation, and inhibition.

This report begins with an overview of the problems facing ultra deepwater (UDW) oil and gas production in GOM. Following are descriptions of research tasks proposed in the Scope of Work for Phase I of this project. Task 6.0 discusses preliminary investigation of new testing for corrosion and scale at xHPHT conditions. HPHT corrosion testing in both an autoclave reactor and flow-through apparatus are discussed along with the development of scale solubility testing in a flow-through apparatus. The methodology developed for applying vertical scanning interferometry (VSI) to corrosion and scale study is then discussed. Task 7.0 demonstrated modeling of the equation of state (EoS) based on statistical associating fluids theory (SAFT) by mean spherical approximation (MSA). Followed by the discussion and validation of activity coefficient data for carbonates (i.e. $CaCO_3$, $FeCO_3$) experimentally obtained at various xHPHT and high total dissolved solids (TDS) conditions. The advancement in EoS modeling helps develop a thermodynamic model for predicting phase behavior of brine-hydrocarbon-acid-gas system at xHPHT conditions. Phase I goals were met and the project is on track to accomplish Phase II goals to add to GOM oil and gas production security through accurate corrosion and scale prediction and prevention.

SIGNATURE AND DATE STAMP

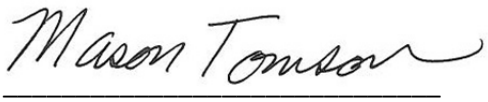

September 16, 2013

Mason Tomson, Principal Investigator Date

THIS PAGE INTENTIONALLY LEFT BLANK

Contents

EXECUTIVE SUMMARY

The goal of this project is to predict and prevent scale and corrosion at extreme high pressure and temperature (xHPHT) to improve the environmental risk, human safety, and production security of Gulf of Mexico (GOM) ultra deepwater oil and gas production. In Phase I of this project, Brine Chemistry Solutions (BCS) collected experimental scaling and corrosion data at xHPHT up to 250 °C and 24,000 psig and teamed with Rice University (Rice) performing thermodynamic and kinetic modeling. In Phase II, BCS and Rice will expand on Phase I's progress to include xHPHT experimental testing of corrosion and scale in complex brine systems, additional alloy types, inhibitor testing, and model refinement.

In Phase I, BCS conducted experiments using unique instrumentation and surface measuring techniques to study corrosion and scaling at xHPHT. To fully assess corrosion at xHPHT conditions, BCS developed new methodology by combining imaging techniques such as vertical scanning interferometry (VSI) with HPHT electrochemistry probe data from autoclave experiments, ICP solution measurements, and weight loss. Experimental research up to 24,000 psig and 250 °C was performed using a novel Hastelloy C-276 dynamic flow-through apparatus built in-lab and with a custom-designed Hastelloy C-276 autoclave reactor. These experiments resulted in new methodology and data that will be expanded upon in Phase II to further develop scale and corrosion models.

BCS performed corrosion testing and analysis on seven alloys in Phase I at temperatures up to 250 °C, salinities up to 6 M (29.85 wt%) NaCl, and various CO_2 concentrations. This full report details corrosion rate and surface morphology measurements performed on commonly used oil and gas production alloys under various high temperature conditions. The alloys of interest and analog fluid compositions were selected from recommendations by BCS's Working Project Group, consisting of eighteen oil and gas operators and service companies. In Phase II, BCS will continue to study various alloy systems under different fluid compositions at xHPHT to further simulate realistic scale and corrosion effects in UDW production up to 24,000 psig and 250 °C. Inhibitor assay methods were also started in Phase I, and inhibitor thermal stability and treatment methodology will continue into Phase II.

To assess scale prediction at xHPHT, BCS experimentally obtained solubility measurements between the range of 100 °C to 250 °C and 10,000 psig to 24,000 psig with salt concentrations that represent GOM UDW oil and gas production wells. Phase I focused on xHPHT equipment design and obtaining preliminary results with $CaCO_3$ and simple salt systems. In Phase II, other systems of interest will be studied such as $BaSO_4$, $FeCO_3$, FeS, and Fe_3O_4 scales and inhibitors with various brine compositions. Scale and corrosion tendencies of these systems at xHPHT are currently unknown and this project will allow for their accurate measurement and prediction.

In addition to xHPHT experimental work in scale and corrosion, Rice advanced the equation of state (EoS) modeling based on statistical associating fluids theory (SAFT) by including mean spherical approximation (MSA). This advancement helped develop a thermodynamic model for predicting phase behavior of brine-hydrocarbon-acid gas systems at xHPHT. In Phase II, modeling will specifically focus on understanding the solvent behavior in mixed electrolytes containing Ca^{2+}, Na^{+}, Ba^{2+}, Cl^{-}, SO_4^{2-}, CO_3^{2-}, S_2^{-} and others. In Phase II, modeling will expand to include the water-ion and ion-ion interaction with efforts focused towards quantifying kinetic factors such as diffusion coefficients. BCS and Rice request to proceed to Phase II as outlined in the Statement of Work, contract, and Project Management Plan, both in terms of technical content and funding.

OVERVIEW

The Gulf of Mexico (GOM) contains hundreds of oil and gas production wells. As seen below in Figure 1 oil and gas production spans a large part of the Gulf coast, and is a critical component to the energy infrastructure of the United States.

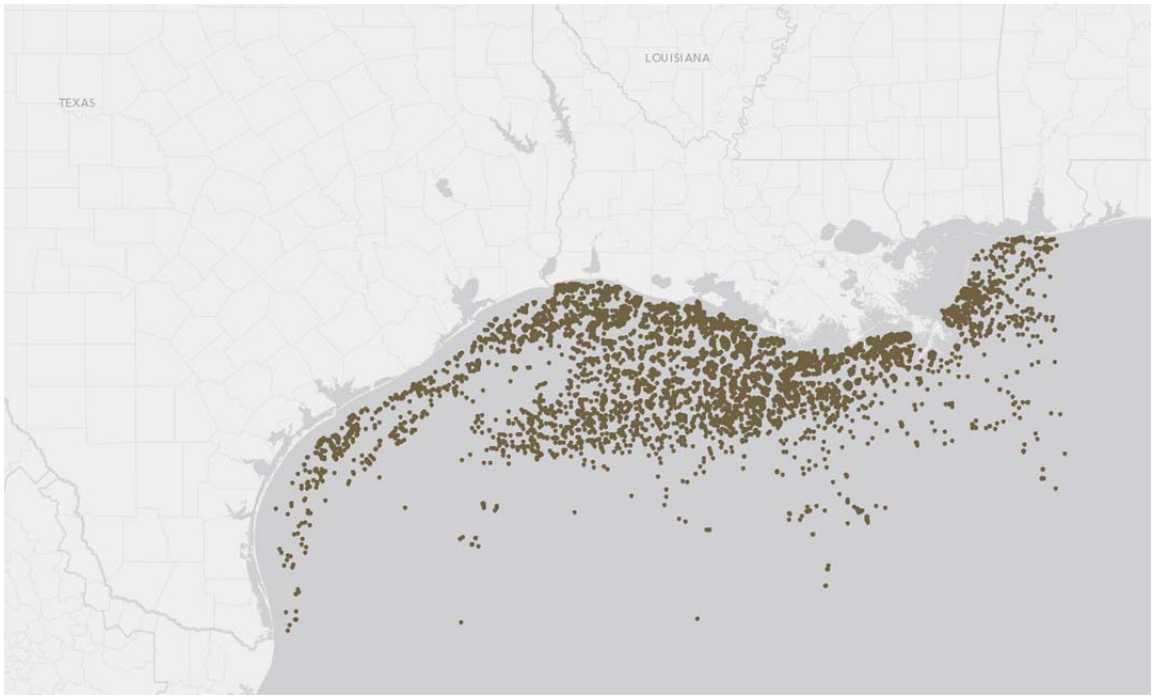

Figure 1. Gulf of Mexico production wells. Source: EIA.gov.

At least for the next thirty years there is little doubt of two trends in energy use, first that oil and gas will continue to be at the core of our energy mix, and second that production will continue to be from more and more hostile conditions of pressure, temperature, and fluid compositions. Unanticipated scale formation or corrosion has been known to stop production quickly. For example if a formation at 171 °C (340 °F) and 7,000 psig is in equilibrium with halite salt in a salt dome and the temperature drops to 115 °C (240 °F) in the tubing, as much as 11,000 pounds of salt are expected to precipitate from only 1,000 barrels of produced water. If corrosion were to break through tubing in an offshore well and expose the casing and cement to the extreme high pressures and temperatures of the formation, the economic damage could be enormous and the environmental impact disastrous. The deeper plays in the GOM are projected to exceed 200 °C (392 °F) and 20,000 psig and will likely contain considerable carbon dioxide and hydrogen sulfide. The oil and gas industry has spent years understanding scale, corrosion, and fluid properties, generally up to about 150 °C (302 °F) and 7,000 to 10,000 psig, with limited work being done to higher temperatures and pressures. Often, these upper limits of typical testing are related to equipment limitations, e.g. most autoclaves can reach the necessary temperature but are limited to only 3,000 psi and most flow-through equipment has been limited to circa 7,000 psig, as developed in the high performance liquid chromatography industry for analytical chemistry. Similarly, for modeling of the gas/oil/salt-water mix the literature is mostly related to these lower pressure and temperature conditions. It is known that many of the accepted theoretical frameworks, such as Peng-

Robinson-like equation of state (EoS) models and Pitzer activity coefficients are reaching their limits of expected application and new methods are needed. Finally, even less is known about the rate of scale formation and corrosion in any of these extreme conditions and little is known about the stability and effect of scale and corrosion inhibitors at these pressures, temperatures, and flow rates and the critical interplay of scale and corrosion inhibitors with specific metallurgies.

The overall objective of this research is to bridge this gap of testing and theory from the present common practice to the temperature, pressure, and conditions needed in next generation of oil and gas production in America. After examining the SPE and NACE literature, talking to many engineers in production companies, surveying available equipment, and comparing the expected breaks in physical and chemical properties, the upper temperature and pressure limits of 250 °C (482 °F) and 24,000 psig were agreed upon as being just higher than expected for onshore and offshore production for many years. The researchers at BCS and Rice University are experienced in testing and modeling fluids, etc., in the temperature and pressure regions now being used, about 150 °C (302 °F) and 7,000 psig, and below. In addition, some preliminary work has been done at Rice University to the higher limits, suggesting the feasibility of accomplishing the project goals. Finally, after examining the various surface analysis methods vertical scanning interferometry (VSI) was selected as a likely method to characterize corrosion, pitting, and scale rapidly and with minimal effort. Therefore, VSI is being tested in cooperation with the manufacturer, Bruker Instruments, for use in routine corrosion and pitting measurements.

In order to accomplish the goals of developing, testing, and modeling needed for the next generation of xHPHT scale formation, corrosion, inhibition, and fluids modeling the overall problem has been broken down into project tasks, accomplished in Phase I:

- Task 1.0 – Project Management Plan
- Task 2.0 – Technology Status Assessment
- Task 3.0 – Technology Transfer Plan
- Task 4.0 – Reports and Special Items
- Task 5.0 – Literature Review on xHPHT Corrosion and Scale Advances
- Task 6.0 – Preliminary investigation of new testing designs
- Task 6.1 – Develop the methodology to study corrosion coupons by various surface instruments, such as AFM, TEM, SEM, EDS, and VSI
- Task 7.1 – Validate Activity Coefficients for Carbonates at Various HPHT And TDS Condition
- Task 7.2 – Equation of State Development
- Task 8.0 – Phase I Report (this document)

Tasks 1 - 3 were completed in the first month of this project, while Task 4.0 is continuously ongoing during the entire project's period of performance. A comprehensive literature review was completed for Task 5.0 and was distributed to our working project group members. Task 5.0 literature review results are incorporated into the other sections and have served as the basis for some of the experimental and modeling approach taken in this project. Tasks 6.0, 6.1, 7.1, and 7.2 are discussed in detail in the rest of this report.

SUBTASK 6.0 - PRELIMINARY INVESTIGATION OF NEW TESTING

Summary

In Phase I of the project, as proposed for Task 6.0, Brine Chemistry Solutions built a high temperature, high pressure (HPHT) stirred autoclave reactor and flow-through reactor with pressure up to 24,000 psig and temperatures up to 250 °C, for corrosion and scale testing.

The HPHT autoclave was customized by incorporating electrochemical probes to facilitate in situ monitoring of corrosion rate at HPHT environment. The flow-through reactor was built for corrosion and scale testing at extreme temperatures up to 250 °C and pressure up to 24,000 psig. Coupons with different shapes and of various steel materials including carbon steel, nickel alloys, and corrosion resistant alloys were tested. Additionally, coupon corrosion rates at various conditions (different temperature, and brine composition as well as partial pressure of CO_2) were studied. Different coupon surface analysis techniques including vertical scanning interferometry (VSI), scanning electron microscopy (SEM), and X-ray diffraction (XRD) were employed for more thorough mechanistic understanding of corrosion of steel alloys at HPHT conditions.

A flow-through HPHT apparatus to study mineral solubility up to 250 °C and 24,000 psig was built to facilitate the measurements of kinetics of precipitation, dissolution, and solubility. Calcite solubility experiments were conducted at xHPHT conditions to evaluate the ability of the apparatus to test at these extreme conditions. Results obtained for calcite solubility at xHPHT can be found on Section 7.1 of this report.

Significant progress was made towards assessing and understanding corrosion and scale formation at extreme temperature and pressure encountered in ultra deepwater development. The experimental tools and test procedures developed in Phase I allow for better understanding of the corrosion and scaling process under HPHT conditions. The experimental setup and equipment designed and employed in Phase I of the project was proved to be applicable and reliable for HPHT corrosion and scale research. The methods developed for corrosion and scale testing will be extended to inhibition studies proposed for Phase II of the project. The data collected will be combined eventually in a thorough model being developed in Phase II and Phase III of this project as well.

Initially, H_2S gas testing was included in the scope of work. However, at our meeting in January 2013, the Working Project Group recommended that we postpone H_2S testing until we visited another facility to assess their setup in order to assure safety. Following this recommendation, a visit was scheduled to a local laboratory where multiple H_2S autoclave tests are routinely performed to review the facilities and necessary precautions for testing conditions. The facility includes secluded rooms with atmospheric ventilation, operation for the reactors from outside the room, and an emergency ventilation system. We are working closely with this local laboratory and are in discussions to utilize the facility to perform H_2S testing in Phase II of this project. In addition, we have designated one section of our laboratory for H_2S testing should RPSEA and the Working Project Group decide we should perform the testing at Brine Chemistry Solutions' labs. This section is separated from the rest of the lab and has access to the outside through a back door as well as an ideal setup for continuous ventilation. Before H_2S testing begins, we

will ensure that all of the safety precautions and regulations are satisfied. As an additional precaution, all personnel involved in the project have completed H_2S safety training by Falck Alford certified trainers to assure that they are prepared to work with H_2S safely.

This section is organized as three subsections: the first section describes the experimental work done in a static HPHT stirred autoclave reactor for corrosion, the second section contains the corrosion tests conducted in the xHPHT flow-through apparatus and the third section describes the scale solubility work done in the flow-through apparatus.

Subsection 1. Corrosion Tests in Static Stirred Autoclave Reactor

Introduction

An important goal for this project was to generate data, develop models, and produce experimental tools to assess corrosion at extreme pressure and temperature (xHPHT) encountered in deepwater development. The autoclave reactor is used for high temperature and high pressure corrosion studies.[1] However, in situ measuring/monitoring of corrosion rate in the autoclave system is always a limitation. Very limited work has been found on the application of electrochemical measurement in the extremes of pressure and temperature conditions scoped in this project.[2, 3] Therefore, in Phase I of this project, a HPHT autoclave setup was employed and customized to conduct corrosion experiments to assess the risk of corrosion of various of steel materials, with the capability of electrochemical measurement for in situ corrosion rate monitoring. The design of this highly customized but also easy to use autoclave setup was confirmed to be very successful for HPHT corrosion studies. It enables the studies of corrosion behavior of different types of steel coupons at realistic extremes of temperature and pressure, as well as high salinity conditions. Effects of temperature, CO_2 concentration, and brine chemistry on the uniform corrosion rate as well as localized corrosion rate of those different alloys were studied and reliable data was collected. This will be used for building a HPHT corrosion model as proposed for Phase II of this project. All the coupons for corrosion testing were obtained from "Metal Samples", a branch of Alabama Specialty Products, Inc. (ASPI). The size and shape of all the corrosion test specimens were designed in accordance with ASTM standard guide recommended by NACE.[4] Corrosion rate of steel coupon was measured using both weight loss method and electrochemical method linear polarization resistance (LPR). Localized corrosion was characterized by using a vertical scanning interferometry (VSI). A new methodology of using this innovative technique was developed and is discussed in detail in subtask 6.1. Selected coupons were also examined using traditional techniques such as scanning electron microscope (SEM) and x-ray diffraction (XRD) to characterize the corrosion product scales and to obtain more thorough mechanistic understanding of the corrosion process.

The experimental details and results obtained on the effects of temperature, CO_2 concentration, and brine chemistry on corrosion rate of different types of steel were discussed and are present below in detail.

Experimental Details

HPHT Autoclave Reactor Corrosion Test Setup

A highly customized HPHT autoclave reactor (Parr Instruments Inc.) was employed for corrosion testing of coupons of various steel materials (Figure 2). All the wetted parts in this static reactor are made of Hastelloy C-276. A temperature and pressure controller was connected to the reactor to enable in situ controlling, monitoring, and recording of the temperature and pressure inside the reactor. A liquid sampling valve was connected to the reactor for in situ liquid sampling. Also three ports were installed on the head of the reactor to mount in electrochemical probes for corrosion monitoring.

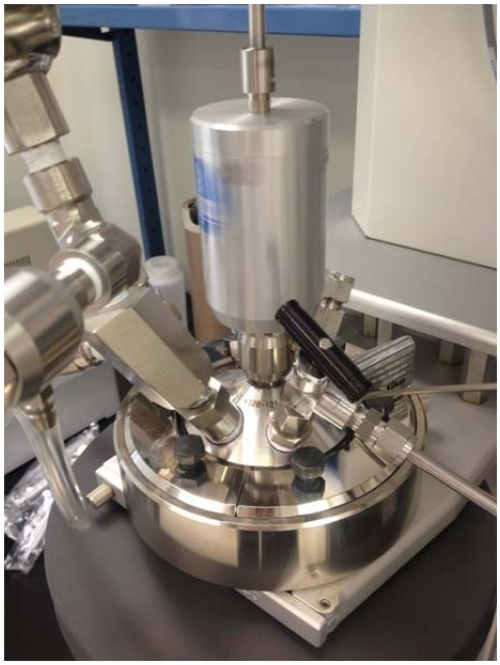

Figure 2. View of the HPHT static autoclave reactor head – custom manifold.

Electrochemical probes (Figure 3) that can operate at temperature up to 250 °C and pressure up to 3,000 psig were designed for corrosion studies. The electrode probe bodies are made of Hastelloy C-276. Steel coupons for electrochemical measurements were spot welded on the Hastelloy C-276 tip on the working electrode (WE) probe. A platinum tip was used as the counter electrode (CE) and a standard saturated Ag/AgCl probe was used as the reference electrode (RE). All the electrochemical measurements of the corrosion process were made with a Gamry™ Reference 600 potentiostat (Figure 4).

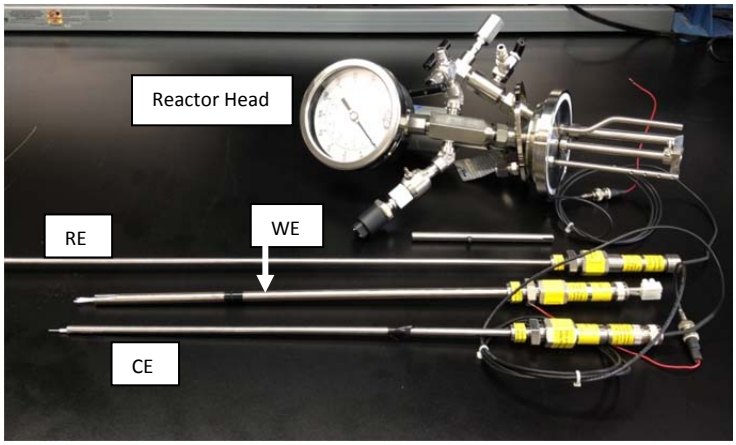

Figure 3. View of the HPHT probes: Reference electrode (RE), working electrode (WE) and counter electrode (CE) for electrochemical measurements and the highly customized autoclave reactor head.

Figure 4. View of potentiostat for electrochemical measurements.

HPHT autoclave reactor corrosion test procedure

All the corrosion experiments were conducted in a 1 L Hastelloy C-276 autoclave reactor. The test solutions were prepared with sodium chloride (ACS grade) and de-ionized (DI) water. For the experiments presented in this report, at the beginning of each test, the test solution was deoxygenated and saturated with CO_2 by continuously sparging CO_2 to the solution at room temperature. The pH of this CO_2 saturated solution was adjusted to 5.0 by using de-oxygenated 1 M $NaHCO_3$ solution as well. Then a previously cleaned (bead blasted 600 grit) new coupon was placed on the holder in the HPHT autoclave reactor and inserted into the solution, and the reactor was sealed and charged with targeted partial pressure of CO_2, which was measured at room temperature. Then the rotator and heater were turned on and experiment starts. All the experiments the rotating speed was set as 100 rpm. In experiments with electrochemical measurements, the corrosion rate was recorded once the target test

temperature was reached. After the test was finished, the hot autoclave was cooled before it was opened. After the coupons were taken out of the reactor, they were rinsed with DI water and isopropyl alcohol (IPA) to clean the surface and to prevent possible further reaction with air. The coupon was then stored in a bag filled with N_2 and stored in a desiccator for further SEM/XRD or VSI analysis.

Corrosion rate monitoring/measurement techniques

Weight loss method.[5]

$$\text{Corrosion rate} = (K \times W)(A \times T \times D)$$

where:

K = a constant, K = 8.76×10^4 if corrosion rate unit desired is millimetres per year (mm/yr) .

T= time of exposure in hours to the nearest 0.01 h.

A= area in cm^2 to the nearest 0.01 cm^2.

W= mass loss in g, to nearest 1 mg (corrected for any loss during cleaning).

D= density of test specimen in g/cm^3.

LPR measurement: [6]

$$i_{corr} = \frac{B}{R_p}$$

$$CR = 1.16 \times i_{corr}, (\text{mm/yr}),$$

where:

B is a constant; B = 26 in this report.

R_p is the polarization resistance measured from LPR.

i_{corr} is the corrosion current density, A/m^2.

Results and Discussion

Effect of Temperature

In preliminary experiments, before electrochemical measurement and vertical scanning interferometry facilities were available, the weight loss method was used to calculate corrosion rate. The effect of temperature was evaluated for this set of experiments. Figure 5 shows the corrosion rate obtained for the C 1018 specimens corroded for four hours at different temperatures. Experiments with longer duration (>24 hours) will be conducted in Phase II. The test conditions were 1 M (5.5 wt%) NaCl solution, saturated with CO_2 and initial solution pH adjusted to be 5.0. The dissolved CO_2 concentration was 0.08 M (50 psig charged at 25 °C) for all the temperatures. It can be seen from the results that the corrosion rate shows a trend of increasing with increasing temperature, with an exceptionally high value at 100 °C. The high corrosion rate of about 20 mm/yr at 200 °C and 250 °C is in contrast with published reports.[3] This difference may be due to the short test time and slightly different conditions etc. Longer test duration tests will be conducted in Phase II to see the corrosion rate change over time at those temperatures.

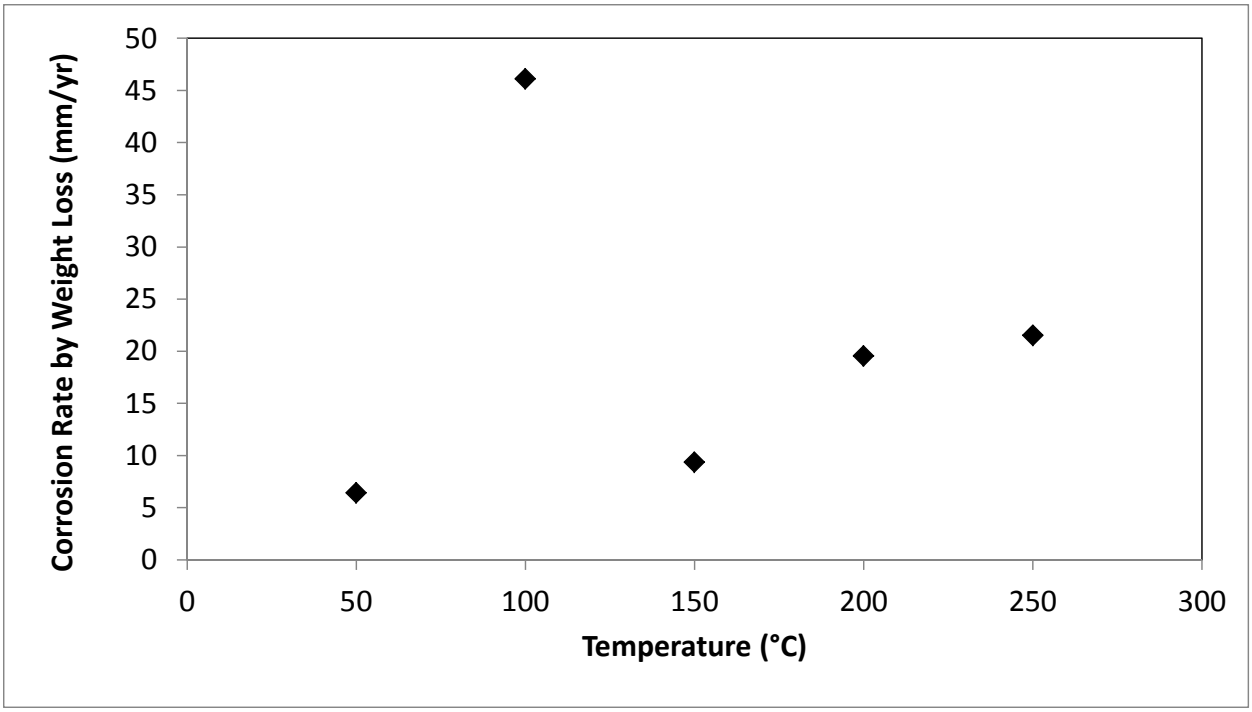

Figure 5. Corrosion rate measured by weight loss method for C 1018 coupons corroded at different temperatures in a 1 M (5.5 wt%) NaCl solution with dissolved CO_2 0.08 M (50 psig CO_2 charged at 25 °C).

Probably, the test duration was too short for the weight loss method to be applied. Weight loss method is a time average as well as surface area average method for corrosion rate calculation. The test duration for the initial tests conducted was too short for a reliable weight loss method analysis. As recommended by NACE, [4] 16 hours test duration is preferred. Another concern is if there is corrosion scale formed on the steel surface, the corrosion kinetics might be changed and this will be studied in Phase II. When the scales are protective, the corrosion process will be slowed down. In addition, if the protective scale is partly broken, localized corrosion might happen. Even though the first series of experiments yielded unexpected quantitative results, the test equipment and test procedures proved to be expected and reliable.

By conducting longer duration tests, more results were obtained. Figure 6 shows the corrosion rate of the C 1018 coupons at temperature 100 °C, and 250 °C for 24 hours in a 1.0 M (5.5 wt%) NaCl solution with 0.057 M dissolved CO_2 (30 psig charged at 25 °C). The solution pH was initially set to be 5.0 by de-oxidized 1 M $NaHCO_3$ at room temperature. The corrosion rate was calculated with the weight loss method. It can be seen that the corrosion rate at 100 °C was higher than the one at 250 °C. The SEM and XRD images of the coupons after corrosion are shown in Figure 7. The morphologies of the steel surface after corrosion were very different at 100 °C and 250 °C. Clearly, hexagonal crystals could be found on the coupon corroded at 100 °C, while for the one corroded at 250 °C, the morphology of the corrosion scales cannot be defined. The XRD analysis shows the hexagonal crystals at 100 °C were $FeCO_3$ and the solid at 250 °C was magnetite.

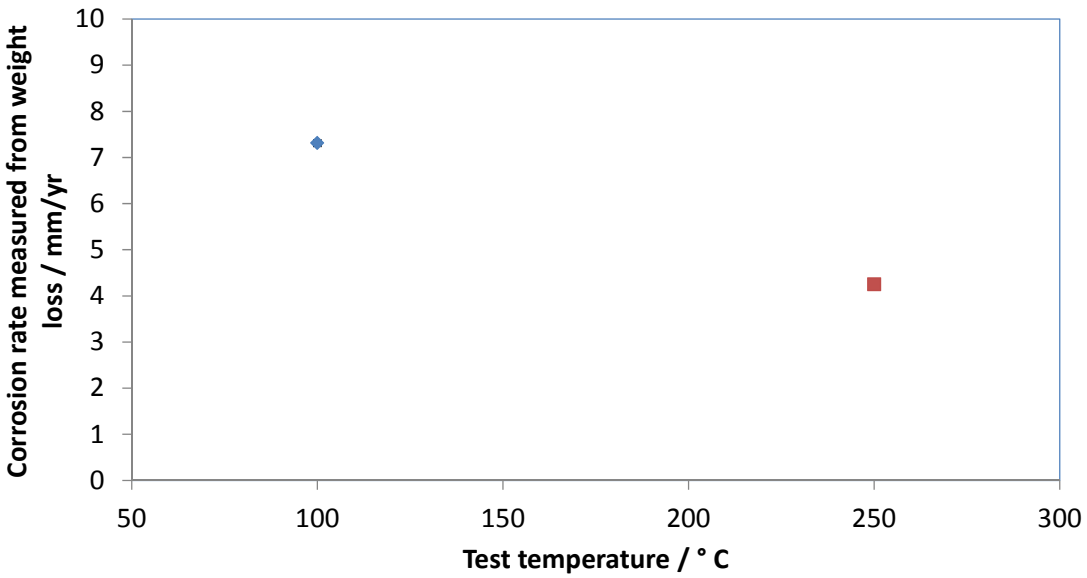

Figure 6. Corrosion rate of C 1018 measured from weight loss method at different temperatures Test conditions are: 1 M (5.5 wt%) NaCl solution with 0.057 M dissolved CO_2 (30 psig CO_2 charged at 25 °C).

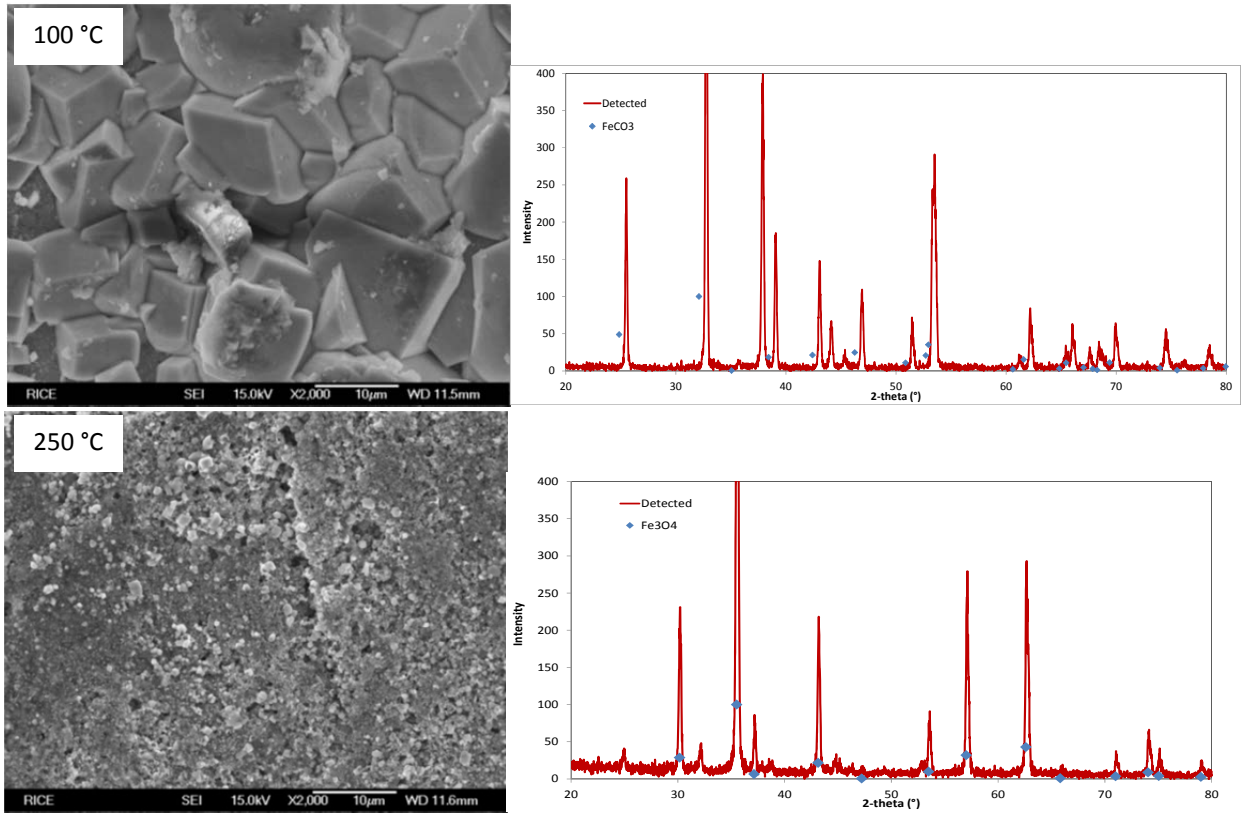

Figure 7. SEM images and XRD results of the C 1018 coupon corroded at 100 °C and 250 °C.

As mentioned above, the weight loss method only gives the average corrosion rate through the entire test period. However, it is very likely that the formation of corrosion product may change the corrosion kinetics so the corrosion rate is not constant over time. It has been known that corrosion products such as iron carbonate and magnetite can be protective. Therefore, electrochemical techniques were employed to enable continuous corrosion rate monitoring (Figure 8).

Figure 8 shows the variation of corrosion rate of C 1018 coupons with time measured by LPR for tests done at 100 °C and 250 °C. The test conditions were 3 M (15.73 wt%) NaCl solution with 0.057 M dissolved CO_2 (30 psig CO_2 charged at 25 °C). Initial solution pH was 5.0 and test duration was 18 hours.

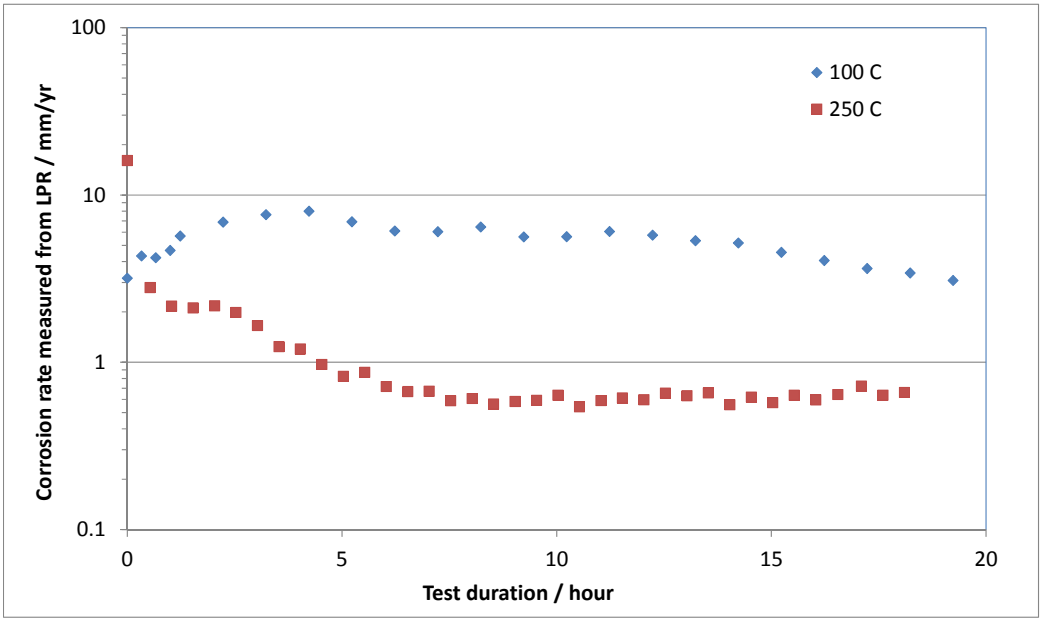

Figure 8. Variation of corrosion rate of C 1018 with time at different temperatures at test conditions: 3 M (15.73 wt%) NaCl solution with 0.057 M dissolved CO_2 (30 psig CO_2 charged at 25 °C).

The data in blue diamonds are for the test at 100 °C, while the ones in red square are for the test at 250 °C. It can be seen that at 100 °C, the corrosion rate of the C 1018 coupon increased from 2 mm/yr to 8 mm/yr in the first five hours, then decreased gradually back to 2 mm/yr. However, at 250 °C, the corrosion rate started with 11 mm/yr and dropped quickly to 1 mm/yr in five hours and kept decreasing until stabilized at about 0.7 mm/yr after approximately eight hours. This low corrosion rate at 250 °C was due to the formation of protective corrosion product scales, which was confirmed to be iron magnetite (Fe_3O_4) from SEM and XRD analysis, as shown in Figure 9 and Figure 10, respectively. Although the peaks in Figure 7 and Figure 9 appear to be offset to a higher 2-theta by a constant amount, the peaks are sharp with little broadening, suggesting well-formed crystals. The offset may be due to systematic substitution of Na^+ for Fe^{2+}, solid solution of e.g. FeO etc., or more likely a systematic error in the recording. The source of the offset will be investigated in Phase II. However, at 100 °C, even though there were some corrosion product scales, which was confirmed to be iron carbonate by SEM and XRD, some part of the surface was not covered. Therefore, the steel was not fully protected and corrosion rate was still high as can be seen in LPR data.

The sample was also cleaned by a method recommended by NACE standard [7] to remove all the corrosion product scales on the surface, and then examined under VSI [subtask 6.1] to see if there was any localized corrosion. Figure 11 shows an example of the VSI images obtained from scanning the coupon. In this report, the consideration of localized corrosion is based on the pitting factor defined by NACE [8, 9], and is defined as if the ratio of the depth of the deepest pit resulting from corrosion divided by the average penetration as calculated from weight loss or LPR is larger than five. It is considered as a pit or localized corrosion. The whole coupon surface was scanned by VSI, and no pits were found per this definition. As an example shown in Figure 11, the coupon corroded at 100 °C, had a very smooth surface after cleaning. The maximum depth found on the surface was 7.14 µm, which is equal to a corrosion rate of 3.5 mm/yr for an 18-hour test. As compared to the surface average corrosion rate measured by LPR (Figure 8), which is 2.0 mm/yr, it is not considered as localized corrosion. The corroded coupon at 250 °C showed similar results, an area of 10 µm depth was found on the cleaned coupon surface, as shown and indicated by a red dashed circle in Figure 12. This 10 µm depth is equal to a corrosion rate of 4.9 mm/yr for an 18-hour test. As compared to the LPR corrosion rate 0.8 mm/yr, it is about six times larger. Therefore, it is considered localized corrosion. However, this localized corrosion was not found everywhere on the steel surface, but only at this single location shown here. This coupon was tested at 250 °C, and it was confirmed that very protective Fe_3O_4 scales were formed on the coupon surface. Therefore, it is suspected that the occurrence of this pitting was due to a breakdown of the protective scales at this particular location. However, more tests are needed to make a conclusion about the localized corrosion mechanisms at this condition. The use of VSI facilitated the findings of the localized corrosion as discussed here. The scanning of this whole coupon surface (3.85 cm^2) took only an hour and the whole process is not destructive to the coupon. VSI has advantages over traditional surface analyses such as traditional interferometry which needs to be operated manually for continuous surface or other techniques such as atomic force microscopy (AFM), which is destructive to the coupon surface, VSI seems to be a powerful tool for the study and analysis of localized corrosion as encountered in xHPHT conditions [subtask 6.1].

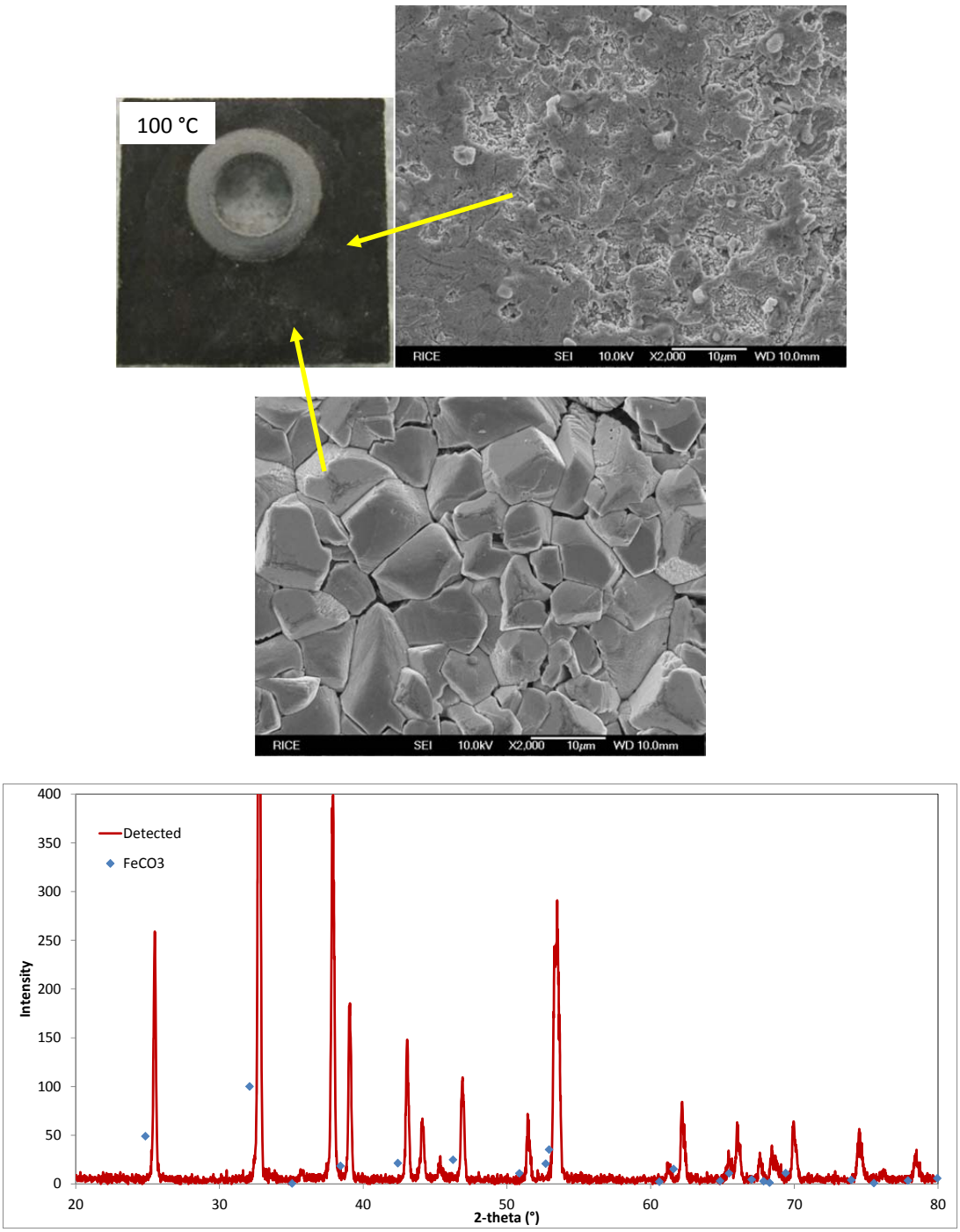

Figure 9. SEM images and XRD results of the C 1018 coupon corroded at 100 °C in a 3 M (15.73 wt%) NaCl solution with 0.057 M dissolved CO_2 (30 psig CO_2 charged at 25 °C).

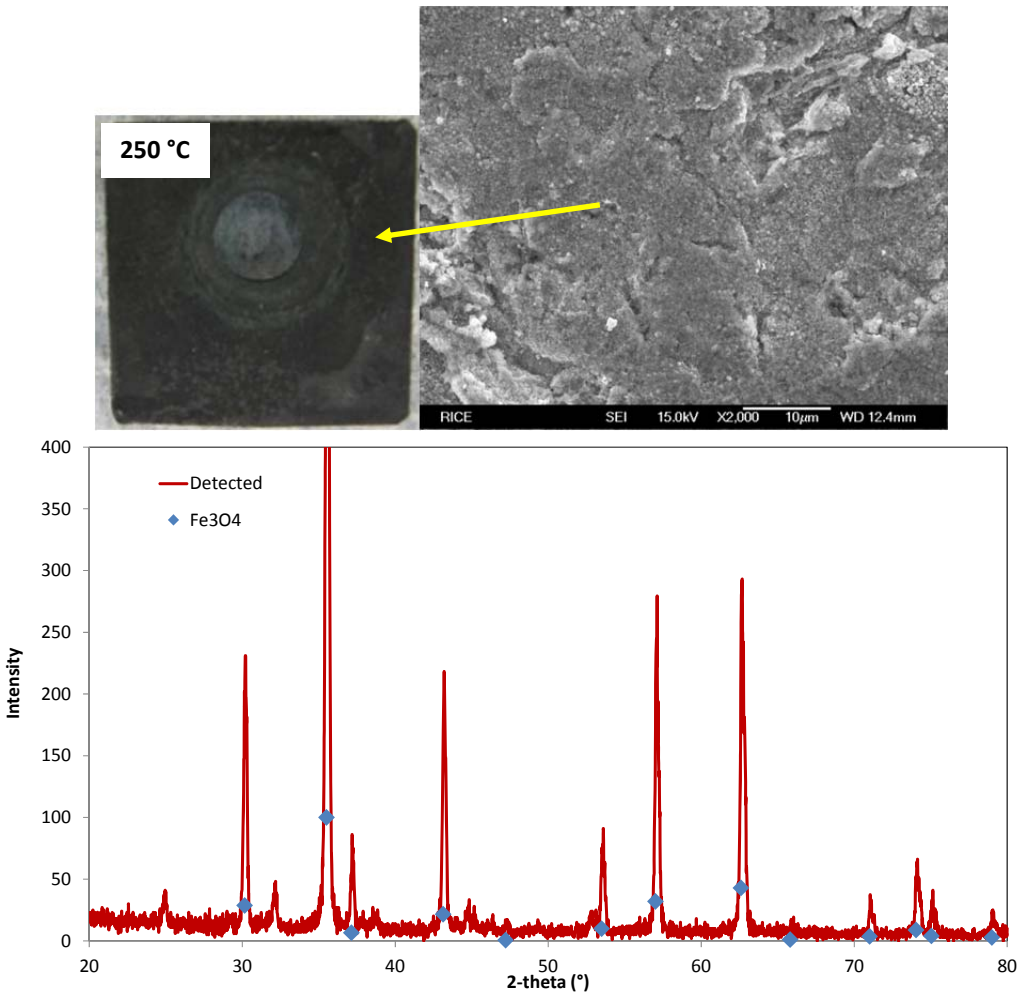

Figure 10. SEM images and XRD results of the C 1018 coupon corroded at 250 °C in a 3 M (15.73 wt%) NaCl solution with 0.057 M dissolved CO_2 (30 psig CO_2 charged at 25 °C).

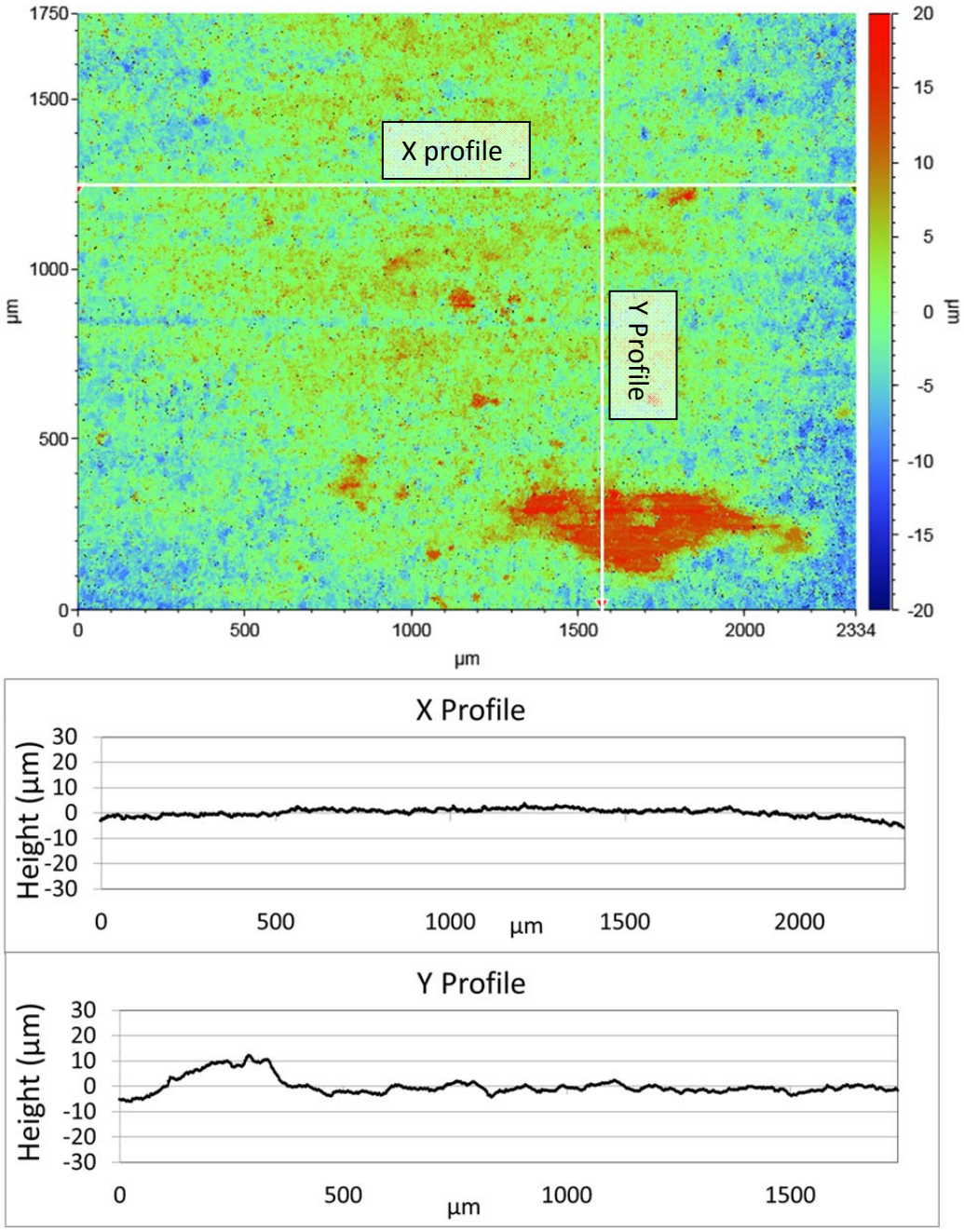

Figure 11. An example of VSI images showing the C 1018 steel surface after it was cleaned. Test conditions were: 100 °C, 0.057 M dissolved CO_2 (30 psig CO_2 charged at 25 °C), 3 M (15.73 wt%) NaCl solution initial pH 5.0.

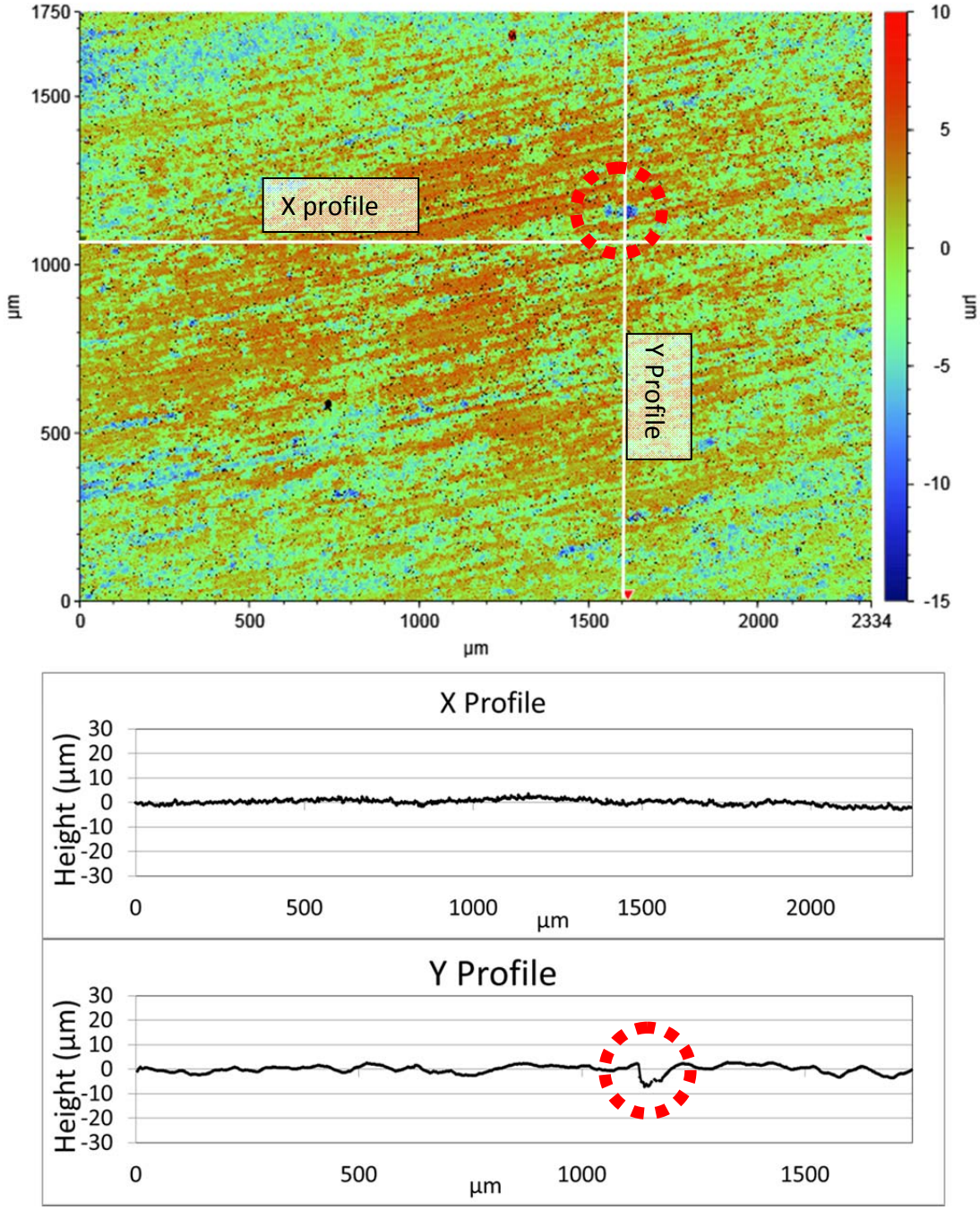

Figure 12. An example of VSI images showing some pits on the C 1018 steel surface after it was cleaned. Test conditions were: 250 °C, 0.057 M dissolved CO_2 (30 psig CO_2 charged at 25 °C), 3 M (15.73 wt%) NaCl solution initial pH 5.0.

Effect of CO_2 Concentration

Tests were conducted at different CO_2 concentrations at 250 °C. The concentration of dissolved CO_2 was controlled by adjusting the CO_2 partial pressure (for 0.05 M dissolved CO_2, 30 psig CO_2 was charged at 25 °C; for 0.1 M dissolved CO_2, 60 psig CO_2 was charged at 25 °C). As can be seen from Figure 13, in both cases, the stabilized corrosion rate was low and the more the dissolved CO_2, the lower the corrosion rate. The SEM images of the C 1018 coupons at these two different CO_2 concentrations are shown in Figure 14. The two coupons' surfaces showed similar morphology.

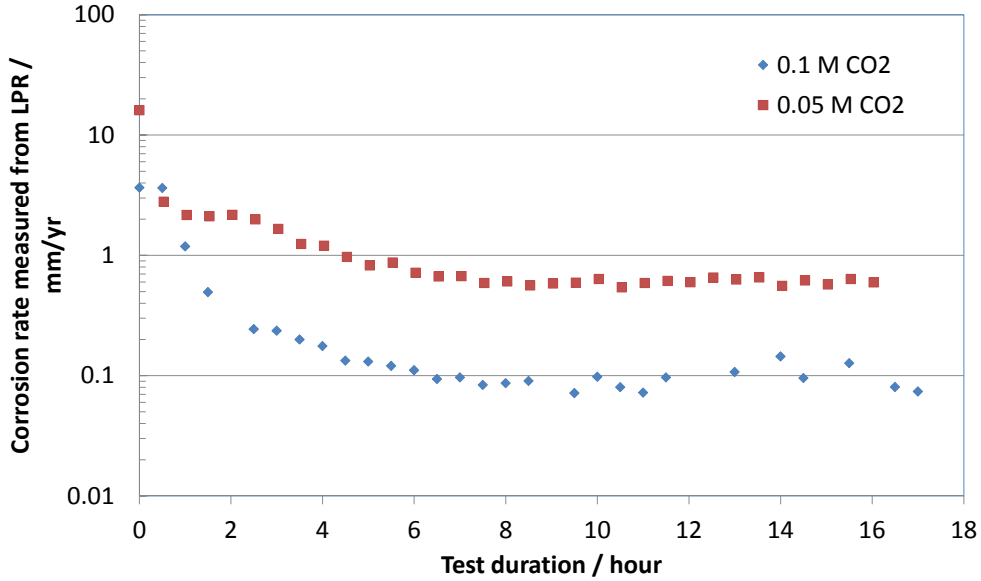

Figure 13. Variation of corrosion rate of carbon steel C 1018 with time at different dissolved CO_2 concentration in a 3 M (15.73 wt%) NaCl solution at 250 °C.

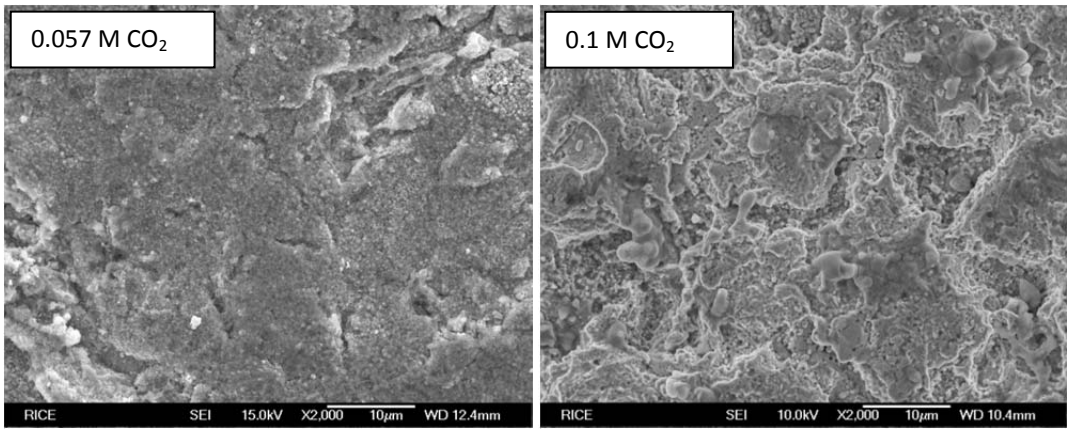

Figure 14. SEM images of the two C 1018 steel coupons tested at different dissolved CO_2 concentration in a 3 M (15.73 wt%) NaCl solution at 250 °C.

The coupons were also examined by VSI after the corrosion product scales were removed. An example of the VSI scanning view of the steel surface is shown in Figure 15. The deepest depth found on the

coupon surface was 9.52 µm, which corresponds to a 5.2 mm/yr corrosion rate for the 16-hour test, as compared to the LPR 0.8 mm/yr; it is six times larger so it is considered as a localized pitting corrosion.

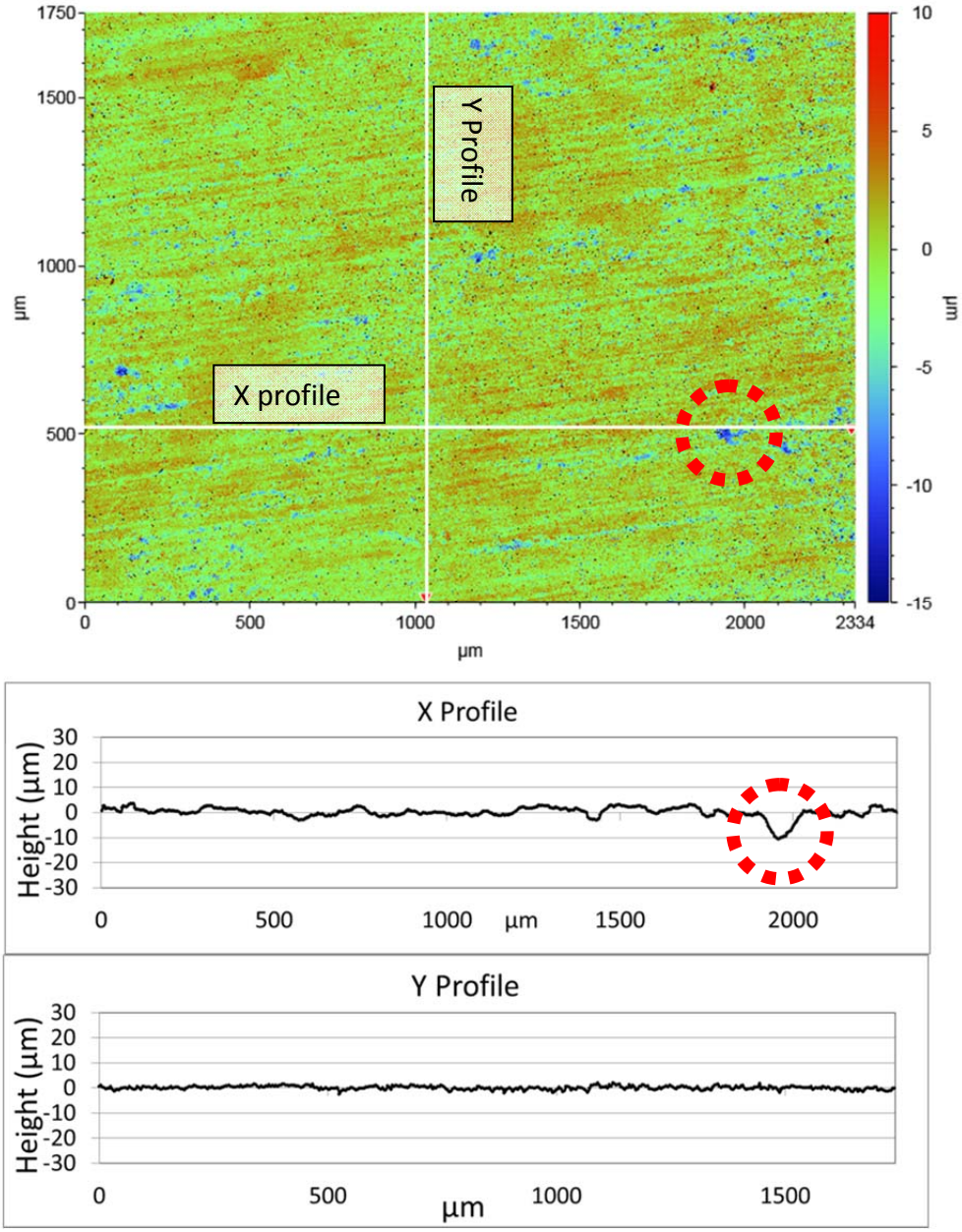

Figure 15. An example of VSI images showing a large pit on the C 1018 steel surface after it was cleaned. Test conditions were: 250 °C, 0.1 M CO_2, 3 M (15.73 wt%) NaCl solution initial pH 5.0.

Different Brine Compositions

Experiments were also conducted in solutions with different salt concentrations. Figure 16 shows the comparison of corrosion rate of C 1018 steel at 250 °C and dissolved CO_2 concentration of 0.057 M (30 psig charged at 25 °C)in 3 M (15.73 wt%) and 6 M (29.85 wt%) NaCl concentrations.

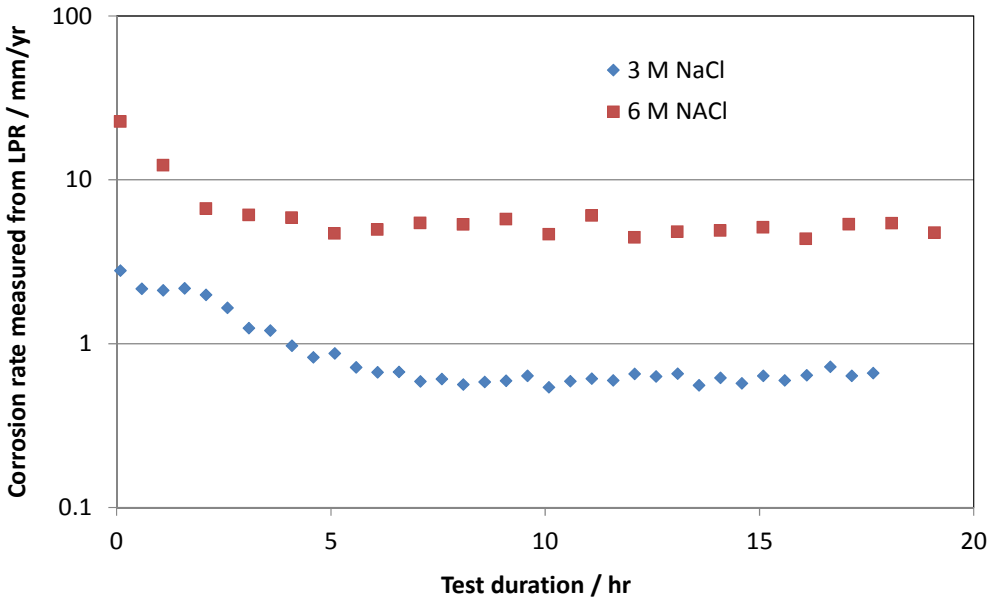

Figure 16. Variation of corrosion rate of carbon steel C 1018 with time in salt solution at different concentration under the same temperature 250 °C and dissolved CO_2 0.057 M(30 psig charged at 25 °C).

It can be seen in Figure 16 that in a 6 M (29.85 wt%) NaCl solution, the corrosion rate of C 1018 was 4.0 mm/yr while in the 3 M (15.73 wt%) NaCl solution, it was much lower, only about 0.7 mm/yr. The coupons surface was examined by SEM as shown in Figure 17. The scales formed on the corroded coupon at 6 M (29.85 wt%) NaCl are more porous than the ones found in the 3 M (15.73 wt%) NaCl test. Fe_3O_4 scales formed on both coupons' surfaces, as confirmed by XRD. These coupons were then checked for localized corrosion by VSI after the corrosion product scales were removed; however, no localized corrosion was found. An example of the VSI scanning of the steel surface corroded in the 6 M (29.85 wt%) NaCl solution is shown in Figure 18. The depth profile shows that the steel surface was smooth, with a variation of less than 5 µm, which corresponds to a corrosion rate of 1.8 mm/yr for this 16-hour test. Compared to the corrosion rate of 4.0 mm/yr measured by LPR, this is not considered as localized corrosion.

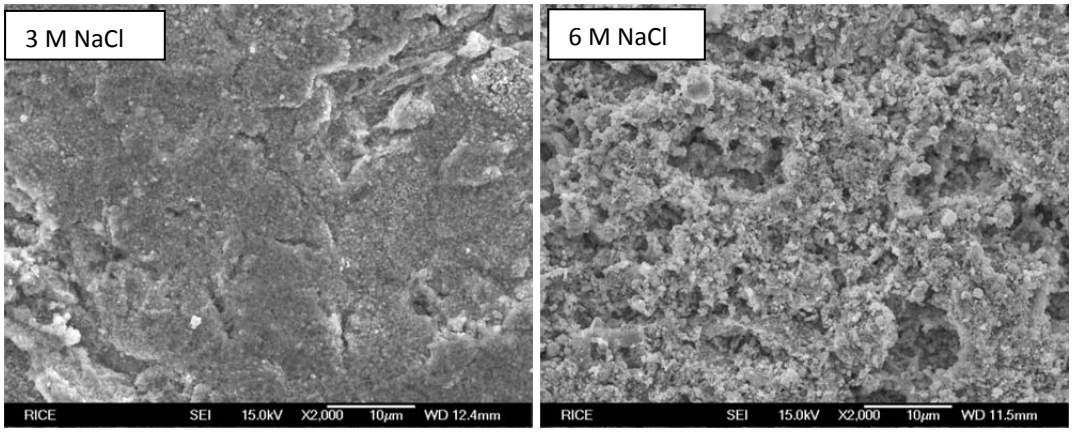

Figure 17. SEM images of the C 1018 steel coupons tested at different salt concentrations under the same temperature (250 °C) and dissolved CO_2 0.057 M (30 psig CO_2 charged at 25 °C).

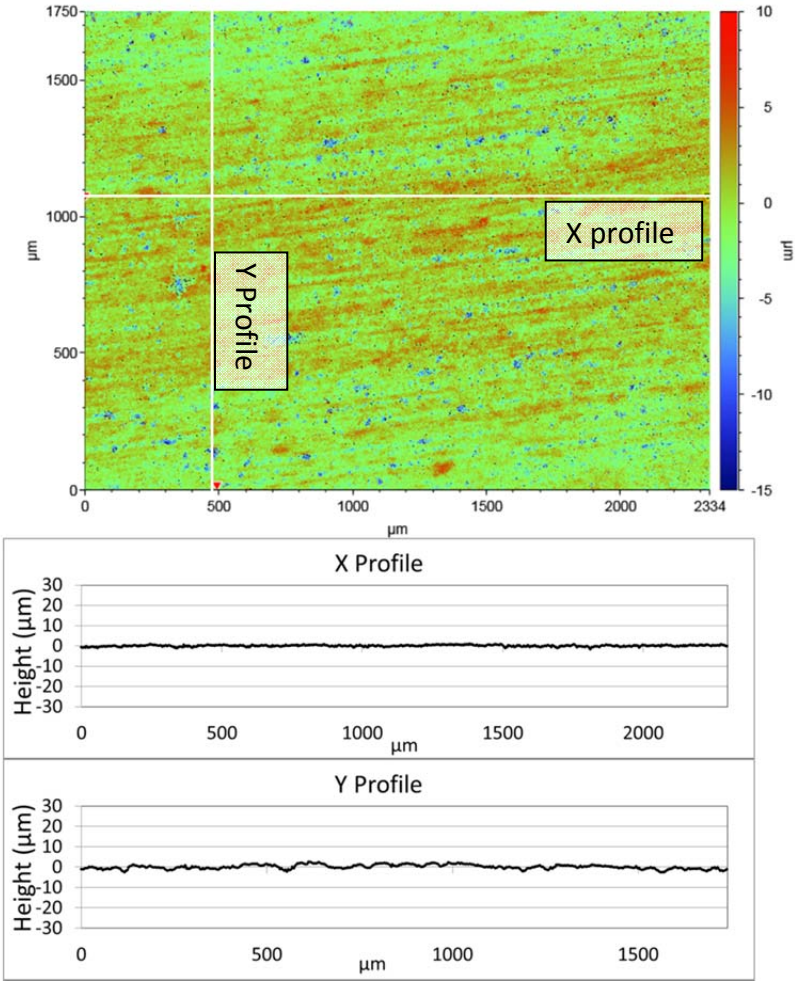

Figure 18. An example of VSI images showing the smooth C 1018 steel surface after it was cleaned. Test conditions were: 250 °C, 0.057 M (30 psig CO_2 charged at 25 °C) dissolved CO_2, 6 M (29.85 wt%) NaCl solution.

Different Alloys

One of the goals proposed in Phase I was to evaluate different steel materials that might be used for UDW oil and gas production. As recommended and suggested by the Working Project Group (WPG), seven different steel materials were selected for testing at this stage, including carbon steel, stainless steel, and corrosion resistant alloys. The composition of each material is listed in Table 1.

Table 1. Composition of different alloys tested in the present work.

Element	I 825	I 718	G3	C1018	316 L	420 (13-Cr)	410 (13-Cr)
Al	0.1	0.57		0.03			0.002
B		0.001					
C	0.02	0.03	0.003	0.19	0.021	0.36	0.14
Ca				0.001			
Co		0.14	1.69				
Cr	22.2	18.54	22.27	0.03	16.72	13.6	12.17
Cu	2	0.2	1.87	0.08			0.15
Fe	31	17.57	19.07	98.853	68.809	84.872	86.522
Mn	0.5	0.15	0.8	0.67	1.89	0.51	0.36
Mo	3.3	2.97	6.96	0.02	2.03	0.05	0.03
N				0.007	0.05		0.01
Nb/Nb+Ta		5.29	0.31	0.004			
Ni	39.2	53.38	64.441	0.04	10.06	0.2	0.19
P		0.008	0.007	0.03	0.03	0.018	0.025
S	0.0004	0.0008	0.002	0.01	0.0004	0.03	0.001
Si	0.3	0.11	0.5	0.02	0.39	0.36	0.39
Sn				0.008			0.01
Ta							
Ti	0.8	1.01		0.004			
V				0.003			
W			1.15				

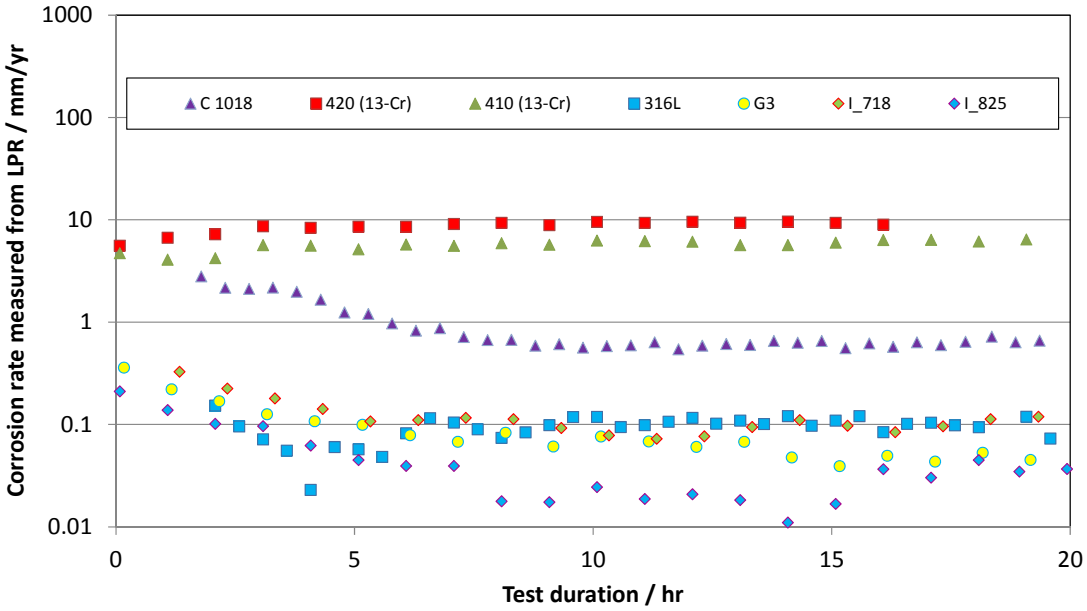

Figure 19. Variation of corrosion rate of different alloys with time in a 3 M (15.73 wt%) NaCl solution with 0.057 M dissolved CO_2 (30 psig CO_2 charged at 25 °C) at temperature 250 °C.

Figure 19 is a comparison of the corrosion rate for different alloys at 250 °C in a 3 M (15.73 wt%) NaCl solution with 0.057 M dissolved CO_2 (30 psig charged at 25 C). Both 13-Cr alloy 410 and 420 had corrosion rates around 10.0 mm/yr; carbon steel C 1018 had a corrosion rate around 2.0 mm/yr at the beginning of the test and then stabilized at about 0.8 mm/yr. Nickel alloys I-718 and I-825, and stainless steel 316 L all showed good corrosion resistance of less than 0.1 mm/yr corrosion rate. Figure 20 shows the view of an I-825 coupon before and after a 20-hour test. Very little change of the coupon was observed. These results can only be considered as preliminary to demonstrate the feasibility of testing at xHPHT conditions. Many additional tests must be conducted at varying times, stir rates, and solution conditions, as planned for Phase II.

Selected coupons were scanned under SEM and are shown in Figure 21. Differences in the surface morphologies can be clearly seen. Some scales could be found on the C 1018 coupon surface, while the surface of the 13-Cr 420 coupon looked very smooth and many crack marks could be seen. Figure 22 shows an example of VSI view of the cleaned stainless steel 316 L coupon surface. The surface was very smooth, no localized corrosion was found on the 13-Cr (410) coupon surface either (Figure 23), and the maximum depth found on the coupon surface was 13.75 µm, which is equal to a corrosion rate of 6.0 mm/yr. As compared to the LPR corrosion rate of 8.0 mm/yr, it is not localized corrosion.

Potentially the most severe problem facing corrosion resistant alloys (CRAs) is localized corrosion in the form of pitting. It is considered that the test conditions shown here were probably not severe enough to form pits. Therefore, the next step in corrosion tests on CRAs will be with a higher total dissolved salt (TDS) and chloride brine solution, as well as different gas types such as H_2S and longer test durations.

Figure 20. View of an I-825 test coupon before (left) and after (right) 24 hours corrosion at 250 °C in a 3 M (15.73 wt%) NaCl solution with 0.057 M dissolved CO_2 (30 psig charged at 25 °C).

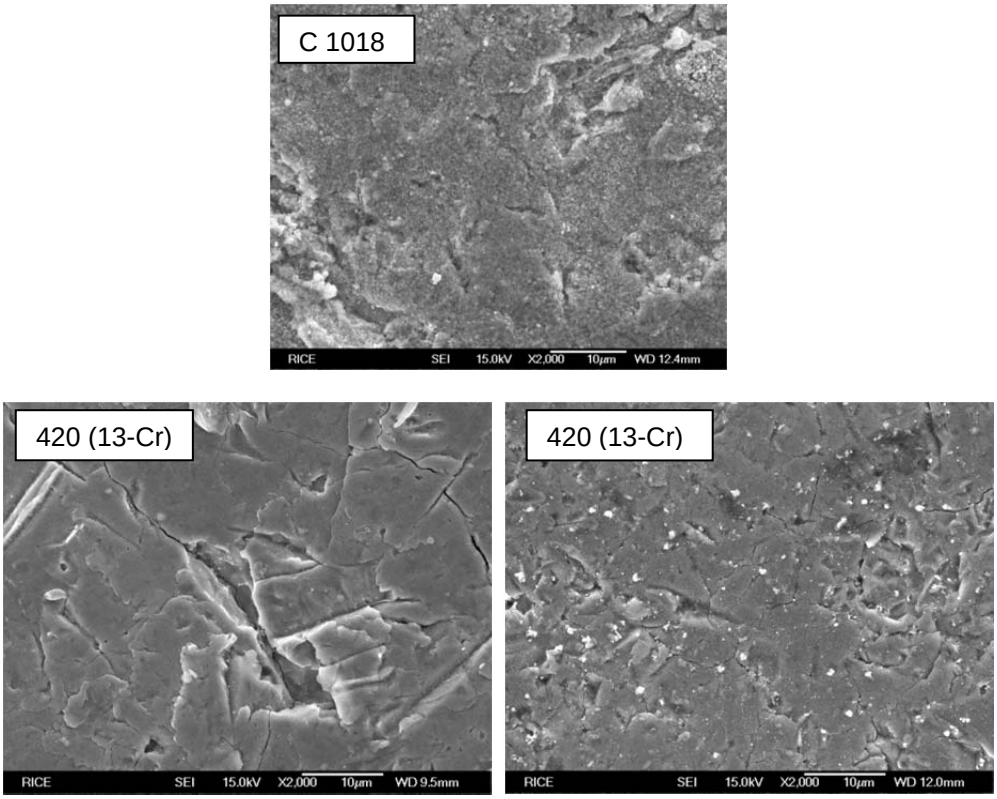

Figure 21. SEM images of different alloy coupons tested at 250 C in a 3 M (15.73 wt%) NaCl solution with 0.057 M dissolved CO_2 (30 psig charged at 25 °C).

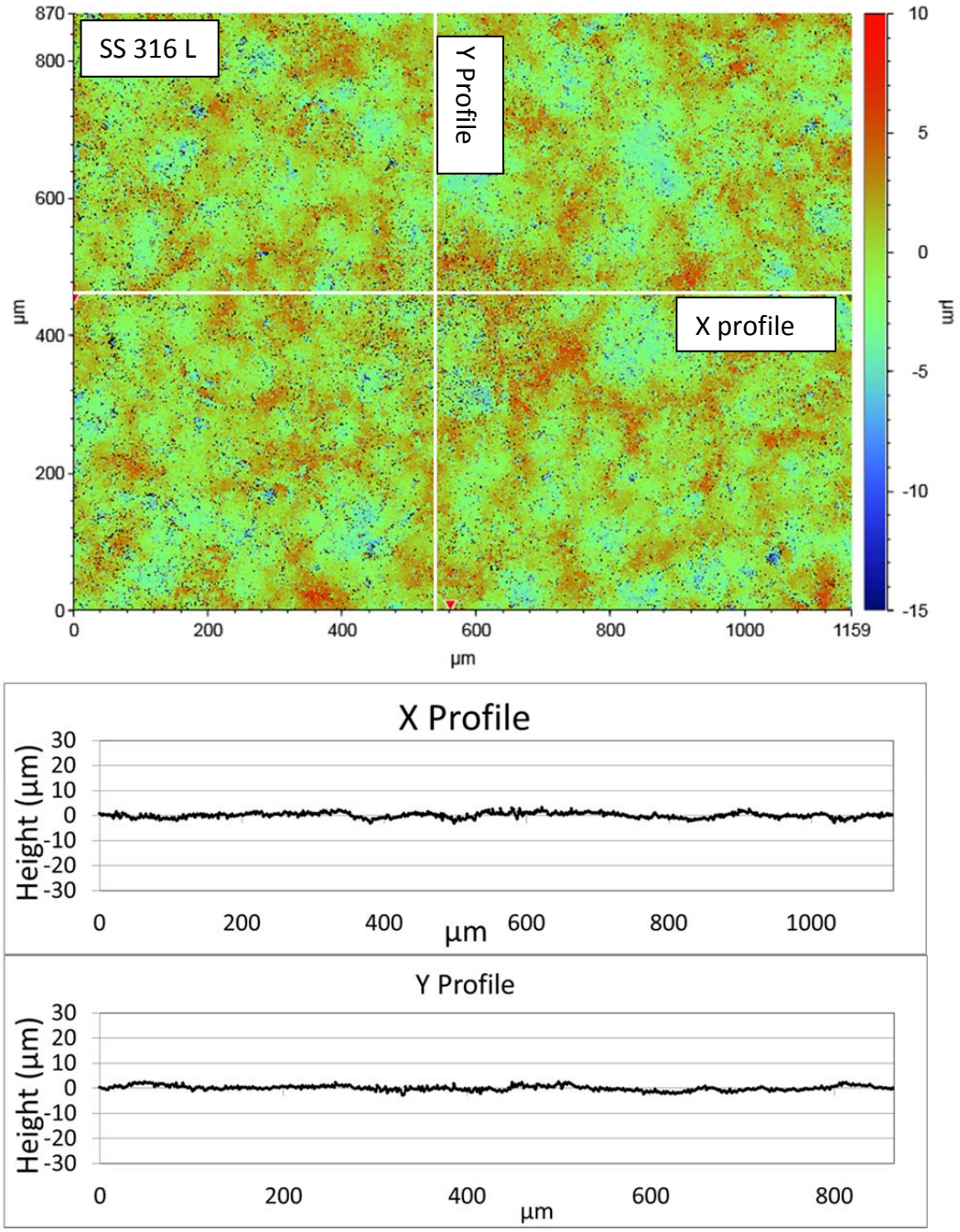

Figure 22. An example of VSI images showing the smooth 316 L stainless steel surface after it was cleaned. Test conditions were: 250 °C, 0.057 M dissolved CO_2 (30 psig charged at 25 °C), 3 M (15.73 wt%) NaCl solution.

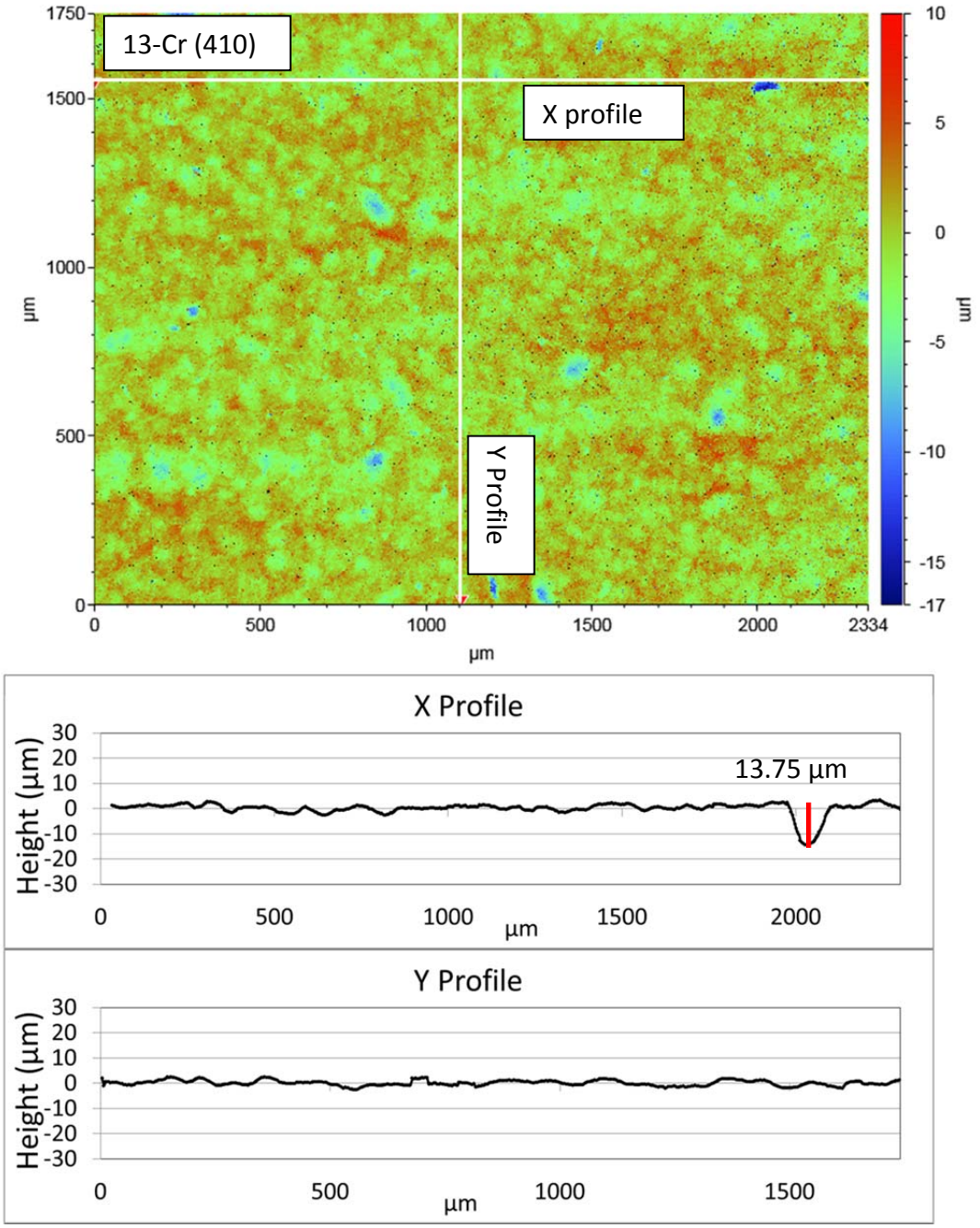

Figure 23. An example of VSI images showing the smooth 410 (13-Cr) surface after it was cleaned. Test conditions were: 250 °C, 0.057 M dissolved CO_2 (30 psig charged at 25 °C), 3 M (15.73 wt%) NaCl solution.

Conclusions

Corrosion screening tests were conducted as a function of temperature, partial pressure of CO_2 and solution composition on carbon steel C 1018, SS 316 L, and nickel alloys I-718, I-825, and G3, as well as on 13-Cr 420 and 410. All screening tests were performed in a HPHT Hastelloy C-276 autoclave reactor using both weight loss method and electrochemical technique linear polarization resistance method. Selected steel coupons were also examined by VSI, SEM, and XRD to understand the corrosion process mechanisms. The customized corrosion testing equipment autoclave reactor has been shown to be reliable for the current research. The method of using electrochemical probes for corrosion monitoring has proved to be an advantageous complement to the traditional weight loss method and applicable for the extremes of pressure and temperature conditions studied in this project.

At test conditions presented in this report, i.e., concentration up to 6 M (29.85 wt%) NaCl brine solution, up to 250 °C, 0.097 M dissolved CO_2 concentration (60 psig CO_2 charged at 25 °C), and test duration of up to 24 hours, it was found that for carbon steel C 1018 the uniform corrosion rate was lower at higher temperature (250 °C) than at 100 °C. At 250 °C, Fe_3O_4 was formed on the C 1018 coupons, while at 100 °C $FeCO_3$ scales were found. The uniform corrosion rate at 100 °C was high, which indicates that the formed $FeCO_3$ was not protective and some pits were found on the coupon surface. Some localized corrosion (pit penetrating rate is five times larger than weight loss and LPR measured surface average corrosion rate) was found on the coupon corroded at 250 °C, where protective Fe_3O_4 was formed. VSI was demonstrated to be a powerful tool for localized corrosion analysis. CRAs and nickel alloy materials did not suffer general corrosion problems nor localized corrosion. One reason might be the short exposure time, longer test duration, as well as more complicated brine chemistry (with Fe^{2+}, Ca^{2+}, Mg^{2+} etc.) or gas (e.g., H_2S) composition are necessary and will be performed to see if and how corrosion (both general and localized) problems occur.

The experimental data collected in Phase I of the project are generally consistent with expected trends in corrosion rate versus temperature and composition, and will be incorporated into a model, which will be developed in Phases II and III of this project. Also, the most important goals fulfilled in Phase I are the confirmation that the test equipment designed and test method and techniques developed for corrosion testing can be used and extended easily to corrosion inhibitor studies for Phase II of this project.

Subsection 2. Corrosion Tests in Flow-Through Apparatus

Introduction

Changing the basic apparatus design used in the Brine Chemistry Consortium research group at Rice University for studying mineral solubility, a flow-through reactor as shown in Figure 24 was built by BCS to study corrosion under xHPHT and high salinity conditions. All the parts having contact with synthetic brine solution, including tubing, fittings and valves, were from Hastelloy C-276 due to its high resistance to corrosion. Hastelloy C-276 tubing with a 0.250 in O.D., 0.083 in I.D., and a total length of 80 in was used to build the system. A high pressure pump with maximum pressure of 24,000 psig was used to pump synthetic brine. All the tubing is purchased from High Pressure Equipment Company and rated to a pressure of 30,000 psig to ensure safety. A gas chromatography (GC) oven was used to

provide programmable control of temperatures up to 250 °C. An air actuated regulator was used to adjust flow rate and keep constant pressure throughout the system.

Tubing for corrosion evaluation was made from various metals, with a 0.250 in O.D., 0.083 in I.D., and length of 4 in, which corresponds to a bed volume of 0.022 in^3 (0.36 mL). The complete volume of the system including the tubing, fittings, and the test tubing was approximately 8 mL, which allows the solution to equilibrate at temperature and pressure before entering the tubing.

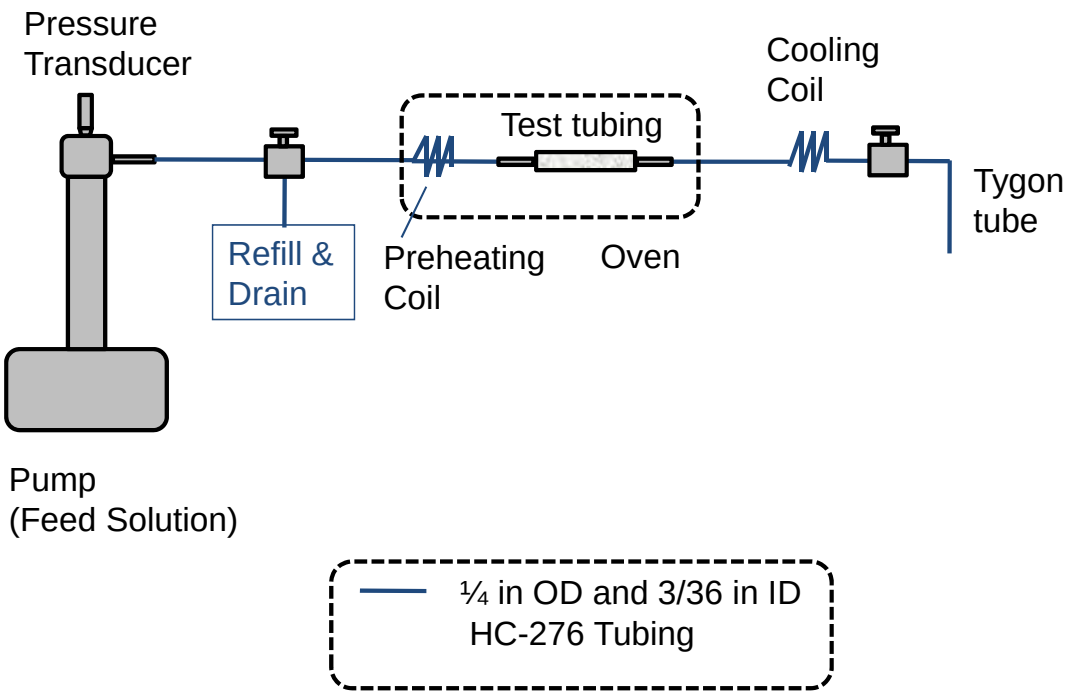

Figure 24. Schematic and picture of the experimental setup for flow-through corrosion study under xHPHT.

Experimental Details

Two types of synthetic brines were used to simulate two UDW well conditions. As shown in Table 2, Brine #1 contains 3 M (15.73 wt%) NaCl, 3 mM $NaHCO_3$ and Brine #2 contains 4.1 M (19.33 wt%) NaCl, 0.15 M $CaCl_2 \cdot 2H_2O$, 3 mM Na_2SO_4, and 3 mM $NaHCO_3$. The Brine #2 composition was suggested by the working project group as representative brine for GOM ultra-deepwater (UDW) reservoirs.

The prepared brines had a pH of 6.05; both brines were pre-saturated with 97 percent CO_2 gas for approximately 20 minutes at ambient temperature. The pH of both brines after CO_2 saturation was approximately 3.5 pH, and 3 mM $NaHCO_3$ was used to adjust the pH to 5.

Tubing made of SS 316 L, Hastelloy C-276, and C 1010 with length of 4 in (bed volume was about 0.8 ml) were used as test tubing coupons for xHPHT corrosion experiments (Table 3). All experiments were performed at 250 °C (482 °F) and 24,000 psig under a flow rate of 0.03 mL/min. Experimental conditions are listed in Table 3.

Table 2. Brine Compositions #1 and #2 for flow-through corrosion experiments.

Brine #1	**Brine #2**
3 M (15.73 wt%) NaCl 3 mM $NaHCO_3$ saturated with 97% CO_2 pH = 5	4.1 M (19.33 wt%) NaCl 0.15 M $CaCl_2 \cdot 2H_2O$ 3 mM Na_2SO_4 3 mM $NaHCO_3$ saturated with 97% CO_2 pH = 5

Table 3. Summary of experimental conditions for flow-through tests.

Exp #	Metal	T (°C)	P (psig)	Q (mL/min)	Brine	OD (in)	ID (in)	L (in)	Bed Volume (ml)
1	HC-276	250	24,000	0.03	#1	0.25	0.0835	4	0.36
2	1010	250	24,000	0.03	#1	0.25	0.125	4	0.8
3	316 LSS	250	24,000	0.03	#1	0.25	0.0835	4	0.36
4	316 LSS	250	24,000	0.03	#2	0.25	0.0835	4	0.36

Methodology

A four-inch section of tubing was connected to the fittings and placed inside the GC oven. The system was washed first with deionized (DI) water at 20 ml/min for two minutes and then washed with synthetic brine for another two minutes under the same flow rate to assure water was purged out of the system and that air bubbles were eliminated. The pressure was then increased from 15 psia (and room pressure) to 24,000 psig at room temperature, followed by an increase in temperature from 25 °C to 250 °C. At 250 °C and 24,000 psig the flow rate was controlled at 0.03 ml/min by manipulating the backpressure regulator. The dead volume (approximately 3.6 ml) was collected for analysis as well, which is from the entering point of brine into the test tubing to the end of the collection tubing. The first three bed volumes were used to pre-flush the test tubing, and samples were collected from the fourth bed volume. The total reaction time was from two to four hours. Samples were diluted with 1 percent HNO_3 approximately 10 times for inductively coupled plasma (ICP) analysis (Perkin Elmer, Optima 8300) for concentration of various ions including iron (Fe), manganese (Mn), chromium (Cr), nickel (Ni), and molybdenum (Mo). After the reaction time had elapsed temperature was decreased to room temperature followed by the decrease of pressure to room pressure. The rest of the brine left inside of the apparatus was flushed by pumping DI water. The test tubing was separated from the apparatus and, as shown in Figure 25, was cut in half length wise by using a Buchler cut off saw with a diamond watering blade for further characterizations. A SEM was used to analyze the morphology of the tubing surface after the flow-through corrosion test. If solid deposits were observed under SEM, they were scratched off from the tubing surface to be analyzed by XRD analysis to confirm the crystal structure. Test tubing surface was cleaned by following the cleaning method recommended by NACE.[7] VSI was then used to image the depth of pits.

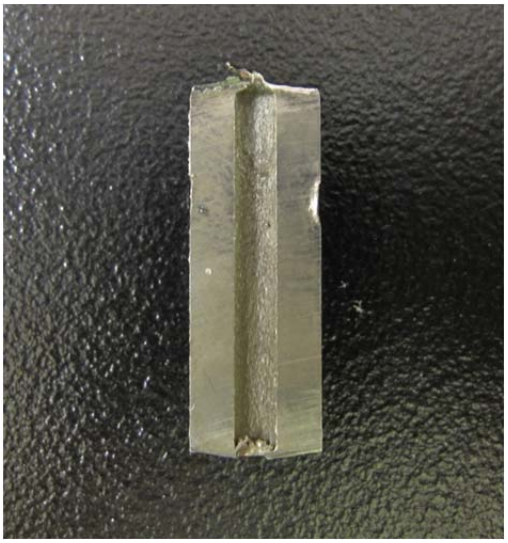

Figure 25. View of a Hastelloy C-276 test tubing after being cut in half length wise.

Results and Discussions

Experiment #1 – Hastelloy C-276

Figure 26 shows the SEM images of the Hastelloy C-276 tubing before corrosion test (left) and after (right). It can be seen that after three hours of continuous flow of Brine #1 that no significant change in the steel surface morphology was seen.

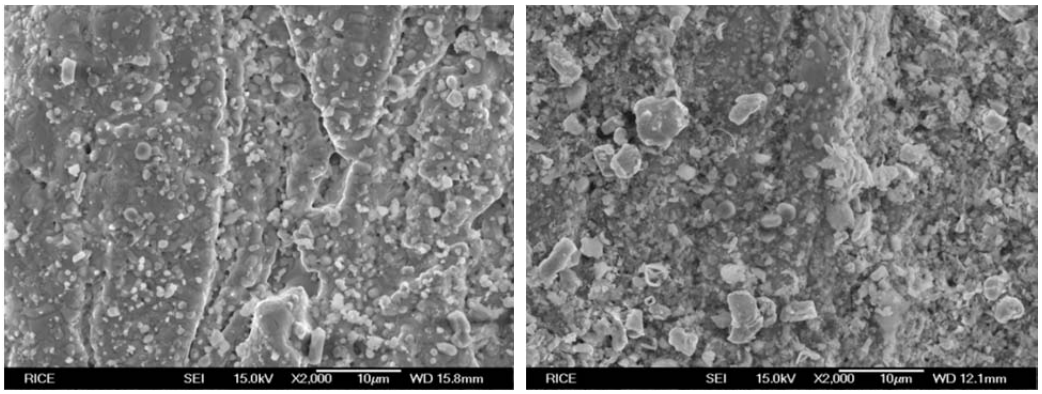

Figure 26. SEM images of the Hastelloy C-276 test tubing inner surface before corrosion test (left) and after (right). Test conditions were 250 °C, 24,000 psig, brine #1 flow-through with flow rate of 0.03 mL/min for three hours.

Figure 27 shows the VSI images of this tubing before (left) and after corrosion test (right). Test tubing after corrosion test standard for VSI imaging was cleaned by a method recommended by NACE.[7] The average roughness measured by VSI was 22.7 µm before corrosion and 21.8 µm afterwards, which indicates no change on the steel surface.

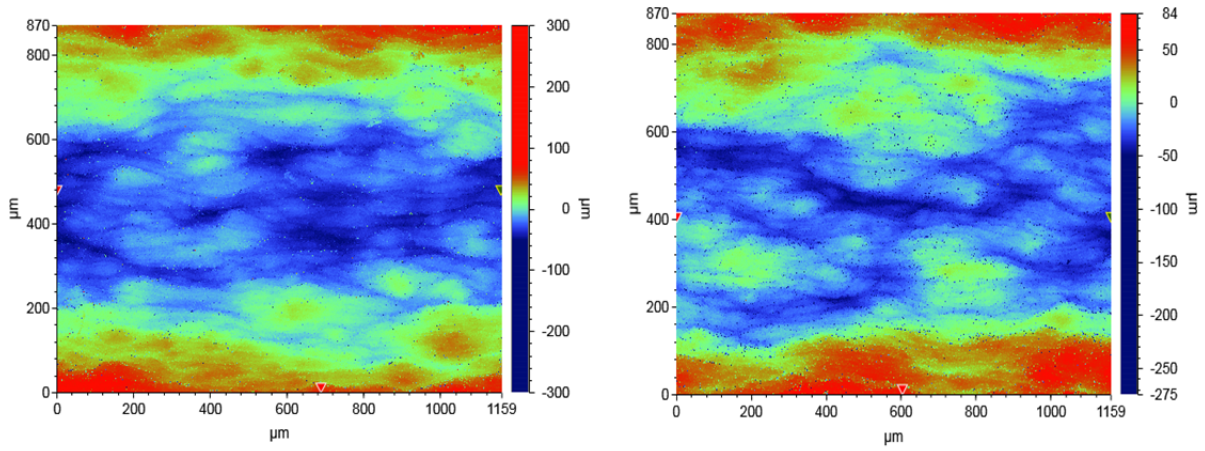

Figure 27. VSI images of the Hastelloy C-276 test tubing inner surface before corrosion test (left) and after (right). Test conditions were 250 °C, 24,000 psig, brine #1 flow-through with flow rate of 0.03 mL/min for three hours.

Figure 28 shows the ICP results for the effluent. It can be seen that the iron and nickel concentration didn't change with time and other metal elements (Mn, Mo, and Cr) all have low concentration in the solution. This indicates that little dissolution of the test tubing occurred during this three-hour test.

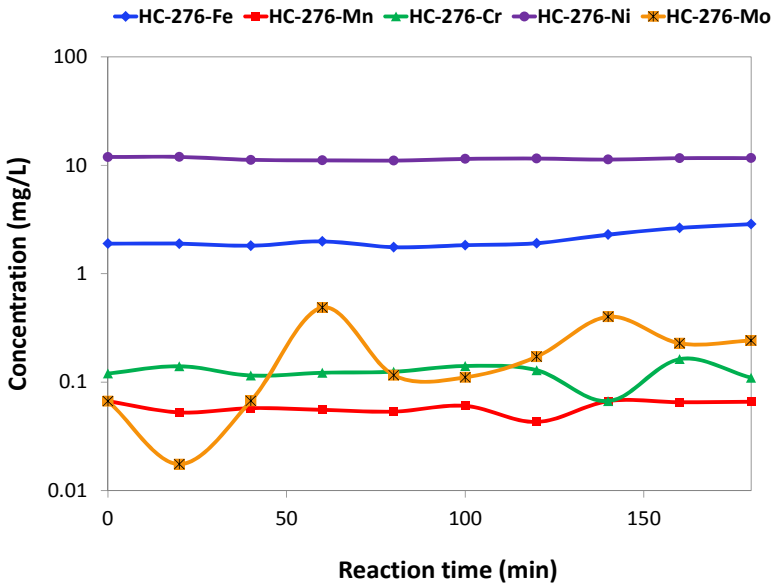

Figure 28. Metal element concentration in the effluent measured by ICP with Hastelloy C-276 test tubing. Test conditions were 250 °C, 24,000 psig, brine #1 flow-through with flow rate of 0.03 mL/min for three hours.

Experiment #2 – 1010 Carbon Steel

Figure 29 shows the C 1010 test tubing surface under SEM before corrosion test (left) and after (right). It shows that after three and a half hours flush with Brine #1 some scales were formed on the steel surface. The deposited materials showed an irregular shape. XRD indicated that the structure of the scales was a mixture of cubic NiO crystals and cubic Fe_2O_3. It was consistent to the NiO standard XRD spectra (PDF# 00-047-1049) and Fe_2O_3 standard XRD spectra (PDF# 00-039-1346). However, as shown in Figure 30, too much noise is present in the XRD spectrum, and therefore a better scale sample is needed for more reliable XRD analysis.

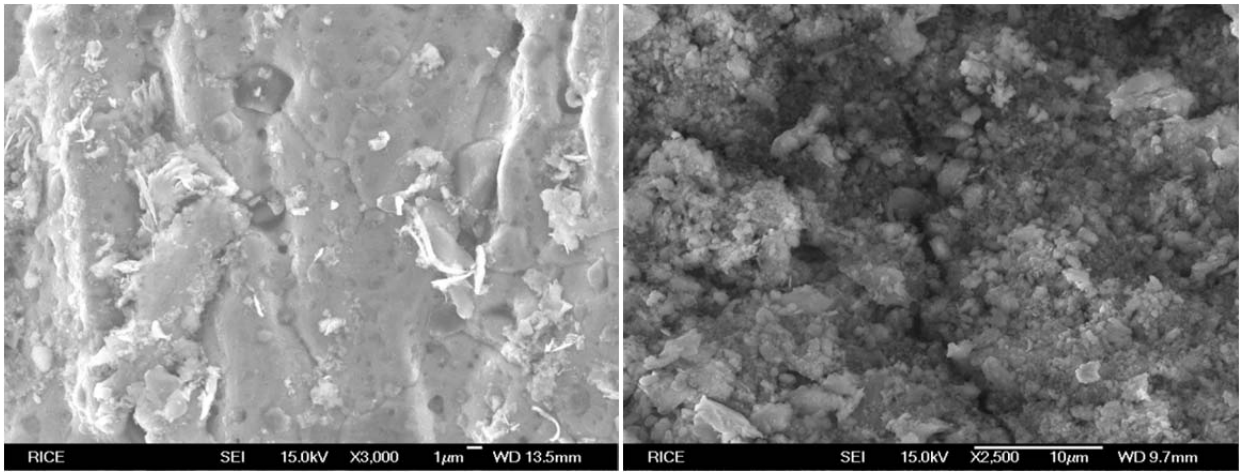

Figure 29. SEM images of the C 1010 test tubing inner surface before corrosion test (left) and after (right). Test conditions were 250 °C, 24,000 psig, brine #1 flow-through with flow rate of 0.03 mL/min for 3.5 hours.

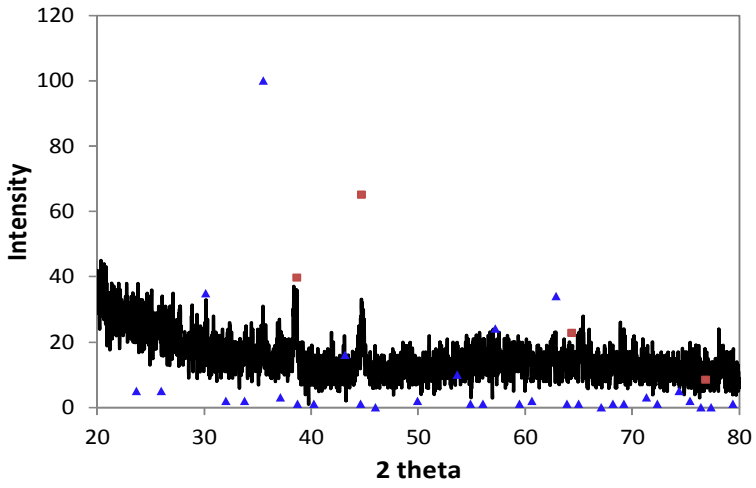

Figure 30. XRD spectrum of the scales formed on the C 1010 test tubing inner surface after corrosion test. Test conditions were 250 °C, 24,000 psig, brine #1 flow-through with flow rate of 0.03 mL/min for 3.5 hours.

Figure 31 shows the VSI images of the test tubing surface before corrosion test (left) and after (right). The test tubing was cleaned after the corrosion test for VSI imaging by a method recommended by NACE standard.[7] The average surface roughness was 14.8 µm before the corrosion test and 16.7 µm afterwards. For the C 1010 test tubing SEM results indicate some general corrosion occurred on the steel surface, but no localized corrosion was observed from VSI analysis. At this stage there was no general corrosion rate measurement applied to the experiments, but only steel surface analysis was available for preliminary understanding of the process. The experiments were designed mainly to confirm the feasibility of test apparatus and procedures. However, a new test coupon design will be

developed to continue this work in Phase II so as to get thorough understanding of the corrosion process at xHPHT.

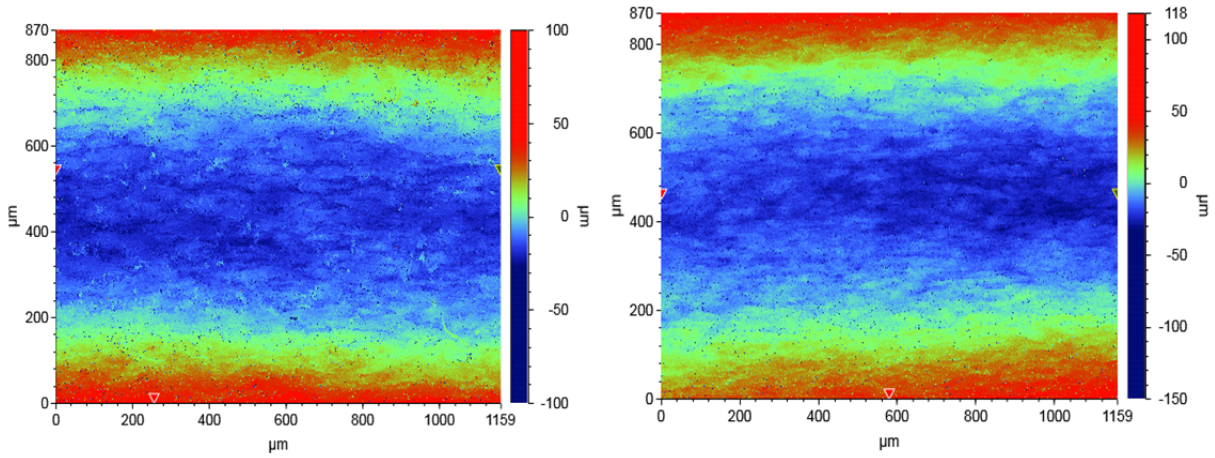

Figure 31. VSI images of the C 1010 test tubing inner surface before corrosion test (left) and after (right). Test conditions were 250 °C, 24,000 psig, brine #1 flow-through with flow rate of 0.03 mL/min for 3.5 hours.

ICP analysis of the effluent is shown in Figure 32. Little change in iron concentration was observed. However, the iron concentration measured in the effluent does not give enough information on the corrosion process because at these test conditions; it is very likely that the C 1010 test tubing was corroded but also formed protective scales on the steel surface, in which case the iron concentration in the solution would not change. This solution's iron concentrations (Fe) are between 10 and 20 mg/L Fe. This is reasonable if it is assumed that the solution is in equilibrium with magnetite (Fe_3O_4), e.g.:

$$Fe_3O_4 + 4H^+ \Leftrightarrow Fe^{2+} + 2Fe^{3+} + 4OH^-$$

More work is needed to establish the solubility of Fe_3O_4 at these xHPHT and salt conditions and will be pursued in Phase II.

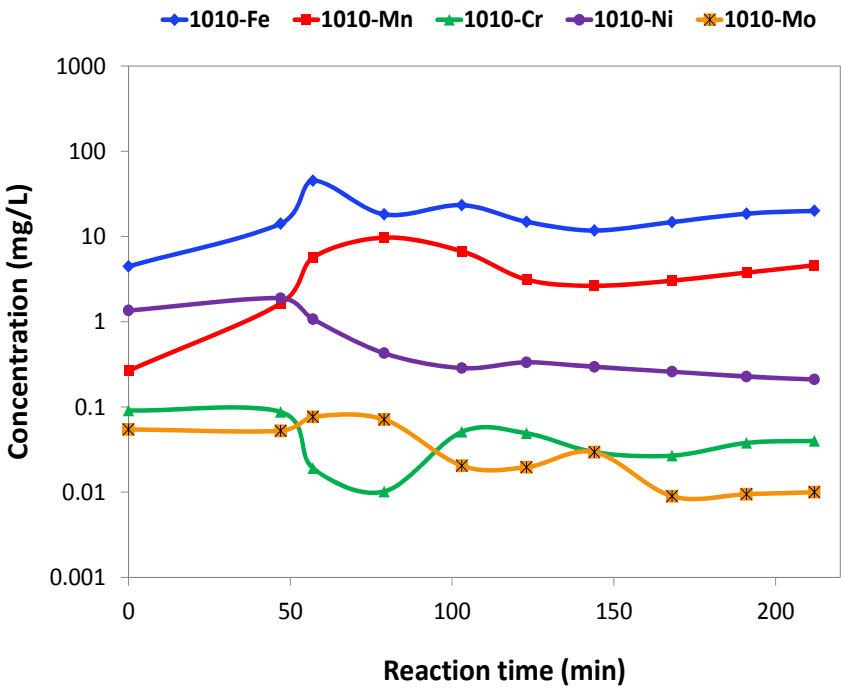

Figure 32. Metal element concentration in the effluent measured by ICP with C 1010 test tubing. Test conditions were 250 °C, 24,000 psig, brine #1 flow-through with flow rate of 0.03 mL/min for 3.5 hours.

Experiment #3 and #4 – SS 316 L in brine #1 and #2

Figure 33 shows the SEM images of a SS 316L test tubing inner surface before (a) and after corrosion test in both brine #1 (b) and brine #2(c). It can be seen that after the corrosion test there was no obvious change of the tubing surface.

Figure 34 shows the VSI images of the inner surface of the test tubing before (a) and after corrosion test (b, c) in the two Brines. The test tubing was cleaned after corrosion test for VSI imaging by a method recommended by NACE.[7] The roughness of the steel surface in brine #1 was 22.6 µm and 24.2 µm for brine #2; both were almost the same as the clean, un-reacted surface, which was 23.8 µm. No indication of corrosion can be seen from SEM and VSI analysis.

ICP analysis of the effluent from brine #1 experiment (left) and brine #2 experiment (right) are shown in Figure 35. Very little change of the metal element concentration in the effluent was found, which also indicates no change in corrosion occurred for SS 316 L steel as the test proceeded.

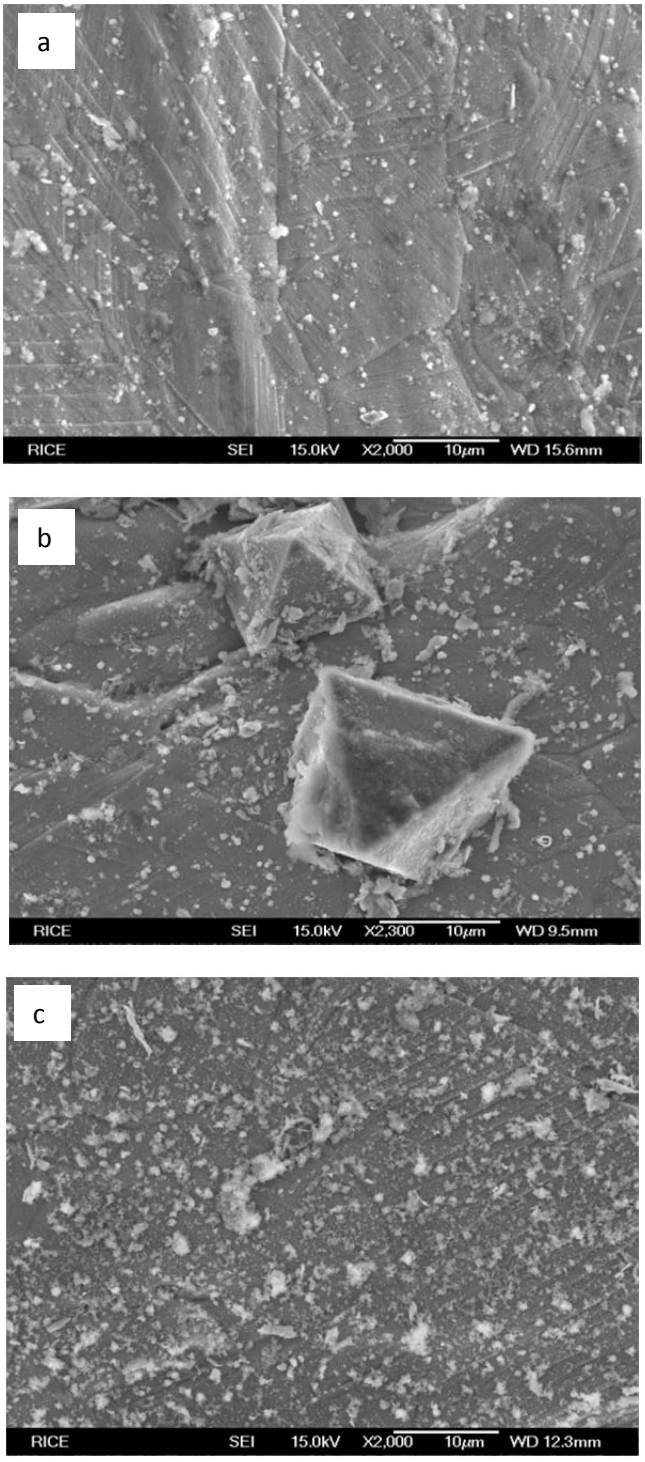

Figure 33. SEM images of the SS 316 L test tubing inner surface before corrosion test (a) and after in brine #1 (b) and in brine #2 (c). Test conditions were 250 °C, 24,000 psig, brine #1 for (b) and brine #2 for (c), flow-through with flow rate of 0.03 mL/min for 1.5 and 3.5 hours, respectively.

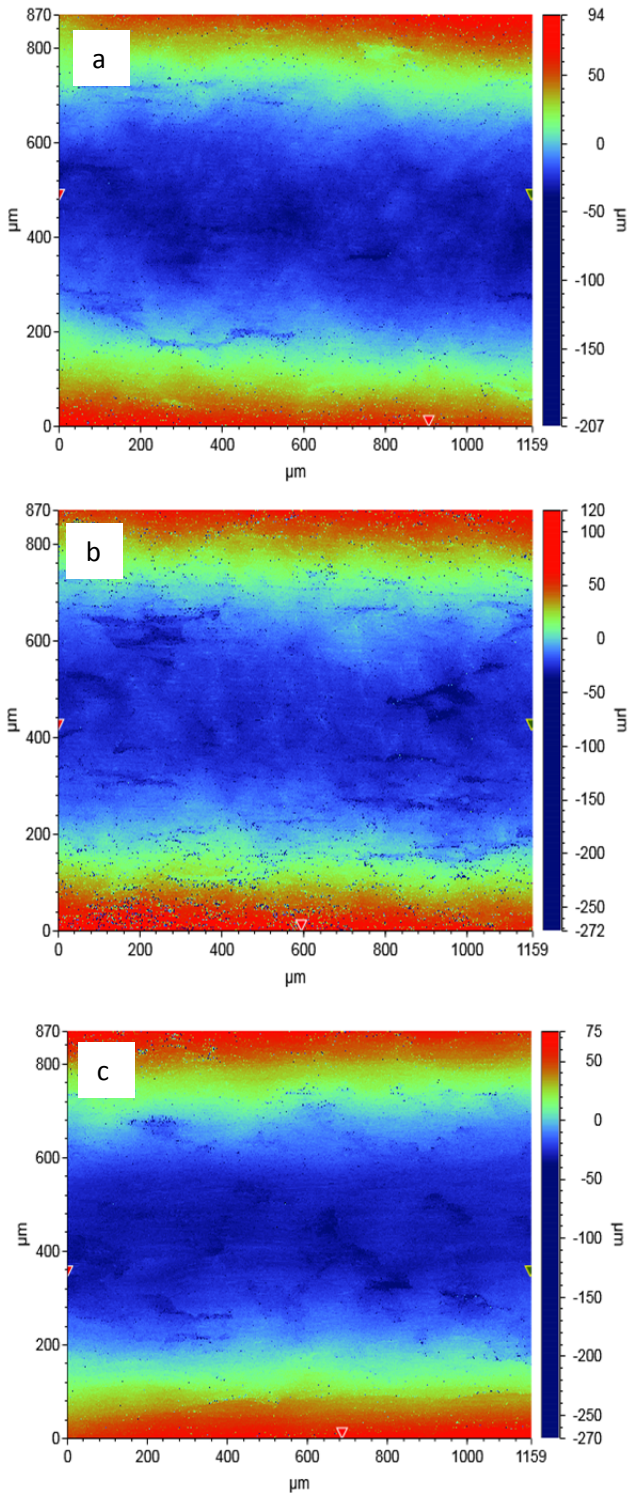

Figure 34. VSI images of the SS 316 L test tubing inner surface before corrosion test (a) and after in brine #1 (b) and in brine #2 (c). Test conditions were 250 °C, 24,000 psig, brine #1 for (b) and brine #2 for (c), flow-through with flow rate of 0.03 mL/min for 1.5 and 3.5 hours, respectively.

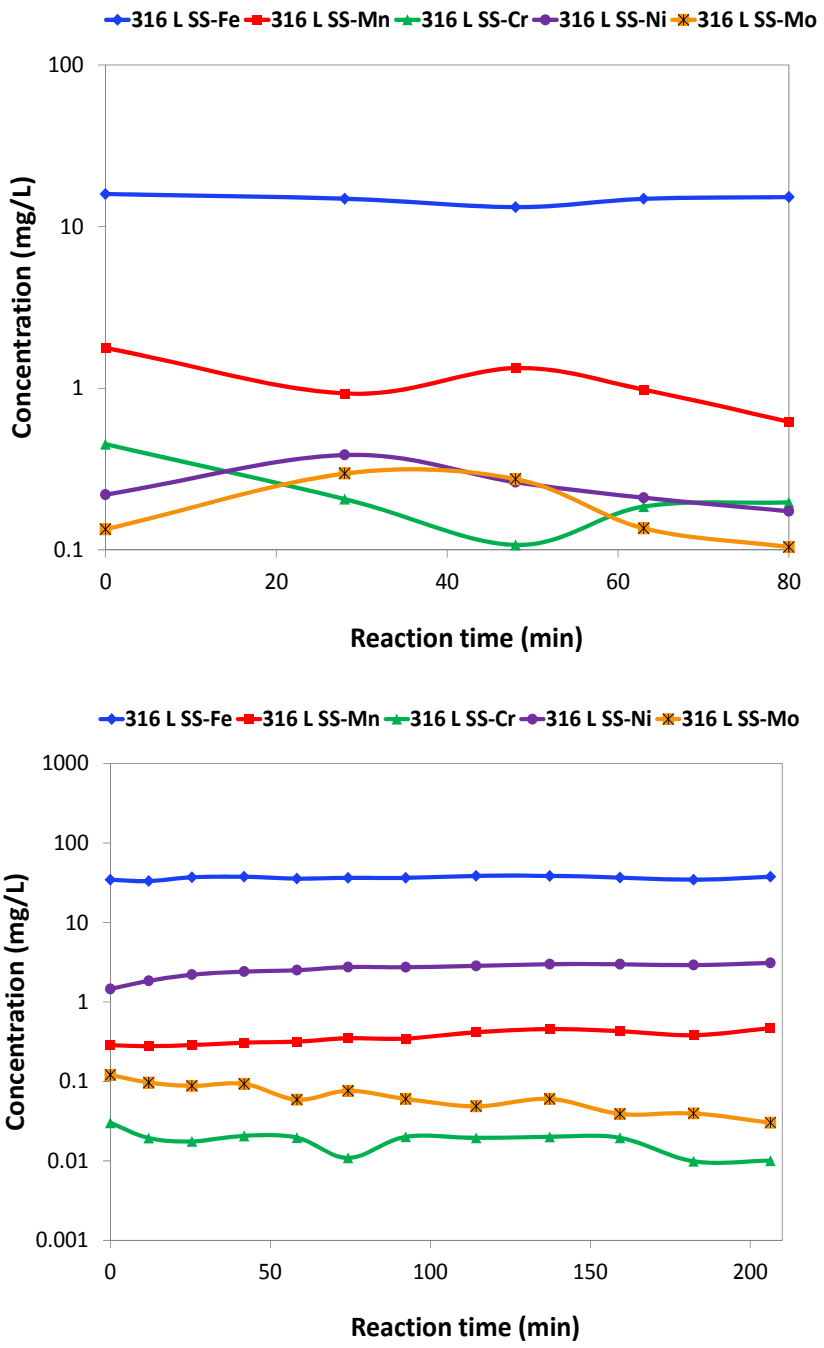

Figure 35. Metal element concentration in the effluent measured by ICP with SS 316 L test tubing. Test conditions were 250 °C, 24,000 psig, brine #1 (left) and brine #2 (right) flow-through with flow rate of 0.03 mL/min for 1.5 and 3.5 hours, respectively.

Conclusions

A preliminary experimental setup for studying corrosion under high temperature (up to 250 °C) and high pressure (up to 24,000 psig) has been developed. It has been shown that corrosion screening of steel samples conducted at these extremes of temperature and pressure can be measured with the

apparatus and test methods developed. Preliminary experimental results showed the feasibility of the experimental apparatus and also indicated the direction of future development. Corrosion rate monitoring and measuring techniques are needed for future work. Using VSI to scan curved metal samples was confirmed to be applicable and will be powerful for localized corrosion analysis for different test coupon surface configurations (e.g., flat or curved). One of the purposes was to start building a database for modeling corrosion under such extreme conditions. Metals including Hastelloy C-276, SS 316 L, and C 1010 were selected for the preliminary tests. However, in coordination with the Working Project Group we will expand the list of metals to be tested in Phase II to include realistic materials used in UDW production.

Subsection 3. Scale Solubility in Flow-Through Apparatus

Introduction

The flow-through apparatus (Figure 36) was designed to test scale dissolution and precipitation kinetics. The experimental setup was highly customized with all wetted parts made of Hastelloy C-276 to resist corrosion at these conditions, as well as two high pressure pumps that can deliver pressurized fluid up to 24,000 psig at constant or variable flow rates. In addition, an air actuated back pressure regulator was used to hold the pressure throughout the system. Hastelloy C-276 tubing with a 0.250 in O.D. and 0.083 in I.D. was used to connect the system. A reactor column with a 0.560 in O.D., a 0.019 in I.D., and a length of 7 in, yielding a pore volume of 0.198 in^3 (3.25 mL), and rated to 30,000 psig was used to ensure safety. The complete volume of the system including the tubing, fittings, and the reactor column was approximately 30 mL, which allowed the solution to equilibrate at temperature and pressure before entering the column where calcite solid was present.

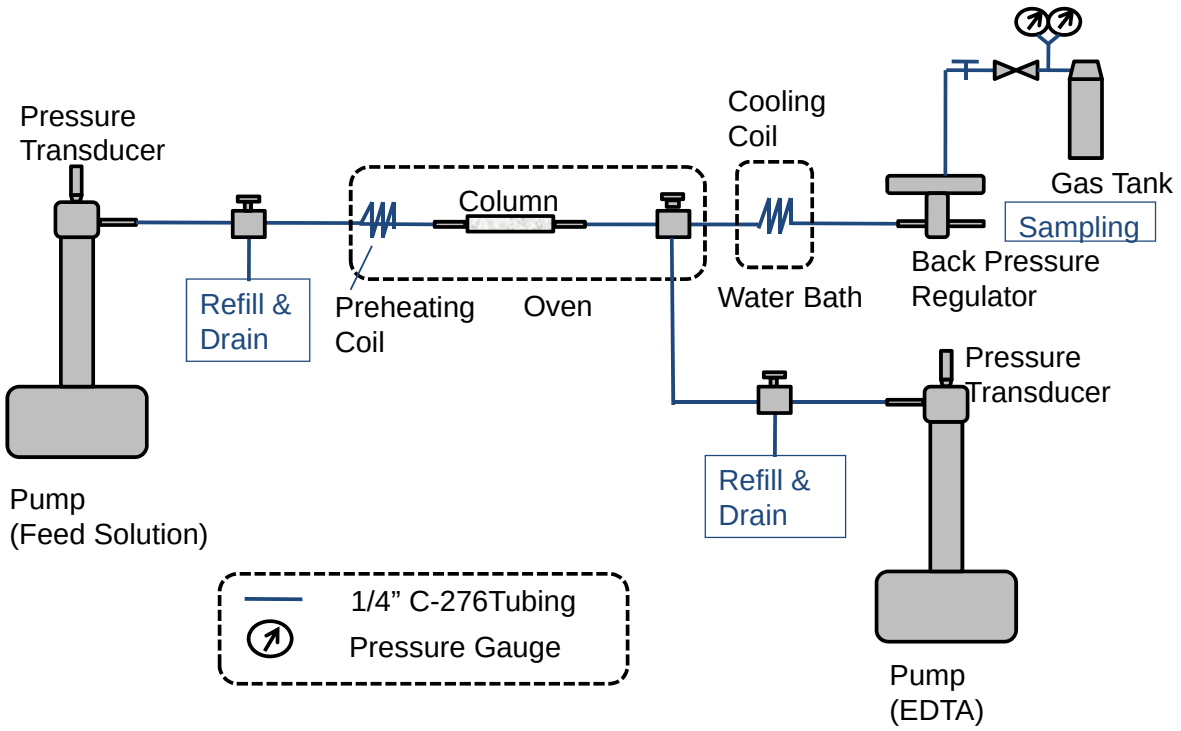

Figure 36. Schematic of the experimental setup for testing of calcite solubility at high temperature and pressure.

Experimental Design

Experiments were initially performed at room temperature to assess the ability of the system to model calcite solubility. Once the system had been tested at room temperature and pressure, subsequent experiments were done at higher temperature and pressure conditions, up to 24,000 psig and 250 °C.

Initial results produced values of Ca^{2+} concentration that were too low compared to the expected equilibrium values calculated using Pitzer theory, so Ethylenediaminetetraacetic acid (EDTA) was added to make sure that the Ca^{2+} was not precipitating in the tubing. This procedure yielded higher Ca^{2+} results and was an effective method to prevent the tubing from blocking. However, Ca^{2+} results yielded higher than predicted equilibrium values. There were two possibilities for this result. The first one was that the calcite particles were being transported by the fluid outside of the rector column and were equilibrating with the fluid outside of the oven at a lower temperature, considering calcite solubility increases with decreasing temperature. The second possibility was that when calcite particles were transported outside of the column, the EDTA was dissolving them and therefore the concentration was higher. To solve these problems, two 0.2 micron high pressure inline filters were installed at the beginning and at the end of the column to prevent calcite solids traveling anywhere outside of the column. This modification to the initial experimental setup proved to be very effective.

Inductively coupled plasma (ICP) standards were, in most cases, diluted with nitric acid (HNO_3) to assure that the sample was digested and the ICP tubing was not blocked or contaminated with solid particles.

This proved to be a challenge since when EDTA is acidified to a pH below 3, it becomes highly insoluble and forms white precipitate. This issue was resolved by making the ICP sample highly basic, to a pH of around 10, with sodium hydroxide (NaOH), before diluting it with HNO_3 to make sure the pH of the sample never got lower than a pH of 3.

Several experiments were run to gain confidence in the setup, and the final set of calcite solubility results can be found in this report under Subtask 7.1 – Validate activity coefficients for carbonate at various HPHT and TDS conditions.

Phase II Recommendations for xHPHT Flow-Through

In the next stage of this research, experiments will be extended to longer test durations and more complex brines (with addition of Fe^{2+}, Ca^{2+}, Mg^{2+}, and others) to see if and how corrosion, both general and localized, would occur.

In Phase I, the ability to test corrosion of different metals under xHPHT conditions was verified. In Phase II, the materials tested will be expanded to include alloys recommended by the working project group, which are used for ultra deepwater development. In addition, higher TDS (up to 6M, i.e. 29.85 wt% NaCl) will be tested to simulate the extreme condition in ultra deepwater wells. Long-term corrosion experiments (i.e., 2 weeks or more) will be performed to assess the effect of exposure time.

A high pressure liquid chromatography (HPLC) pump has been received and will be used in Phase II experiments to extend the exposure time for scale solubility studies as well as inhibitor performance tests.

In addition, the performance of corrosion and scale inhibitors under the same extreme conditions will be studied for thermal stability and decomposition under these extreme conditions. Preliminary corrosion inhibitor assay work has been conducted in Phase I. Experimental setup and equipment have been designed and evaluated. A standard glass cell for electrochemical measurement has been setup for corrosion inhibitor assay testing. Extensive communication has been made with the Working Project Group on which corrosion inhibitors will be tested and studied for this project.

As Phase II begins, the design of the experimental setup will continue to improve to provide more accurate and time efficient measurement techniques. The flow-through apparatus will be modified to include H_2S testing, or experimental work will be performed at an external H_2S testing facility. Scale inhibitors will also be tested for their thermal stability as detailed in Subtask 7.1 of this report.

SUBTASK 6.1 - DEVELOP THE METHODOLOGY TO STUDY CORROSION COUPON BY VARIOUS SURFACE INSTRUMENTS, SUCH AS AFM, TEM, SEM, EDS, AND VERTICAL SCANNING INTERFEROMETRY (VSI)

Summary

One of the goals in Phase I was to develop methodology to study corrosion by surface analysis instrumentation. This task focuses on BCS's use of a vertical scanning interferometer (VSI) with the goal of making it a readily accessible tool to study corrosion. This report first evaluates surface analysis equipment for their suitability to study corrosion, including many microscopy techniques such as VSI, atomic force microscopy (AFM), SEM, and transmission electron microscopy (TEM). It was found that the most significant advantages of a VSI were its large field of view, sub-nanometer Z resolution, ease of sample preparation, and ease of use. Various VSI machines were evaluated. Based on equipment performance, the Bruker Contour GT-K was chosen and used in this project to analyze the surfaces of corrosion coupons. Next, alloy coupons were analyzed with VSI from both the autoclave reactor at temperatures from 50 - 250 °C and 14.7 – 600 psia in a 3 M (15.73 wt%) NaCl solution and the flow-through apparatus up to 250 °C and 24,000 psig in a 3 M (15.73 wt%) NaCl solution. To complement VSI imaging, SEM was also used to analyze surface morphology.

VSI Study of Localized Corrosion

Introduction

In the oil and gas industry, tubing experiences a variety of corrosive conditions during its production lifetime. In many cases, pitting corrosion is not detected until complete penetration occurs. Severe corrosion can shut down production and substantially damage the environment.[10] Having efficient and accurate surface measurements from VSI will provide additional monitoring techniques for corrosion. The ease of use and its applicability to oil and gas production make the VSI ideal, especially for the detection of localized pitting because it has the capability to measure the surface-height of the sample directly. In this project, methodology using a Bruker Contour GT-K was developed for corrosion at xHPHT conditions.

VSI Suitability for Study of Localized Corrosion

Equipment performance and cost of several VSIs from a number of different manufacturers were evaluated and summarized in Table 4. Direct measure of surface-height of the sample and the larger field of view gave a comprehensive surface analysis ideal for localized corrosion measurements. Based on white light interferometry, a 3D non-contact optical microscope can quickly deliver surface measurements over a larger field of view (FOV). VSI is an optical microscope with interferometer mirrors under the objective lens used to monitor fringe contrast. Fringe contrast results from the interferences of light waves as light oscillates down to the sample and back to the detector, or CCD camera. As a light source, dual LED lights are split into two beams. The returning beams are relayed by the beam splitter to the CCD camera. For each pixel on the CCD camera, an interference pattern of the sample surface is

detected. A height value of maximum fringe contrast from interference patterns is given for each pixel. This surface characterization technique yields high-resolution 3D images with vertical resolutions of about 0.1 nm.

VSI comparison to various instruments

Unlike VSI, AFM is a contact method whose tip shape actually defines height resolution. The slow scan across the surface with an AFM probe takes longer than VSI and is limited to the physical size of the probe. Over time, excessive wear on the AFM probe decreases resolution and accuracy. In comparison to VSI, Koyuncu et al showed that when measuring the roughness of filters and reverse osmosis membrane surfaces the AFM and VSI gave different results.[11] Roughness measurements were higher with VSI than measurements from AFM, which may be attributed to the VSI capability to capture large changes in surface height of several microns. Ultimately, the significant advantage of VSI over AFM was the larger FOV with high vertical resolution, time that it takes to scan samples and no degradation in image quality due to wear on tips. Figure 37 shows an example where AFM and VSI work at different scales.

VSI has the most appropriate fast, non-contact optical inspection for height measurements of features in localized corrosion studies when compared with a number of other non-contact instruments (Table 5). In addition, unlike AFM and SEM, VSI is suitable for profiling features with a high aspect ratio, such as steps, pits, holes, and grooves.

At higher magnification and resolution, SEM only renders two-dimensional top view images and provides poor estimation of the height of real surfaces of smaller height gradients. Even though SEM height measurements have been used in the semiconductor manufacturing industry by tilting the surface and using software to assess the depth, these engineered surfaces render data on local surface angles. SEM can also analyze the elemental composition on the surface using energy dispersive spectroscopy (EDS) by bombarding the surface with electrons or X-rays and measuring energy reflected from the surface. Unlike AFM and VSI, SEM cannot render 3D images. In Task 6.0 of this report, SEM was used alongside VSI in order to image the morphology of scale and corrosion deposits on the surface to identify formations at different temperatures.

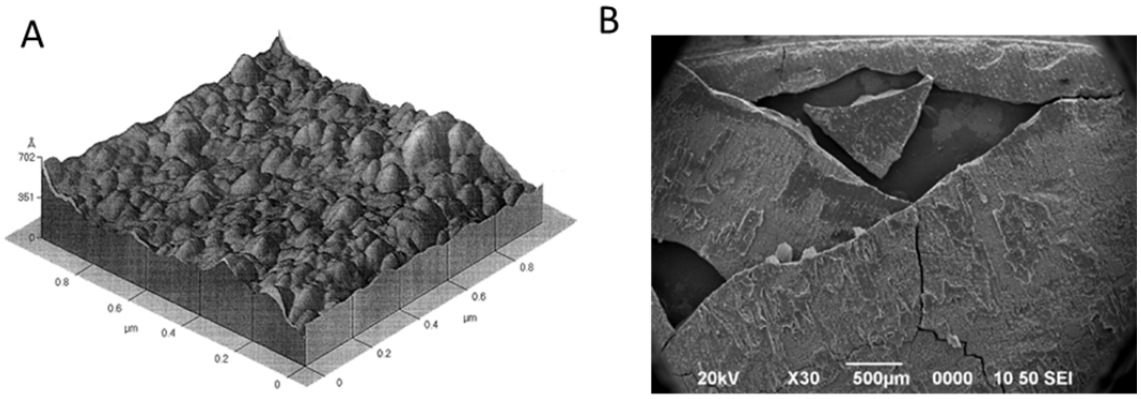

Figure 37. AFM and SEM work at different scales where AFM probes have a tip radius of 2 to 20 nm for profile and 3D analysis (A) and SEM can have a field of view of 1-2 mm for 2D surface analysis (B). (Image from Sun et al., ExxonMobil, NACE 11080). Using white light interferometry, VSI can measure samples (mm^2) faster at a scan speed of 28.1 µm/s than AFM and over a larger surface area (with up to a 5 mm field of view) than SEM.

Lastly, an analysis of TEM as a possible tool was conducted. TEM requires the operator to permanently embed samples into an epoxy resin. Sample preparation for TEM requires a significant amount of time and highly specialized skills to embed samples into the resin without damaging the structure of the sample. In addition, ultra-microtoming the embedded sample into 100 nm thick sections to image with the TEM acquires only information over a sub-nanometer cross-section. This small amount of information is only useful to visualize and measure the layered deposits of corrosion products and scaling on the surface, which can be valuable, but not for corrosion and pitting studies. Of all three microscopic techniques compared in Table 5, the VSI can inspect the surface for height measurements of features smaller than 500 nm as well as at larger dimensions, without tilting the stage and using special software, therefore VSI should complement existing methods of surface and pit detection.

Pit Depth Analysis

The software used with the Bruker Contour GT-K, Vision 64, has a number of analytic capabilities for measuring surface features such as pits from both 2D profile data and surface morphology 3D data (Table 4).

Surface area and pit depth are two parameters that were used to identify which surface morphology characteristics were pits on the surface of metal coupons using VSI. First localized pitting was defined as a region with at least a top width of 100 μm^2 and a pit depth 5 times larger than the average depth calculated from the corrosion rate using weight loss.[9]

In this study, VSI found and measured pitted regions with a user-set value for surface area of at least 100 μm^2 (any region with a smaller value was not included), created a list of pits sorted by size, and used them for statistical analysis. However, the VSI only has one user-set parameter that allows the operator to specify the surface area only and not depth for pit measurements. Next, Microsoft Excel was used to process the VSI data further to remove shallow pits having depths less than five times the value calculated from weight loss.[9]

An advantage of choosing a VSI from Bruker was the ability for the BCS team to work with their engineers to customize the Vision 64 software to be available for the industry's use. This collaboration will be further developed during Phase II. For example, future software development can include incorporating a user-set parameter to filter out shallow pits without having to manipulate the data in Excel. After finding and measuring the pit regions, the software analysis can be customized to show localized corrosion for each pit automatically. Software that is user-friendly and that is used to analyze pitting rate rapidly will allow field operators to use the VSI on location. VSI portability and non-contact measurement technique of surfaces make it time-efficient in comparison to other surface analyzing techniques and complimenting existing approaches.

Furthermore, BCS and Bruker will start to customize the VSI software with predictive models for corrosion, taking into account production temperature and pressure in order to quickly and accurately evaluate the environmental effects on tubing from xHPHT environments. The different types of corrosion products identified, such as Fe_3O_4 and $FeCO_3$, will have an effect on the pitting rate as well. The rate of pitting and localized corrosion can be monitored with VSI. With more data and analysis, modeling the environmental effects on localized corrosion can be further developed to prevent severe damage to the surface.

Table 4. VSI Model Comparison

	Bruker Contour GT-K	Bruker Contour GT-X8	Leica DCM 3D VSI
			
Total Cost	$149,300.61	$287,937.13	$204,868.00
Form Factor	Bench top; vibration isolation table	Integrated air table for vibration isolation	Bench top; vibration isolation table
Capabilities	Imaging, profiles, 3D-topography	Imaging, profiles, 3D-topography	Imaging, profiles, 3D-topography
Modes	Interferometry (PSI, VSI), bright field gray	interferometry (PSI, VSI), bright field color	Interferometry (PSI, VSI), bright field color, Confocal
Objectives	From 5x to 50x, automated turret	From 5x to 50x, automated turret	From 5x to 50x, manual turret, 20x confocal objective as part of base system
Automation	Whole coupon analysis, point analysis	Whole coupon analysis, Point analysis	Whole coupon analysis
Illumination	White LED, Green LED (530 nm)	Proprietary internal laser reference	White LED, Blue LED (460 nm)
Stage	150 mm	200 mm	100 mm
Z Range	100 mm	100 mm	10 mm
Vertical Resolution	0.1 nm	0.1 nm	0.1 nm
Optical Resolution	2.2 µm	2.2 µm	1.08 µm
Scan Speed	28.1 µm/s	92.5 µm/s	20 µm/s

Table 5. Comparison of Different Surface Analysis Techniques

	VSI	AFM	SEM	SEM/EDS	TEM
	Vertical Scanning Interferometer	Atomic Force Microscopy	Scanning Electron Microscopy	Energy Dispersive Spectroscopy	Transmission Electron Microscopy
Model	Bruker Contour GT-K	Digital Instrument Nanoscope IIIA	JEOL 6500F	JEOL 6500F	JEOL 1230 High Contrast
Description	Non-contact optical method for surface height measurement on 3-D structures with surface profiles varying between a few micrometers and centimeters, with 0.1 nm vertical resolution	Spatial resolution is on the order of 100 nanometers, or 1000 times more than the optical diffraction limit, with 0.3 nm height resolution	Magnification up to 100,000X is attainable, with a spatial resolution of 3 nm.	Elemental analysis on SEM	Magnifications up to 1,000,000x is attainable with a spatial resolution of 0.2 nm
Pros	Precise measurement of wavelength. Extreme accuracy of small distances. No sample preparation	Renders 3D imaging and profile measurements	Non-contact optical method. Imaging and surface topography	Used in tandem with SEM. Qualitative elemental analysis only.	Crystalline orientation analysis can be used to study the lattice structure of scale
Cons	Requires that the microscope be placed on a vibration isolation table.	Contact optical method. Small field of view for analysis. Limited height analysis of features with low aspect ratio	Requires sample preparation and conductive coating on samples. Analysis conducted under vacuum.	Requires extensive calibration for quantitative elemental analysis	Sample thickness must be <10 nm and transparent. Height measurement on cross-sections in epoxy requiring extensive time and skill

VSI Analysis of Localized Corrosion

Figure 38 and Figure 39 show the results of various steps in data acquisition and data analysis. First, data acquisition can be summarized as:

- The operator focused the sample with the microscope objective lenses.
- At low magnification, fringes were found; light intensity and scan height were set.
- The lower left and upper right corners of the area to be scanned were set by the operator. The instrument then scanned together individual measurements into one large topography map of the entire coupon (Figure 38).
- Software identified flat plateaus at various heights in the data in order to estimate pit depth relative to the user-selected zero level.

Duration Effect on Localized Corrosion

For illustration purposes, from the various autoclave reactor experiments performed (see Task 6.0), two separate autoclave reactor experiments under the same conditions at different exposure times were selected to compare the effects on pit growth (Figure 38 and Figure 39). First, after a four hour corrosion exposure at 250 °C, with a 1.0 M (5.5 wt%) NaCl solution with an initial pH of 5.0 and charged with 0.08 M $CO_{2(aq)}$, the surface of a C 1018 mild steel coupon was analyzed by VSI (Figure 38). Corrosion product, identified by XRD as magnetite (Fe_3O_4), deposited on the surface and is seen as dark red regions. The magnetite was also imaged by SEM to show deposition of magnetite on the metal surface (Figure 38B). In Figure 38C, blue regions near the bottom right edge of the coupon were analyzed. Once the valleys were identified and seen in the 3D map, depth was measured by analyzing the profile lines drawn by the operator in the desired region (Figure 38D). From the line profile, a black graph showed a cluster of up to five potential pits on the left and a region without valleys on the right. From weight loss (30 mg), the corrosion rate calculated by CR/WL was calculated to be 21.5 mm/yr. Then from corrosion rate, any depth greater than 49.0 µm (which is five times the calculated height of 9.8 µm from CR/WL) were considered pits.[9] From this observation, no pits were found on the surface (Figure 38E).

In a different experiment using a seperate C 1018 mild steel coupon in the autoclave reactor, VSI measurements after a 24-hour experiment to study the effects of time on pit formation under the same conditions (autoclave reactor, 250 °C, 1.0 M i.e. 5.5 wt% NaCl, 0.08 M $CO_{2(aq)}$ i.e.50 psig CO_2 charged at 25 °C, pH 5.0 initial solution), showed a pit depth increase (Figure 39). The profile graph showed a number of different features measured by VSI (Figure 39A), including the zero level on the left with no pits, a smaller valley feature, a larger pit in the center, and an elevated feature with height on the right side of the surface. Profile lines help quickly assess the surface as it moves along the length of the map (Figure 39B). The VSI can also help determine the shape of the pit as elliptical compared to narrow and deep defined by ASTM standard.[9] From the profile in Figure 39A the large pit can readily be seen to show a depth of 78.2 µm (Figure 39B insert).

In Phase I, these preliminary results showed the suitability of VSI to measure localized corrosion by using pit depth established by the weight loss corrosion rate. Other surface techniques like SEM do not provide any height measurements from 2D images and AFM is a contact technique with resolutions

based on the quality of its tip. VSI can be effectively used to measure localized corrosion with pits of high-aspect ratio and used to calculate the pitting rate. VSI measurements for Phase II will focus on the effects of more complicated brine solutions and varying conditions (as mentioned in Task 6.0) and their effects on localized pitting.

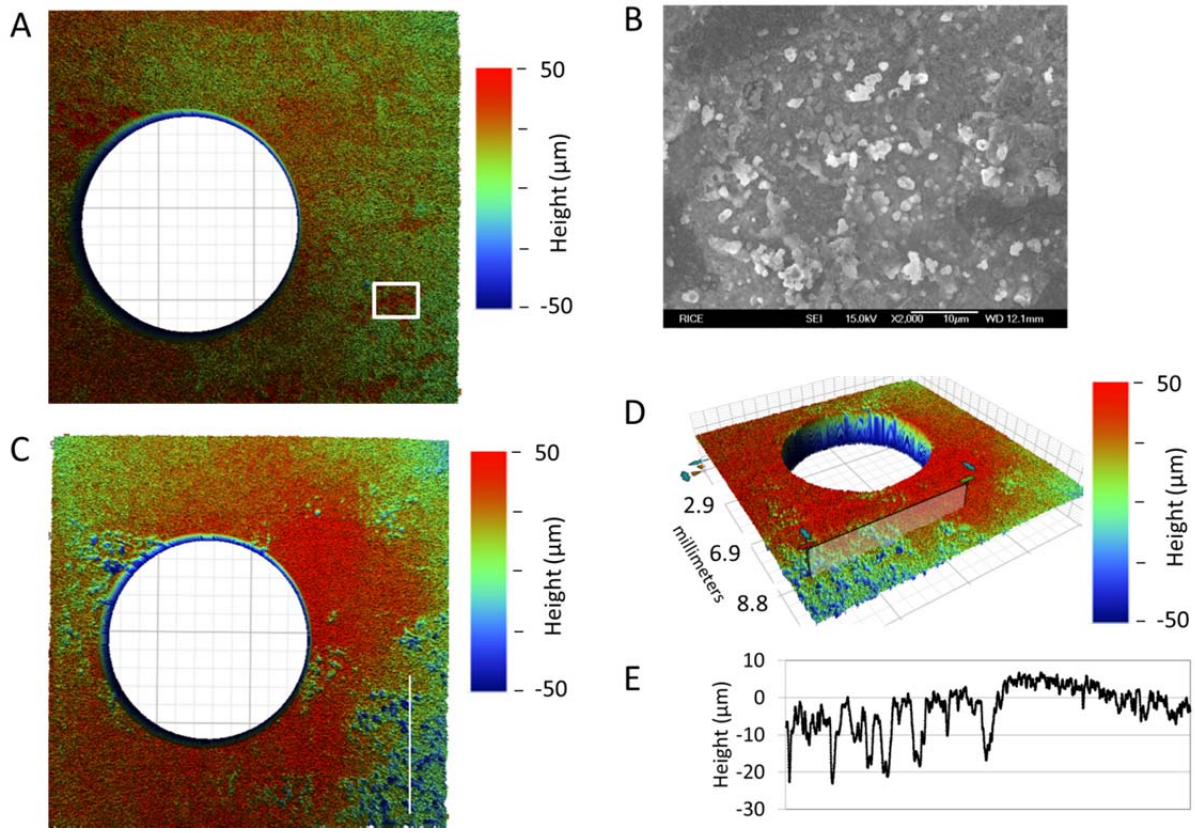

Figure 38. VSI (5x magnification) and SEM surface measurement and analysis. (A) shows a metal coupon with corrosion product on a C 1018 surface after heating to 250 °C in 1 M (5.5 wt%) NaCl solution (0.08 M $CO_{2\,(aq)}$) for 4 hours in an autoclave reactor. From weight loss (30 mg), the corrosion rate by weight loss (CR/WL) was calculated to be 21.5 mm/yr. In the region shown as a white box in (A), corrosion product was imaged with SEM. Here, (B) the SEM image shows the corrosion product on the surface. After a chemical strip following an ASTM protocol.[7] (C) The metal coupon had a different topography (valleys features in blue, lower right). VSI measured valleys with a surface area of at least 100 µm^2 and listed them by depth. Then from CR/WL, any depth > 49.0 µm (9.8 µm x5) were considered pits. (C) No pits were found on the surface. The software can give (D) a profile measurement (black graph) along a user-drawn line (C, white line). The hole used to mount the coupon into the autoclave reactor, was removed from the data.

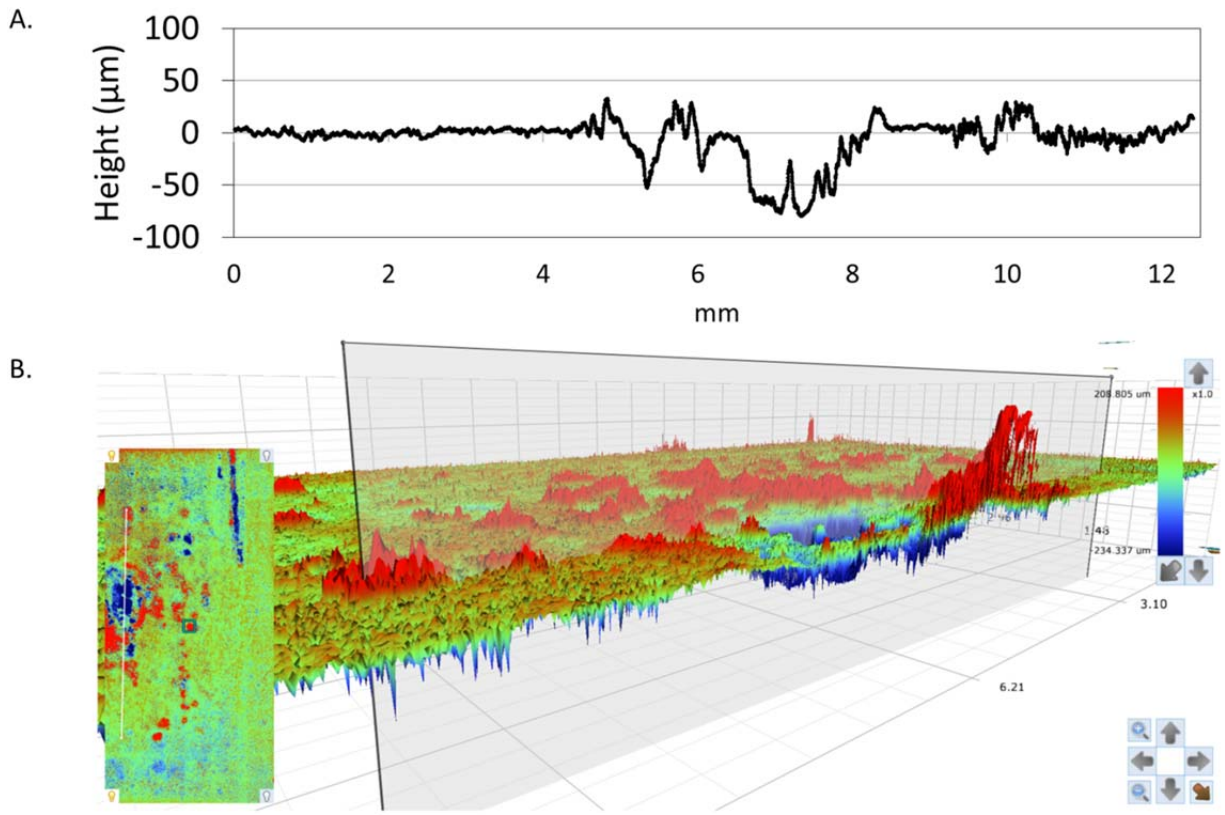

Figure 39. Topography measurement of C 1018 surface by VSI shows the surface after heating to 250 °C in 1 M (5.5 wt%) NaCl solution (0.08 M $CO_{2\,(aq)}$) for 24 hours in an autoclave reactor. From weight loss (35 mg), the corrosion rate by weight loss (CR/WL) was calculated to be 4.2 mm/yr. However, the (A) 2D profile measured a number of valley and features on the surface. From CR/WL, any depth > 58.5 µm (11.6 µm x5) were considered pits. The large pit at the center of the profile was 78.2 µm deep with a pitting rate of 28.5 mm/yr. (B) 3D topography map of a corroded metal coupon illustrates the shape and location of features where the blue region indicates valleys, the green region is the zero, and the red regions are peaks.

Temperature Effect on Localized Corrosion

Figure 40 shows VSI results from a set of experiments testing the effects of temperature on pit depth using an autoclave reactor (see Task 6.0). VSI data analysis can be summarized as follows:

- The VSI analysis of the coupon found flat plateaus at various heights in the data and measured regions relative to a user-selected background level.
- The image map of the VSI coupon is analyzed by the software, which performs a multiple regional analysis with a user-set value with a surface area of at least 100 μm^2.
- Listing the regions of valleys by size and by depth and exporting this list into Excel for additional sorting by pit depth.
- The rate of localized corrosion was calculated for each pit.

In order to test the equipment on measuring valley regions on cleaned C 1018 coupons and calculating the localized corrosion from pit depth, a four-hour experiment in an autoclave reactor at gradient temperatures was conducted (Table 6).[9] Table 6 shows that with an increase in temperature from 50°C to 250 °C, CR/WL increased to 21.5 mm/yr at 250 °C (Task 6.0). Still, no pits formed in the span of this four-hour experiment (Figure 40).[9]

Interestingly, an increase in CR/WL (see Task 6.0) occurred at 100 °C where iron carbonate scale, rather than iron oxide scale was more likely to form (Table 6). As previously discussed in Task 6.0, CO_2 corrosion at HPHT facilitated the formation of magnetite (iron oxide, Fe_3O_4) or iron carbonate ($FeCO_3$) under certain conditions. At low temperatures iron carbonate formed, whereas at increased temperatures magnetite formed, as measured by XRD (see Task 6.0 for discussion). Here, resistance to corrosion by $FeCO_3$ scale was about two times lower than with Fe_3O_4 scale, producing greater weight loss. Thus, this change is more likely due to the transition from $FeCO_3$ to Fe_3O_4 near 100 °C. Experiments indicated that at around 250 °C scale thickness can increase at higher temperatures, becoming more corrosion resistant, as the rate of diffusion of iron from the surface to scale increases. Using the VSI, the thickness of these films formed from corrosion products will be measured in Phase II to study the effects of scaling on the rate of corrosion. Future thermo-kinetic studies in Phase II will elucidate localized corrosion dependence on temperature and the effects of corrosion product formation on the surface.

Table 6. Test conditions and pit depth as a result of temperature and initial solution pH of 5.0. From height derived from CR/WL, minimum pit depth for localized corrosion was calculated by multiplying the height by five. Surface topographies were measured for localized corrosion, but none of these four-hour experiments yielded any pits or localized corrosion (Figure 40).

T (°C)	Time (h)	CO_2 (M)	NaCl (M)	CR/WL (mm/yr)	Height from CR/WL (μm)	Minimum pit depth (μm)	Pits/VSI
50	5	0.08	1.0	6.4	3.7	18	None
100	4	0.08	1.0	46.1	21.1	105	None
150	4	0.08	1.0	9.4	4.3	21	None
200	4	0.08	1.0	19.5	8.9	45	None
250	4	0.08	1.0	21.5	9.8	49	None

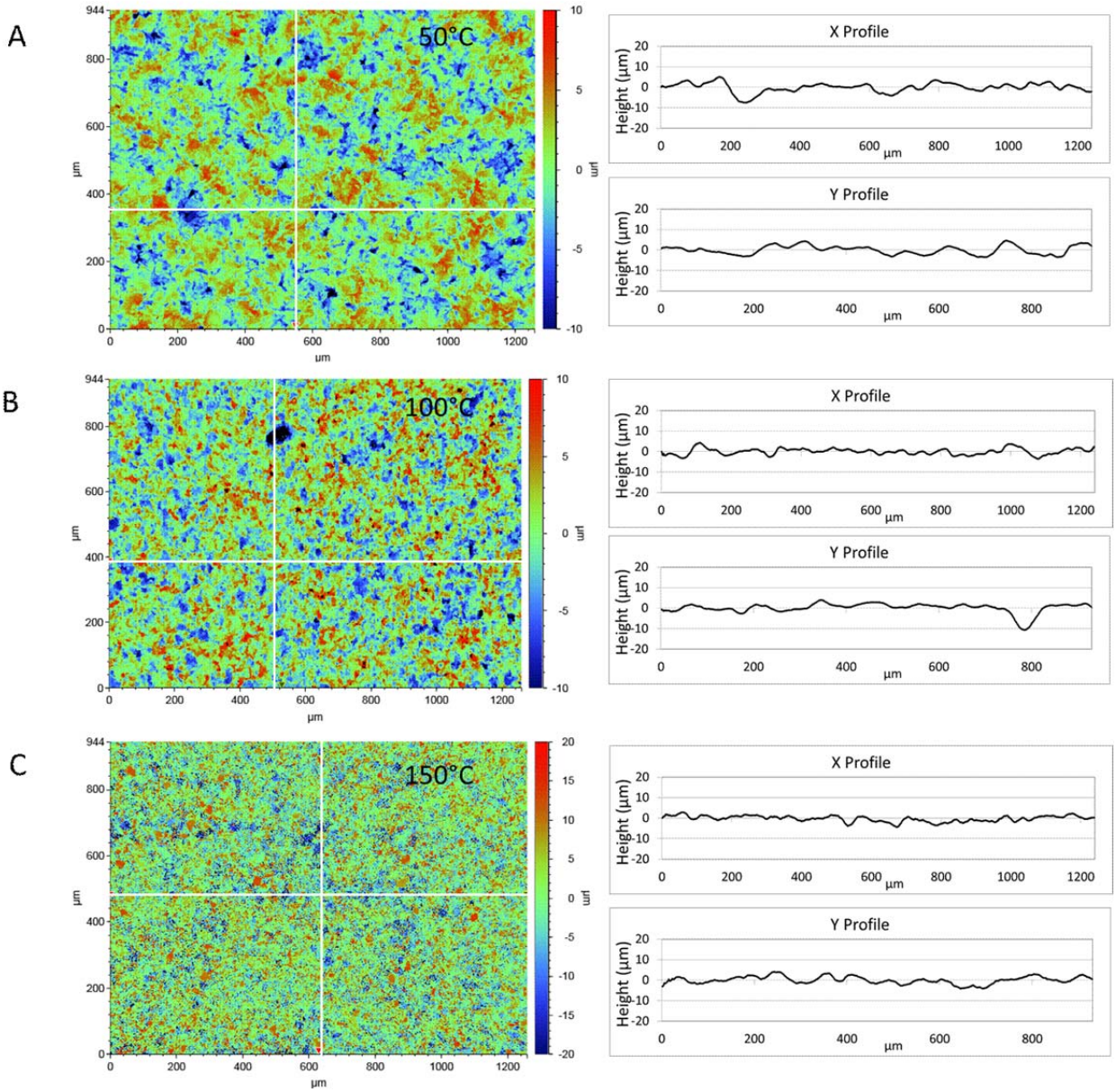
A
50°C
X Profile
Y Profile
Height (µm)
µm
B
100°C
X Profile
Y Profile
Height (µm)
µm
C
150°C
X Profile
Y Profile
Height (µm)
µm

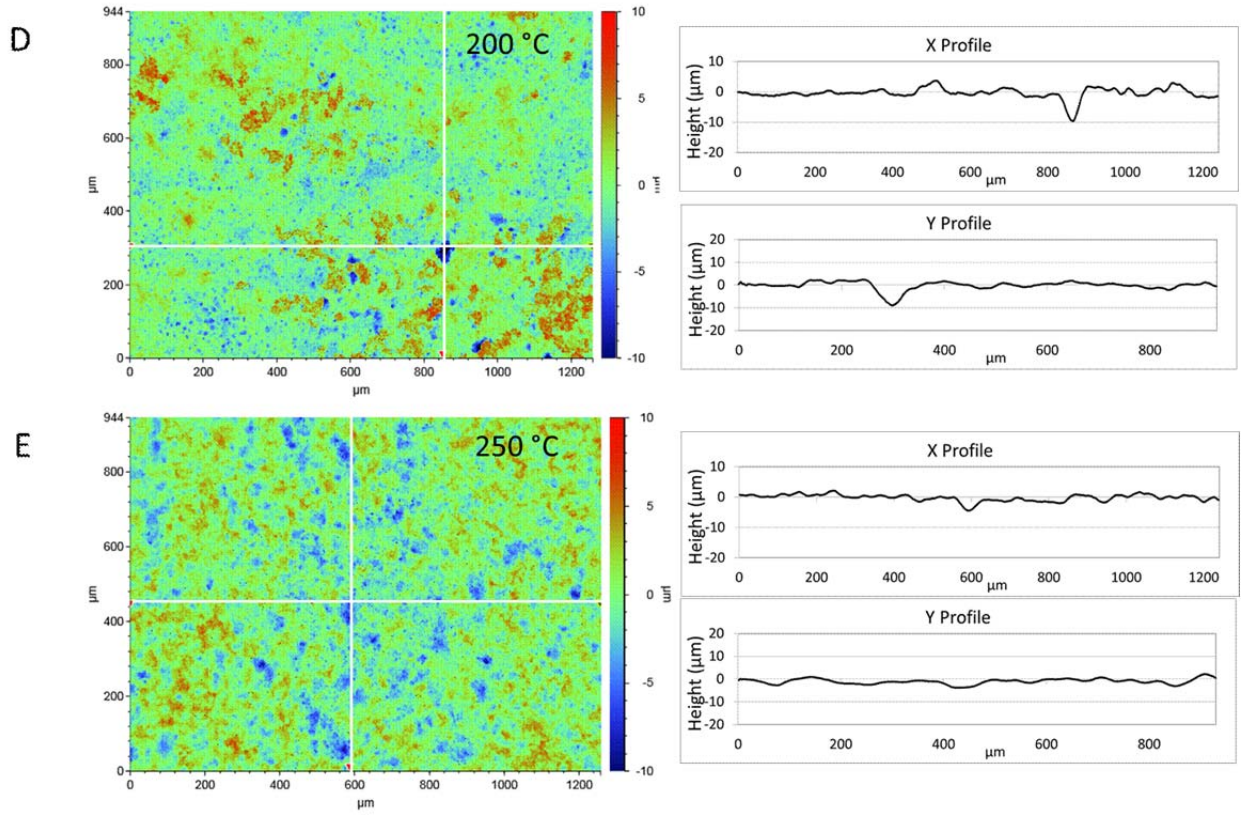

Figure 40. C 1018 corrosion rate dependence on temperature (A) 50, (B) 100, (C) 150, (D), 200, and (E) 250 °C in 1 M (5.5 wt%) NaCl solution (0.08M $CO_{2\,(aq)}$) for 4 hours in an autoclave reactor. VSI 2D images are on the left and profile graphs corresponding to the X and Y axis are on the right.

HPHT Flow-Through Reactor Experiments

The surface topographies of both the initial coupon (Figure 41A-C) and the features created during xHPHT experiments in the flow-through reactor (Figure 41D-F) were measured with VSI. In this experiment three different metals were tested under the same conditions in a continuous flow-through apparatus at 250 °C, 3M NaCl, 24,000 psig for four hours (Table 7). From the profile graphs and SEM images, not much change in post-cleaning surface topography occurred after the flow-through corrosion experiments (discussed further in Task 6.). This technique was developed to measure pitting and changes in topography before and after the flow-through apparatus to determine correlations between changes in the topography and alloy type at xHPHT. No pitting was found by VSI at these initial testing parameters, but numerous other conditions will be explored in Phase II of this project.

Table 7. Test conditions of flow-through experiment at 250 °C, 3 M (15.73 wt%) NaCl, 24,000 psig for four hours. The alloys tested are Hastelloy C-276 (HC 276), stainless steel (SS 316 L), and carbon steel (C 1010).

Alloy	T (°C)	Pressure (psi)	Time (h)	NaCl (M)	Tube I. D. (in)
HC 276	250	24,000	4	3.0	0.084
SS 316L	250	24,000	4	3.0	0.084

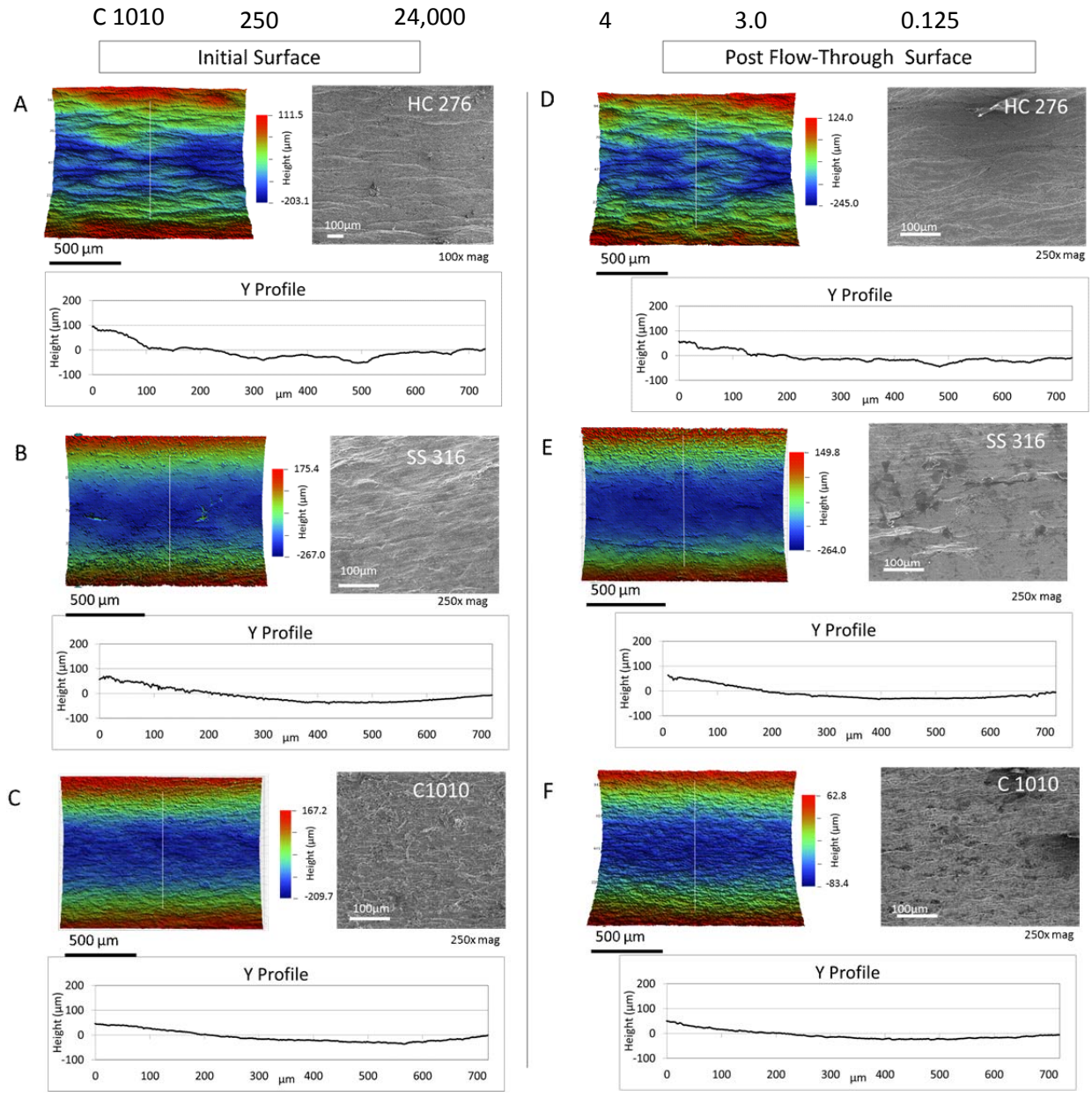

Figure 41. xHPHT experiments in a continuous flow-through reactor at 250 °C in 3 M (15.73 wt%) NaCl at 24,000 psig using tubing (see Task 6). The left side shows VSI images of the initial surface of the inner tubing of three different alloys. On the right, the samples were measured by VSI after the flow-through experiment and after removing any scaling.[7] SEM images (grey images) were also taken. No pits in (A) HC-276, (B) C 1010, and (C) SS 316 L, were found. The line graphs (black) under the 3D plots show no significant change between the topography profile before and after corrosion experiments.

Recommendations for Phase II

Surface topography measurements of metal coupon and tubing surfaces provide important insights on environmental effects on localized corrosion and pitting. Localized corrosion can cause serious damage to field equipment if not monitored accurately. In this report, localized corrosion was measured using data from pits imaged by VSI. VSI and software capabilities can measure pitting, which is not possible with weight loss, LPR experiments, AFM, or SEM. The VSI will be used to monitor changes in surface topography before, during, and after corrosion tests. To make VSI more universal, further evaluation in method development to measure corrosion and scale thickness on flat and curved surfaces will be developed and explored in Phase II. Also in Phase II, more corrosive conditions using hydrogen sulfide (H_2S) and CO_2/H_2S systems will further develop VSI methodology and techniques to make it more applicable to oil and gas production environments.

SUBTASK 7.1 – VALIDATE ACTIVITY COEFFICIENTS FOR CARBONATE AT VARIOUS HPHT AND TDS CONDITIONS

Summary

A preliminary investigation of the process of scale and corrosion at extreme high temperature and pressures were undertaken using the flow-through reactor designed and constructed in Task 6.0 at Brine Chemistry Solution (BCS). Solubility of calcite ($CaCO_3$) was measured in 50 °C increments in temperature range from 100 °C to 250 °C, pressure range from 10,000 psig to 24,000 psig, using the flow-through apparatus containing solid calcite. Prior to collecting the samples at room temperature for analysis and in order to prevent calcite precipitation in the tubing, the effluent was diluted with an ethylenediaminetetraacetic acid (EDTA) solution after the calcite column. The total Ca^{2+} ion concentration in the solution was measured by inductively coupled plasma (ICP). The preliminary experiments were performed in 3 M (15.73 wt%) aqueous solution of sodium chloride, NaCl. To study the ionic strength dependence of calcite solubility, the data set is currently being expanded to include concentrations of NaCl up to 6 M (29.85 wt%). The experimental data from this study for calcite solubility in a concentrated aqueous solution of NaCl at different temperatures and pressures and equilibrium constants from literature were used to construct an activity coefficient model for $CaCO_3$. Pitzer's model was chosen to model the activity coefficients. The pressure and temperature dependence of the model parameters, $\beta^{(0)}_{NaHCO3}$, $\beta^{(0)}_{CaCl+}$, C^{Φ}_{CaHCO3}, and C^{Φ}_{CaCl+}, were studied.

Introduction

Oil and gas reservoirs have been found in unconventional resources including deep and ultra deepwater. The encountered production conditions can experience temperature over 200 °C, pressure over 20,000 psig, and total dissolved solids (TDS) over 300,000 mg/L, making production from these reservoirs challenging due to the limited knowledge of scale and inhibitor behavior at these conditions.[12] Scale prediction requires knowledge of the equilibrium constants and the activity coefficients at the temperatures and pressures of interest, which are lacking in the literature. The deficiency of accurate prediction data regarding scale formation in UDW production can lead to environmental and safety risks, which is one of the main motivations for this study.

Calcite was chosen due to its importance in the oil and gas production [12c] and because its complex dissolution and precipitation processes are closely related to the carbonic acid system. There are various models that predict $CaCO_3$ solubility; however, most of these models are limited in terms of the temperature, pressure, and TDS at which they are applicable, and, in addition, there are considerable differences in the predicted values between existing models.

Reservoir fluid is at equilibrium with calcite rock. As it leaves the reservoir the saturation index (defined as the logarithm of the ion activity product divided by the solubility product) for that solution should theoretically be zero, and this condition was used to model calcite dissolution from a packed column in the present work. It is of great importance to the industry to expand the available knowledge of scale behavior at these extreme conditions in order to accurately predict scale formation and inhibition. Development of UDW resources is currently limited by a lack of precision in the prediction of

thermodynamic and kinetic reactions of the common minerals at extreme temperature and pressure (xHPHT) and high concentration of mixed electrolytes.

Experimental Conditions

Using the flow-through apparatus defined in Task 6.0 of this report, calcite solubility measurements were made at xHPHT conditions.

Naturally occurring Iceland Spar was chosen to represent the $CaCO_3$ crystals present in the reservoir. The calcite was ground and sieved to obtain a uniform particle size of 75-125 µm. A feed solution was prepared to include half of the equilibrium concentration of Ca^{2+} and HCO_3^- at the temperature and pressure of interest for the purpose of not stripping the Ca^{2+} from the column. The solution also contained a high concentration of electrolytes represented by 3 M (15.73 wt%) NaCl and it was equilibrated with CO_2 gas at room temperature and pressure.

To prevent precipitation throughout the tubing as the pressure decreased, EDTA was injected into the system at the temperature and pressure of interest after the solution exited the reactor column. Calcite solubility values were modeled using Pitzer[13] theory to predict the scaling tendency of the system. The equilibrium concentration of Ca^{2+} at temperature, pressure, and NaCl content of interest were calculated using Pitzer theory, ScaleSoftPitzer™ (SSP).[14] The values are listed in Table 8; these values are used as theoretical concentrations for future calculations.

Table 8. Equilibrium Ca^{2+} concentrations calculated using Pitzer theory, SSP [14], at high temperature and pressure.

T (°C)	Pressure (psig)	Equilibrium Concentration (mg/L)		pH
		Ca^{2+}	HCO_3^-	
100	10,000	476.74	1,454.04	5.42
150	10,000	319.13	973.34	5.39
200	10,000	207.61	633.22	5.45
250	10,000	147.03	448.45	5.66
100	15,000	572.17	1,745.13	5.37
150	15,000	379.49	1,157.44	5.31
200	15,000	243.93	743.98	5.35
250	15,000	171.64	523.49	5.53
100	24,000	803.36	2,450.23	5.30
150	24,000	524.99	1,601.23	5.21
200	24,000	334.44	1,020.03	5.21
250	24,000	241.00	737.72	5.37

Methodology

The feed solutions were prepared using $CaCl_2$ and $NaHCO_3$ (ACS grade) in half of the equilibrium value at the temperature and pressure of interest such that the feed solution would contain half of the Ca^{2+} amount needed to reach equilibrium at the target conditions. This ensured that $CaCO_3$ dissolution was not limited by the amount of Ca^{2+} or HCO_3 available in the column. A 0.2 M EDTA solution was prepared with an $MgCl_2$ tracer so that the volume ratio between the feed solution and the EDTA could be accurately calculated and accounted in the final dilution. The feed solution was sparged with pure CO_2 at room temperature and pressure until the pH became constant, so that the solution contained a fixed amount of CO_2 in equilibrium with 97 percent CO_2 in the gas phase, with approximately 3 percent water vapor. The solution was then delivered into the column by the high pressure pumps to interact with the calcite solid particles at the temperature and pressure of interest.

The effect of retention time was studied at room temperature and pressure, and it was found that equilibrium was reached quickly. A flow rate of 0.5 ml/min was chosen, which corresponded to a residence time of 6.5 minutes in the column (3.25mL). Thus, we assumed that reaction kinetics were faster at higher temperature and that equilibrium would be reached faster than 6.5 minutes at higher temperatures.

A sample was collected from the effluent of the back pressure regulator and analyzed using inductively coupled plasma optical emission spectrometry (ICP-OES) for Ca^{2+} and Mg^{2+} concentrations. The concentrations of HCO_3^- and CO_2 were calculated based on the following principles:

The assumed reaction is:

$$CaCO_{3,(s)} + CO_{2,(aq)} + H_2O \rightarrow Ca^{2+} + 2HCO_3^- \quad (1)$$

From the measured Ca^{2+}_{final} concentration, the corresponding values for HCO_3^- and $CO_{2,\,aq}$ were calculated as follows:

$$HCO_{3effluent}^- \,(mM) = m_{HCO_3^-} = HCO_{3,initial}^-(mM) + 2 * \left[Ca_{final}(mM) - Ca_{initial}(mM)\right] \quad (2)$$

$$CO_{2,aq,effluent}(mM) = m_{CO_{2(aq)}} = CO_{2,aq,initial}(mM) - \left[Ca_{final}(mM) - Ca_{initial}(mM)\right] \quad (3)$$

The initial CO_2 concentration was calculated for the feed solution in equilibrium with 97 percent CO_2 at room temperature using Henry's law.

$$CO_{2,aq,initial} = \frac{K_{gw,CO_2} P_{CO_2} \gamma_{CO_2(g)}}{\gamma_{CO_{2(aq)}}} \quad (4)$$

where $K_{gw,CO2}$ is the Henry's constant for CO_2 in water, P_{CO2} is the partial pressure of CO_2 of 0.97 atm. $\gamma_{CO2(g)}$ and $\gamma_{CO2(aq)}$ are the respective activity coefficients of CO_2 in the gas and solution phases. $\gamma_{CO2(aq)}$ is calculated using Pitzer ion interaction theory[13] by the following equation.

$$ln\gamma_{CO_{2(aq)}} = m_{Na^+}\left(2\lambda_{CO_2Na}\right) + m_{Ca^{2+}}\left(2\lambda_{CO_2Ca}\right) + m_{Cl^-}\left(2\lambda_{CO_2Cl}\right) + m_{HCO_3^-}\left(2\lambda_{CO_2HCO_3^-}\right) + m_{Na^+}m_{Cl^-}\left(\xi_{CO_2NaCl}\right) + m_{Na^+}m_{HCO_3^-}\left(\xi_{CO_2NaHCO_3}\right) + m_{Ca^{2+}}m_{Cl^-}\left(\xi_{CO_2CaCl}\right) + m_{Ca^{2+}+}m_{HCO_3^-}\left(\xi_{CO_2CaHCO_3}\right) \quad (5)$$

where γ is the activity coefficient of aqueous species and m is the concentration in molality. λ represents the binary interaction between neutral species and ions, while ξ are for interactions among one neutral species, one cation and one anion. In the system presented in this work, a separate gas phase was not considered because the feed solution contained only dissolved CO_2 which was partially consumed during the calcite dissolution process.

Equilibrium constants K_1 and K_2 were obtained through the following equations from Duan and Li[15]

$$lnK = a_1 + a_2T + a_3T^{-1} + a_4T^{-2} + a_5lnT + (a_6T^{-1} + a_7T^{-2} + a_8T^{-1}lnT)(P - P_s) + (a_9T^{-1} + a_{10}T^{-2} + a_{11}T^{-1}lnT)(P - P_s)^2 \quad (6)$$

where a_1-a_{11} are parameters listed in Table 9, P_s is 1 bar at temperatures below 373.15 K (100 °C) or saturation pressure of water at temperatures above 373.15 K (100 °C) and temperature is in K.

Table 9. Parameters for Equation 6 from Duan and Li. [15]

	Ln K_1	**LnK_2**
a_1	233.516	-151.182
a_2	0.0	-0.089
a_3	-11974.383	-1362.259
a_4	0.0	0.0
a_5	-36.506	27.798
a_6	-45.080	-29.514
a_7	2131.319	1389.015
a_8	6.714	4.420
a_9	0.008	0.003
a_{10}	-0.402	-0.164
a_{11}	-0.001	-0.001

The saturation index (SI) was calculated using the following equation:

$$SI_{CaCO_3} = log_{10}\left(\frac{a_{Ca^{2+}}a_{CO_3^{2-}}}{K_{sp,CaCO_3}}\right) = log_{10}\left(\frac{m_{Ca^{2+}}m^2_{HCO_3^-}}{m_{CO_{2(aq)}}}\frac{\gamma_{Ca^{2+}}\gamma^2_{HCO_3^-}}{\gamma_{CO_{2(aq)}}a_{H_2O}}\frac{K_2}{K_1K_{sp,CaCO_3}}\right) \quad (7)$$

where m_{Ca}^{2+} is the measured Ca^{2+} molar concentration from ICP, and m_{HCO3}^{-} and $m_{CO2(aq)}$ are molar concentrations of HCO_3^- and aqueous CO_2 calculated by equations 2 and 3, respectively. The dissociation constants K_1 and K_2 are defined in Equation 6 above.

The activity coefficients of the species γ_{Ca2+} , γ_{HCO3-} and $\gamma_{CO2(aq)}$ are calculated using Pitzer[16] theory with the use of ScaleSoftPitzer™ [14], which follows the following equations derived by Pitzer Equation 8 and Equation 9.[17]

$$ln\gamma_{Ca^{2+}} = z_{Ca^{2+}}^2 F + m_{Cl^-}(2B_{CaCl} + ZC_{CaCl}) + m_{HCO_3^-}\left(2B_{CaHCO_3} + ZC_{CaHCO_3}\right) + m_{Na^+}(2\Phi_{NaCa} + m_{Cl^-}\Psi_{CaNaCl}) + |z_{Ca^{2+}}|\left(m_{Na^+}m_{Cl^-}C_{NaCl} + m_{Na^+}m_{HCO_3^-}C_{NaHCO_3} + m_{Ca^{2+}}m_{Cl^-}C_{CaCl}\right) + m_{CO_{2(aq)}}\left(2\lambda_{CO_2Ca}\right) + m_{CO_{2(aq)}}m_{Cl^-}\xi_{CO_2CaCl} \quad (8)$$

$$ln\gamma_{HCO_3^-} = z_{HCO_3^-}^2 F + m_{Na^+}\left(2B_{NaHCO_3} + ZC_{NaHCO_3}\right) + m_{Ca^{2+}}\left(2B_{CaHCO_3} + ZC_{CaHCO_3}\right) + m_{Cl^-}\left(2\Phi_{ClHCO_3^-} + m_{Na^+}\Psi_{NaHCO_3Cl}\right) + \left|z_{HCO_3^-}\right|\left(m_{Na^+}m_{Cl^-}C_{NaCl} + m_{Na^+}m_{HCO_3^-}C_{NaHCO_3} + m_{Ca^{2+}}m_{Cl^-}C_{CaCl}\right) + m_{CO_{2(aq)}}\left(2\lambda_{CO_2HCO_3}\right) + m_{CO_{2(aq)}}m_{Na^+}\xi_{CO_2NaHCO_3} \quad (9)$$

where γ is the activity coefficient of the species and m_x is the concentration in molality of species x. B and C are coefficients that represent the interactions between oppositely charged ions, Φ for liked charged ions and Ψ represents the ternary interactions among ions. Z is the total molality of charges in the system and z denotes the charge of an individual species. F is the Debye—Hückel type long range electrostatic interaction term which can be calculated using Equation 10.[18]

$$F = A^{\Phi}\left(\frac{\sqrt{I}}{1+b\sqrt{I}} + \frac{2}{b}ln\left(1 + b\sqrt{I}\right)\right) + m_{Na}m_{Cl}B_{NaCl}' \quad (10)$$

where I is the ionic strength of the solution, B_{NaCl}' is the first derivative of B_{NaCl} with respect to I. A^{Φ} is the Debye-Hückel limiting law slope.[18]

The activity coefficients used for the SI calculation are listed in Table 10. The activity coefficient for $CO_{2,(aq)}$ is calculated to be 2.818 and does not take into account the temperature and pressure dependence. This represents a deviation in the calculation procedure which is being modeled and corrected for by this groups' modeling team at Rice University. It will be further explained in Subtask 7.2 section of this report.

Table 10. Activity coefficients calculated using SSP. [14]

T (°C)	P (psig)	γCa^{2+}	γHCO_3^-
100	10,000	0.252	0.449
100	15,000	0.276	0.459
100	24,000	0.318	0.475
150	10,000	0.168	0.328
150	15,000	0.192	0.338
150	24,000	0.234	0.354
200	10,000	0.104	0.236
200	15,000	0.128	0.247
200	24,000	0.168	0.264
250	10,000	0.061	0.178
250	15,000	0.083	0.191
250	24,000	0.123	0.209

Results and Discussion

Solubility of $CaCO_3$ was measured in the NaCl-CO_2-H_2O system up to 250 °C, 24,000 psig and 3 M (15.73 wt%) NaCl to compare the predicted equilibrium values by three different sets of dissociation and equilibrium constants. There are significant differences in the values reported for the three equilibrium constants K_1, K_2 and $K_{sp,CaCO3}$ at xHPHT conditions.[19]

The equilibrium constants K_1 and K_2 were calculated using Equation 6[20] for the different temperatures and pressure as shown in Table 11. These were used for calculating the SI for all three cases, where P_s is the saturation pressure of water at that temperature.

Table 11. Equilibrium constants calculated using Equation 6 at temperature and pressure.

Temperature (°C)	Temperature (K)	Pressure (psig)	P_s (psig)	ln K1	ln K2	K1	K2
100	373.15	10,000	14.69	-14.07	-22.64	7.73E-07	1.47E-10
100	373.15	15,000	14.69	-13.75	-22.33	1.06E-06	2.01E-10
100	373.15	24,000	14.69	-13.22	-21.81	1.81E-06	3.37E-10
150	423.15	10,000	69.07	-14.71	-23.05	4.07E-07	9.75E-11
150	423.15	15,000	69.07	-14.33	-22.69	5.95E-07	1.40E-10
150	423.15	24,000	69.07	-13.73	-22.09	1.09E-06	2.54E-10
200	473.15	10,000	224.80	-15.63	-23.93	1.63E-07	4.03E-11
200	473.15	15,000	224.80	-15.18	-23.52	2.56E-07	6.09E-11
200	473.15	24,000	224.80	-14.48	-22.83	5.14E-07	1.21E-10
250	523.15	10,000	576.67	-16.74	-25.22	5.39E-08	1.11E-11
250	523.15	15,000	576.67	-16.21	-24.75	9.11E-08	1.78E-11
250	523.15	24,000	576.67	-15.42	-23.98	2.00E-07	3.85E-11

Experimental results are shown in Table 12, for the Ca^{2+} measured concentration, and the calculated $CO_{2(aq)}$ and HCO_3^- concentrations for the different test conditions with temperatures ranging from 100 °C to 250 °C and pressures from 10,000 psig to 24,000 psig, all at 3 M (15.73 wt%) NaCl. The concentration of Ca^{2+} was measured by ICP from the sample taken at the effluent of the back pressure regulator. Concentrations of HCO_3^- and CO_2 were calculated based on their initial concentrations and on the Ca^{2+} measured value. Initial concentration of $CO_{2(aq)}$ was calculated using Henry's Law in Equation 4. HCO_3^- concentration in the effluent assumed 2 moles of bicarbonate are formed per mole of calcium ion based on Equation 1. Also in that table, the Saturation Index (SI) values were calculated using the experimental data and three different sets of equilibrium constants. These three sets of stability constants were evaluated for their ability to reproduce the experimental results obtained in this study.

The first set of data in Table 12 used $K_{sp,CaCO3}$ from Kharaka et al [19], which did not take into account the pressure dependence of the equilibrium constant. The variation for this group was plus or minus 0.54 logarithmic units. For the second set in Table 12, $K_{sp\ CaCO3}$ from Plummer et al [21] was used, which also did not take into account the pressure dependence of the solubility product constant; the resulting deviation was 1.03 log units.

The third set listed in Table 12 also used $K_{sp,CaCO3}$ from Kharaka et al [19], but took into account the pressure dependence of the solubility product constant. These values were taken from Helgeson's values [22] curve fitted vs. temperature and used the pressure values from the same. This set took into account the association between divalent cations and anions (Ca^{2+} - SO_4^{2-} and Ca^{2+} - CO_3^- for examples). Since our experimental data did not contain SO_4^{2-}, it is not necessary to adjust the Pitzer[23] coefficient, but the model used does it automatically. The third set was the closest match to the experimental values, with a mean SI value of -0.11 and a standard deviation of 0.18. This prediction will be further improved by using the model which is being developed and will be explained in detail in Subtask 7.2 section of this report.

Table 12. SI calculated using experimental data at 3 M (15.73 wt%) NaCl and constants from different sources.

Temperature (°C)	Pressure (psig)	Concentrations in the effluent (mmol/kg-H2O) Ca^{2+} ±Std. Dev		HCO_3^- ±Std. Dev		$CO_{2(aq)}$ ±Std. Dev		SI calculated using constant group 1	2	3
100	10,000	7.84	±0.14	19.19	±0.28	17.53	±0.14	0.78	0.47	-0.30
100	15,000	9.31	±0.07	22.13	±0.15	16.06	±0.07	1.07	0.76	-0.30
100	24,000	11.85	±0.42	27.20	±0.85	13.60	±0.42	1.51	1.20	-0.41
150	10,000	6.05	±0.08	14.12	±0.16	17.73	±0.08	0.43	-0.26	-0.16
150	15,000	7.17	±0.49	16.35	±0.98	16.62	±0.49	0.74	0.04	-0.25
150	24,000	10.00	±0.05	22.02	±0.11	13.85	±0.05	1.34	0.65	-0.09
200	10,000	4.42	±0.06	10.26	±0.13	18.28	±0.06	0.02	-1.17	-0.03
200	15,000	5.33	±0.04	12.07	±0.09	17.37	±0.04	0.37	-0.81	0.01
200	24,000	7.99	±0.46	17.40	±0.92	14.78	±0.46	1.11	-0.08	0.09
250	10,000	3.96	±0.09	7.90	±0.18	18.65	±0.09	-0.24	-2.01	0.14
250	15,000	4.43	±0.03	8.85	±0.05	18.17	±0.03	0.10	-1.68	0.10
250	24,000	5.06	±0.05	10.11	±0.11	17.61	±0.05	0.52	-1.25	-0.15
							Mean SI	0.64	-0.34	-0.11
							Std. Dev.	0.54	1.03	0.18

1. K_1 and K_2 from Duan and Li[15] Ksp from Kharaka[19] without pressure dependence

2. K_1 and K_2 from Duan and Li[15] and Ksp From Plummer[21] with no pressure dependence term

3. Duan and Li[15] Ksp from Kharaka[19] with pressure dependence and with β_{CaSO4}[(2)] correction

The main difference between sets 1 and 3 is the pressure dependence. We can see from the results in Table 12 that the mean value using the pressure dependence was closer to zero and that the standard deviation became smaller. Accuracy improved when accounting for the pressure dependence of the solubility constant product.

In Phase II more complex brines will be used which contain other anions that interact with Ca^{2+} or other cations of interest. Particularly, in the presence of sulfate, deviations associated to the interactions between the anion and Ca^{2+} can be corrected by adjusting the $\beta_{CaSO4}^{(2)}$, the Pitzer[13] coefficient corresponding to the interaction between Ca^{2+} and SO_4^{2-}, as a function of temperature and pressure using the following equation (Table 13).[17c]

$$\beta_{CaSO_4}^{(2)} = z_1 + z_2 * T + \frac{z_3}{T} + z_4 * \ln(T) + \left(z_5 + z_6 * T + \frac{z_7}{T} + z_8 * \ln(T)\right) * P + \left(z_9 + z_{10} * T + \frac{z_{11}}{T} + z_{12} * \ln(T)\right) * P^2 \quad (11)$$

Table 13. Coefficients for Equation 11 from Shi. [18]

Coefficients in Equation 11	Value
z_1	3.039E+3
z_2	-5.313
z_3	-4.851E+5
z_4	52.152
z_5	987.226
z_6	0.211
z_7	-3.034E+4
z_8	-166.116
z_9	-1.270
z_{10}	-2.783E-4
z_{11}	39.231
z_{12}	0.214

The adjustment of this term represents one of the many ways that can be used to correct the model. Experimental work and modeling in Phase II will be directed to making the prediction more accurate even in the presence of anions that alter the interactions.

Propagation of Error Calculation

There are several sources of possible error in our experimental setup and calculations. These sources may include the set temperature at the oven, the pressure reading, the constituent concentrations in the feed solution, the measured Ca^{2+} concentration, or the pH reading. We have estimated the errors for each parameter and evaluated the effect they have on the final saturation index (SI) value. We will illustrate how we do the calculations with an example for 171 °C and 7,000 psig.

The overall approach is to calculate the various sources of error, and sum the squares, and then takes the square root of the sum, to obtain the contribution of all sources of error to the final value, shown in

bold in Table 14. Estimated error for each parameter is listed in Table 14 as s_{value}. The contribution of each term is listed under the error column. Based upon a propagation of error formula:

$$Estimated\ error\ in\ SI = \left\{\sum \left(\frac{\Delta \mathrm{SI}}{\Delta \mathrm{Parameter}}\right)^2 \sigma^2_{parameter}\right\}^{1/2} \quad (12)$$

where

$$\Delta Parameter = Final\ value - Initial\ value \quad (13)$$

In the example illustrated in Table 14, SI_{CaCO3} = 1.51 ± 0.08 is obtained based upon the estimated errors for each parameter measured or calculated to determine the final saturation index value.

Table 14. Propagation of error example for SI calculation.

	Initial	Final	SI (final)	Δ SI	Δ SI/ Δ Parameter	(Δ SI/ Δ Parameter^2)	s_{value}	$(s_{value})^2$	(Δ SI/ (Δ Parameter)^2(svalue)^2	error
T °C	171	176	1.5807	0.073	7.3E-03	5.3E-05	5	2.5E+01	1.3E-03	0.037
P psia	7000	7700	1.4341	-0.073	-1.1E-04	1.1E-08	100	1.0E+04	1.1E-04	0.011
Na mg/l	19872	20872	1.4833	-0.024	-2.4E-05	5.9E-10	1000	1.0E+06	5.9E-04	0.024
Ca mg/l	6500	6600	1.5119	0.004	4.2E-05	1.8E-09	325	1.1E+05	1.9E-04	0.014
Cl mg/l	43000	44000	1.5149	0.007	7.2E-06	5.3E-11	2150	4.6E+06	2.4E-04	0.016
Alk mg/l	281	291	1.5368	0.029	2.9E-03	8.5E-06	14	2.0E+02	1.7E-03	0.041
Ac mg/l	0	10	1.4751	-0.032	-3.3E-03	1.1E-05	10	1.0E+02	1.1E-03	0.033
TDS mg/l	70900	71900	1.5077	0.000	1.0E-07	1.0E-14	3545	1.3E+07	1.3E-07	0.000
r	1.045	1.046								
CO_2 %	0.27	0.32	1.4395	-0.068	-1.4E+00	1.9E+00	0.01	1.8E-04	3.4E-04	0.018
pH	7.879	7.811								
pH	7.879	5.360	1.5811	0.073	-2.9E-02	8.5E-04	0.10	1.0E-02	8.5E-06	0.003
CO_2%	0.27	0.223								
Oil B	1000	1100	1.5085	0.001	9.4E-06	8.8E-11	50.00	2.5E+03	2.2E-07	0.000
Brine B	100	200	1.5073	-0.000	-3.5E-06	1.2E-11	5.00	2.5E+01	3.1E-10	0.000
								SUM Sqrs	0.006	
SI initial		**1.507**		**Estimated error in Calcite SI value (SUM SQRT)**					**0.075**	

ICP Measurement Propagation of Error Analysis

In addition to the above propagation of error analysis, we are aware that ICP measurements may have an associated error. We have applied a systematic approach to quantify the error resulting exclusively from Ca^{2+} measurements.

When ICP measures a sample, it performs three individual readings and provides a mean value with an associated standard deviation (SD) from the three readings, the recommended approach to considering this SD is established in Equation 13.

$$SD' = \frac{2*SD}{1.716} \quad (13)$$

where *2* is referred to as the coverage factor that gives an interval having a level of confidence of approximately 95 percent (1.96 at 95%) and *1.716* is the square root of 3 (for three measurements). Three samples were collected for each temperature and pressure and the corresponding SD_1' to SD_3' measured by ICP.

The mean value for each of the three sample results from ICP is averaged to obtain one value for each temperature and pressure, the associated standard deviation from this average is also included in the overall uncertainty as SD_4'.

The overall uncertainty, u_1, from ICP measurement is calculated using the following equation

$$u_1 = \sqrt{SD_1'^2 + SD_2'^2 + SD_3'^2 + SD_4'^2} \quad (14)$$

A comparison of the uncertainties obtained by this method and the standard deviation obtained by only considering the average of the results is presented in Table 15.

The uncertainty is more representative of the error because it takes into account a 95 percent confidence while standard deviations from average results do not. The uncertainty calculations in Table 15 are considerable and may represent errors of up to 20 percent in the measured Ca^{2+} concentration. The importance of precision during dilution, sample collection, and measurement are made clear by using this approach.

Table 15. Standard deviation (SD) and uncertainty calculation (u1) for the Ca^{2+} concentration in the effluent measured by ICP.

T (°C)	P (psig)	SD (mg/L)	u1 (mg/L)
100	10000	0.14	1.488
100	15000	0.07	1.971
100	24000	0.42	1.977
150	10000	0.08	1.531
150	15000	0.49	1.240
150	24000	0.05	1.878
200	10000	0.06	0.599
200	15000	0.04	1.320
200	24000	0.46	1.289
250	10000	0.09	1.357
250	15000	0.03	1.150
250	24000	0.05	1.046

Conclusions

Solubility of $CaCO_3$ was measured in a 3 M (15.73 wt%) NaCl, CO_2-H_2O system up to 250 °C and 24,000 psig to compare the predicted saturation index values derived from various sets of dissociation and equilibrium constants. As can be seen in the results, there were significant differences in equilibrium values calculated using the three different sets of constants K_1, K_2, and $K_{sp,CaCO3}$ at extreme temperature, pressure, and ionic strength conditions. These deviations make scale prediction at extreme temperature and pressure conditions unreliable.

This study evaluates the solubility of calcite at extreme temperature and pressure and ionic strength. From the favorable modeling results of the SI vs. the experimental data, there is confidence that the experimental method used is able to reliably model the extreme temperature and pressure conditions encountered in ultra deepwater drilling. This study expands the current data set available for calcite solubility. On the other hand, the difference in predictions using different models was confirmed, and also a set of solubility constants was selected as the best match for the experimental data. Experimental values were within 0.18 log units of the prediction, which is considered to be extremely accurate at these xHPHT conditions.

Although the adjustment of the $\beta_{CaSO4}^{(2)}$ did not make a contribution in our set of data, if SO_4^{2-} had been present, the adjustment would have helped to reduce the deviations of the model. It is only one of the many possible ways to correct the existing model in the presence of sulfide.

It is known that anions have strong interactions with Ca^{2+} in aqueous solutions ,and the Pitzer [17a] virial coefficients are likely a contribution for error in modeling. These deviations can be eliminated by adjusting the $\beta_{CaSO4}^{(2)}$, the Pitzer coefficient corresponding to the interaction between Ca^{2+} and SO_4^{2-}, as a function of temperature and pressure.[17a] Other species' activity coefficients are also involved in the calculation of SI value and can also be adjusted to better fit the prediction in the presence of other anions.

Due to the complexity of the Pitzer model, a thorough evaluation of the interactions between the different species, as well as the effect of each parameter, are needed to fully represent the actual system. Some evaluations are being performed by other research groups on the subject. This is one of the efforts that will be performed in Phase II of this research project.

Recommendations for Phase II

Overall, the ability to perform scale solubility experiments at high temperature, high pressure, and high TDS conditions has been assessed, and the results obtained are consistent with the limited literature available and are also consistent with the models available. Extending the available results allows for better understanding of the test methodology to assess solubility, dissolution, and inhibition at extreme conditions.

Research will be expanded in Phase II to include the study of sulfides in the system, where the Pitzer [23] coefficient corresponding to the interaction between Ca^{2+} and SO_4^{2-} as a function of temperature and pressure will be adjusted to reduce deviations in the predictions from the model. Research in Phase II will also include $BaSO_4$, $FeCO_3$, FeS, and Fe_3O_4 scales for which, dissolution, precipitation, and inhibition behavior is unknown at these xHPHT conditions. Experiments performed on $CaCO_3$ allowed us to experimentally test the functionality of the designed apparatus at these conditions and to ensure that the results obtained are representative of the actual conditions. More complex brine compositions will also be studied to simulate brine encountered in UDW oil and gas production.

Commercially available inhibitors recommended by the Working Project Group will be tested for their ability to perform at these extreme temperature and pressure as well as more complex brine systems. Thermal degradation of inhibitor performance is a concern for UDW development of resources that will be assessed during research performed in Phase II.

SUBTASK 7.2 – EQUATION OF STATE DEVELOPMENT: APPLICATION TO IONIC SYSTEMS

Summary

One of the key objectives of this project is to develop an equation of state (EoS) based on the extension of the association term of the Statistical Associating Fluid Theory (SAFT), for predicting the thermodynamic properties and the phase behavior of brine-hydrocarbon-acid gas system at conditions of high pressure and high temperature (HPHT).

In the first phase of the project, the Perturbed Chain SAFT (PC-SAFT) equation of state was modified through the incorporation of an additional term based on mean spherical approximation (MSA). This additional term accounts for the electrostatic interactions and was tested for model systems for the prediction of phase equilibrium properties. We demonstrate that the PC-SAFT equation of state is able to predict the water content in the hydrocarbon rich phase of hydrocarbon-acid gas system with greater accuracy when compared to other conventional models. PC-SAFT was then combined with the semi-restricted non-primitive MSA model to predict solubility of acid gas in concentrated brine. Significant progress was made towards understanding the effect of ionic strength on the dielectric properties of polar solvent molecules and the effect thereof, in accurately describing the 'salting out' of nonpolar acid gas molecules. The findings of this report also underscore the limitations of current EoS models and the need for pursuing alternate approaches to the modeling of brine-hydrocarbon-acid gas system. Molecular Dynamics (MD) simulation studies were used as a complementary tool to assist model development and to obtain insights into structuring of solvent molecules in electrolyte systems at HPHT.

We have presented a model (unified theory of electrolytes) for prediction of the standard state (infinite dilution) thermodynamic properties of electrolytes to extreme temperatures and pressures (xHPHT). Standard state thermodynamic properties of aqueous electrolytes give insight into the nature of the ion-solvent interactions. These properties have contributions from ion-solvent and solvent-perturbed solvent interactions. The temperature dependence of the standard state thermodynamic properties are reflective of the effect of temperature on structure of solvent and its influence on the ion-solvent interaction.

This section of the report is organized as three subsections: Section I describes the application of SAFT based EoS model combined with MSA in predicting the solubility of acid gases in brine. We show that the ion-water interactions and contributions due to polar interactions are critical to modeling solubility of acid gases. MD simulation studies of NaCl-H_2O system at HPHT are presented in section II. Partial molar volumes for ions at infinite dilution were calculated from MD simulations for validating the molecular models for water and ions. The ion-water radial distribution function and the water coordination number for ions were obtained at pressures and temperatures of interest. The information on solvent organization around ions is very useful for defining association parameters for EoS models. In section III, we demonstrate the ability of unified model in accurately predicting standard state thermodynamic properties of electrolytes to xHPHT. The electrolytes at infinite dilution can be used as reference system for a SAFT based model as discussed in section I. Understanding the standard state properties is

therefore critical to building an efficient molecular model. The unified model will therefore provide a basis for a molecular model based on associating species.

Section I: SAFT Equation of State for Ionic Systems

Introduction

Chapman et al [24,25,26] derived the SAFT equation of state by extending Wertheim's thermodynamic perturbation theory [27,27,28,28] of first order to mixtures of associating spherical segments forming chains. SAFT is equivalent to a chemical equilibrium theory combined with a material balance developed in classical statistical mechanics. The approach was further extended to include non-spherical molecules and long-range polar interactions.[29,30,31] In the SAFT approach, the Helmholtz free energy is written as a sum of the following contributions

$$A = A^{ideal\ gas} + A^{hs} + A^{disp} + A^{chain} + A^{assoc} + A^{polar} \tag{15}$$

where A^{hs} is the contribution to the free energy from a mixture of hard spheres, A^{disp} is the contribution due to dispersive forces between the segments, A^{chain} is the change in free energy due to bonding the segments to create the molecules, A^{assoc} is the change in free energy due to hydrogen bonding or other strong, short ranged association, and A^{polar} is the contribution to free energy due to long range polar interactions. The details of individual contributions to the free energy are given in the appendix of this report. Briefly, the association term is modeled with short ranged, orientation specific attraction sites on the surface of the segments. The association term Helmholtz free energy for mixtures is written as: [25]

$$\frac{A^{assoc}}{NkT} = \sum_i \mathrm{X}_i \left[\sum_{A_i} \left[\ln \mathrm{X}^{A_i} - \frac{\mathrm{X}^{A_i}}{2} \right] - \frac{1}{2} M_i \right] \tag{16}$$

where X_i is the mole fraction of component i, M_i is the number of the association sites per molecule, and X^{Ai} is the mole fraction of molecules that are not bonded at site, A. The term X^{Ai} can be determined as follows

$$X^{A_i} = \left[1 + \sum_j \sum_{B_J} \rho_i \mathrm{X}^{B_j} \Delta^{A_i B_j} \right]^{-1} \tag{17}$$

where ρ_i is the number density and Δ^{AiBj} is the "association strength" defined as

$$\Delta^{A_i B_j} = d_{ij}^3 g_{ij}(d_{ij})^{seg} \kappa^{A_i B_j} \left[\exp\left(\frac{\varepsilon^{A_i B_j}}{kT} \right) - 1 \right] \tag{18}$$

where $g_{ij}(d_{ij})^{seg}$ is segment radial distribution function approximated with a hard sphere distribution function as

$$g_{ij}\left(d_{ij}\right)^{seg} \approx g_{ij}\left(d_{ij}\right)^{hs} = \frac{1}{1-\zeta_3} + \frac{3d_{ii}d_{jj}}{d_{ii}+d_{jj}}\frac{\zeta_2}{\left(1-\zeta_3\right)^2} + 2\left[\frac{d_{ii}d_{jj}}{d_{ii}+d_{jj}}\right]^2 \frac{\zeta_2^2}{\left(1-\zeta_3\right)^3} \tag{19}$$

and

$$\zeta_n = \frac{\pi}{6}\rho\sum_i x_i m_i d_i^n \qquad\qquad n \in \{0,1,2,3\} \tag{20}$$

Within the framework of the Barker and Henderson's perturbation theory,[32] for a reference hard sphere fluid the temperature dependent segment diameter $d_i(T)$ is given as

$$d_i(T) = \sigma_i\left[1 - 0.12\exp\left(-3\frac{\varepsilon_i}{kT}\right)\right] \tag{21}$$

where ε_i is the depth of the square well interaction potential, σ_i is the segment diameter, and k is the Boltzmann constant. The mixing rules for the association energy, ε^{AiBj}, and the effective association volume, κ^{AiBj}, are

$$\varepsilon^{A_iB_j} = \frac{1}{2}\left(\varepsilon^{A_iB_i} + \varepsilon^{A_jB_j}\right) \tag{22}$$

$$\kappa^{A_iB_j} = \sqrt{\kappa^{A_iB_i}\kappa^{A_jB_j}}\left(\frac{\sqrt{\sigma_{ii}\sigma_{jj}}}{0.5\left(\sigma_{ii}+\sigma_{jj}\right)}\right)^3 \tag{23}$$

Gross and Sadowki [33,34] derived a set of equations for the attractive part of the dispersion contribution based on Barker and Henderson's perturbation theory,[32] the details of which are given in the appendix of the report. This formulation of SAFT with dispersion contribution came to be known as Perturbed Chain-SAFT model or PC-SAFT.[33,34]

Debye-Hückel (DH) theory [35] was the first significant statistical approach to describe electrolyte behavior, where ions were represented by point charges with solvent treated as a dielectric continuum. The theory incorporates a truncated Taylor series expansion term for Poisson-Boltzmann equation and is valid at low concentration (< 0.01 M) and for symmetrical electrolytes. However, at concentrations of interest (~4 - 6 M) the DH theory shows significant deviations. The lack of ion specific parameters was another major limitation of the original DH theory. Friedman extended the Debye Hückel model by including short-range repulsions between ions to develop the Primitive Model.[36] Integral equation approaches such as hypernetted chain (HNC) [37] and mean spherical approximation (MSA) [38] as closure functions have been used to solve Ornstein-Zernike [39] equation for electrolyte solutions. Although the HNC method is more accurate, it is mathematically complex and does not have an analytical form of solution. Lebowitz et al [40] and Blum [41] have independently derived analytical solutions for the primitive models for MSA. In the restricted primitive model (RPM), the volume effects of ions in the dielectric continuum are treated with equal sized hard spheres (**Error! Reference source not found.**(a)). When the

asymmetry in the ion sizes is taken into consideration, the model is called non-restricted primitive model or simply primitive model (Figure 42**Error! Reference source not found.**(b)). Adelman et al [42] and Blum et al [43] derived MSA expressions to explicitly account for solvent as equal sized ions and dipolar hard spheres. This model is known as semi-restricted non-primitive model (Figure 42**Error! Reference source not found.**(c)). Wei and Blum [44] later extended the MSA expressions to incorporate the asymmetric hard spheres for ion specificity to develop the non-primitive or civilized model (Figure 42 (d)). The solution of the non-primitive model includes three types of interactions: ion-ion, ion-dipole, and dipole-dipole interactions. Due to the treatment of ions as hard spheres, MSA models can be combined with SAFT based EoS. Recently, various equations of state based on SAFT and CPA [45] were combined with DH and MSA for describing electrolyte behavior.

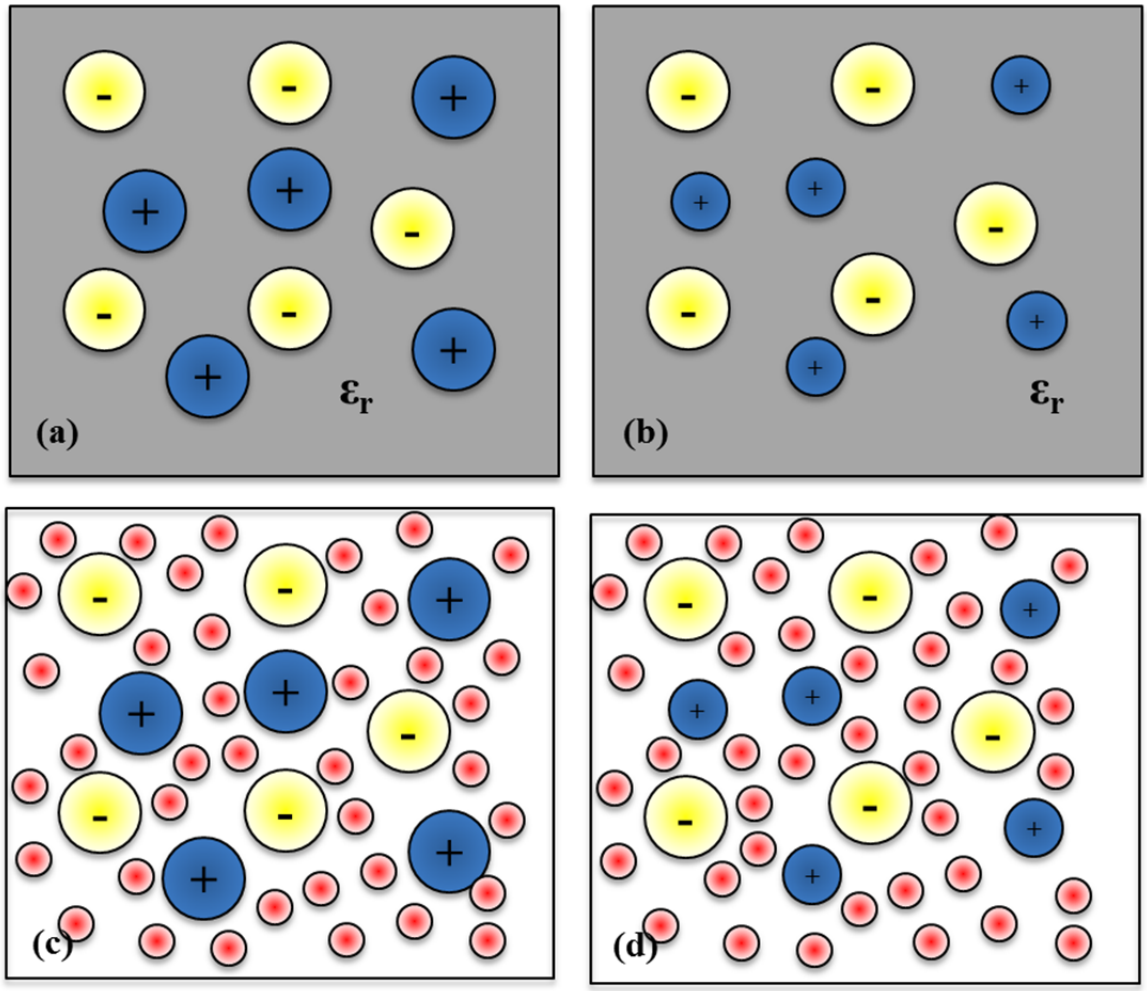

Figure 42. Schematic representation of various models for mean spherical approximation: (a) Restricted Primitive Model, ε_r being the dielectric constant of the continuum, (b) Primitive Model, (c) Semi-restricted non-primitive model, solvent molecules represented by red spheres, and (d) Non-primitive or civilized model.

Table 16 presents a select list of such models available in the literature. The presence of ions in water results in disruption of hydrogen bonding network due to solvation of both cations and anions by the

water molecules.[46] As the ionic concentration increases, the degree of hydrogen bonding in water decreases and the number of water molecules associated with ionic species increases. The structural framework of water, affected by changes in temperature and ionic concentration, dictates the behavior of electrolytes.[47] Llano-Restrepo and Chapman [48] demonstrated in Monte Carlo simulations of ions in water that the civilized model showed good agreement with X-ray data for structure and hydration numbers for ion pairs and solvent separated ion pairs. A civilized model is required to model the steric effects, the hydration effects, and the ion association, as opposed to a Primitive Model in which structure related information are obviated and lumped into the dielectric properties of the continuum model.

Table 16. A brief summary of electrolyte SAFT models in literature.

SAFT Version	Authors	Electrolyte Model
SAFT-VR	Patel et al [49]	Restricted Primitive MSA
	Behzadi et al [50]	Non-primitive MSA
	Zhao et al [51]	Non-primitive MSA
PC-SAFT	Cameretti et al [52]	Debye and Hückel
	Herzog et al [53]	Semi-restricted Non-Primitive MSA
SAFT-LJ	Sun and Dubessy [54,55]	Restricted Primitive MSA
CPA (Peng-Robinson)	Wu and Prausnitz [56]	Restricted Primitive MSA
CPA (SRK)	Lin et al [57]	Primitive MSA

Model and Theory

In Phase I of the project, PC-SAFT combined with semi-restricted non-primitive MSA (NPMSA) model was used to account for columbic and dipole interactions with the model parameters being described by Herzog et al.[53] Briefly, the Helmholtz free energy for an electrolyte system can be written as contribution from the following components

$$A = A^{ideal\,gas} + A^{hs} + A^{disp} + A^{chain} + A^{assoc} + A^{NPMSA} \quad (24)$$

where A^{NPMSA} is the free energy contribution due to electrostatic interactions calculated using a semi-restricted non-primitive MSA model. This contribution is constituted of three individual components as

$$A^{NPMSA} = A^{CC} + A^{DD} + A^{CD} \quad (25)$$

where the superscripts *CC*, *CD*, and *DD* correspond to contributions to free energy due to charge-charge, charge-dipole and dipole-dipole interactions, respectively. It should be noted that the polar contributions due to solvent are treated within the MSA framework, and hence the A^{polar} term is not included in the formulation. In the NPMSA model, the following set of three non-linear equations are solved to yield three dimensionless energy parameters b_0 for ion-ion interactions, b_1 for ion-dipole, and b_2 for dipole-dipole interactions:

$$\begin{aligned} 0 &= a_1^2 + a_2^2 - d_0^2 \\ 0 &= a_1 k_{10} - a_2(1-k_{11}) - d_0 d_2 \\ 0 &= k_{10}^2 + (1-k_{11})^2 - y_1^2 - d_2^2 \end{aligned} \tag{26}$$

where d_0^2 and d_2^2 represent the charge and dipole densities of the solvents respectively and are given as:

$$\begin{aligned} d_0^2 &= \frac{4\pi}{kT} e^2 \sigma_{ion}^2 \sum_j \rho_j z_j^2 \\ d_2^2 &= \frac{4\pi}{3kT} \mu_{D,solv}^2 \rho_{solv} \end{aligned} \tag{27}$$

where σ_{ion} is the single ion diameter solely used for the semi-restricted NPMSA term whereas individual ion size parameters (equal to Pauling radius [58] of the ions) were handled in the PC-SAFT EoS. The dipole moment of the solvent molecule $\mu_{D,solv}$ is an important parameter used in this model. From Herzog et al[53] water was modeled as a spherical segment with two association sites with a dipole moment $\mu_{D,solv}$. The parameters for water, fitted to vapor pressure and liquid density data of water between 0 °C and 340 °C, were used. Carbon dioxide was modeled using parameters from Gross and Sadowski.[34] The water and CO_2 parameters are summarized below in Table 17.

Table 17. Pure component parameters for water and carbon dioxide in SAFT+ NPMSA. Water was modeled with two sites and the dipole-dipole contributions were accounted using MSA. No association or polar contributions were used for carbon dioxide.

Component	Segment Number	Segment Diameter	Dispersion Energy	Association Energy	Association Volume	Dipole Moment (NPMSA)
	m	σ (Å)	ε/k (K)	ε^{AB}/k (K)	κ^{AB}	$\mu_{D,solv}$ (D)
Water	1	2.98	199.74	1937.52	0.0654	2.28
Carbon Dioxide	2.0729	2.78	169.21	-	-	-

As mentioned earlier, the ion diameters for PC-SAFT are the same as Pauling crystal diameters and the single ion parameter for NPMSA was adjusted to the mean ionic activity coefficient and osmotic coefficient data at 25 ^{o}C. Dispersive interactions between the ions were not considered. The dispersion energy parameter for the individual ions, ε_i, is obtained from the relationship of Mavroyannis and Stephen [59] and is used to describe the ion-water dispersion, ε_{ij}, using the Lorentz–Berthelot [60,61] combining rules. These parameters are described in Herzog et al. In addition to the dispersive interactions, PC-SAFT+ NPMSA model also included association interactions between cations and water in A^{assoc}. In Phase I we focused on the sodium chloride system. The sodium cation was modeled with four association sites. The association volume, κ^{AB}, was fixed as 0.03, and the association energy was adjusted to the mean ionic activity coefficient and osmotic coefficient data at 25 ^{o}C. Table 18 shows the single ion and association parameters for ionic systems validated in the preliminary studies.

Table 18. Ion parameters for two electrolyte systems used for validation of the MATLAB code.

System	Ion Size (NPMSA)	Association Energy	Association Volume
	σ (Å)	ε^{AB}/k (K)	κ^{AB}
NaCl/Water	3.033	3900	0.03
NaBr/Water	2.958	3300	0.03

Results and Discussion

PC-SAFT EoS for Non-Electrolyte System

SAFT theory has been used successfully for a wide range of applications for associating molecules, polar fluids, polymers and hydrogen bonding molecules such as water. The association term derived from fundamental theory by Chapman et al[25] has also been included in other prevalent models such as cubic plus association (CPA) EoS.[45] We demonstrate the ability of PC-SAFT EoS to predict the water content in the hydrocarbon-acid gas system.

Results for single acid gas-hydrocarbon systems are compared to experimental data, other empirical models and charts widely used by industry. Table 19 and Table 20 show predicted water content in hydrogen sulfide-methane system and carbon dioxide-methane system at different mixture compositions at a temperature of 71 ^{o}C and different pressures. As shown in

Table 21, the absolute average deviation (AAD %) in the prediction of water content in a mixed acid gas-hydrocarbon system prediction compared to experimental measurements by Ng et al [62] at two different temperatures and pressures is less than 7 percent. These results are indicative of the efficacy of a molecular level theory, as opposed to an empirical method, in describing the phase behavior of mixtures of water, hydrocarbons, and acid gases.

Table 19. Water content in the binary system methane-hydrogen sulfide.

T (^oC)	P (psia)	H_2S conc. (mol. %)	Water Content (lbm/ MMSCF)					
			Exp.	McKetta	AQUA	Wichert	B-M	PC-SAFT
71.1	1395	16	226	220	235	231	260	209
71.1	1010	17	292	280	294	294	322	271
71.1	611	19	442	410	435	418	467	421
71.1	358	21	712	700	692	707	723	693
71.1	1392	27.5	247	220	255	264	297	220
71.1	925	29	328	300	329	330	375	286

Table 20. Water content in the binary system methane-carbon dioxide.

T (^oC)	P (psia)	CO_2 conc. (mol. %)	Water Content (lbm/ MMSCF)					
			Exp	Maddox	Robinson	AQUA	B-M	PC-SAFT
37.8	2000	11	40.6	42	39.2	42	39.4	39.2
71.1	1000	11	286	277	287	284	287	275.1
37.8	2000	20	40.6	43	44.1	46	40.7	39.7
71.1	1000	20	282	278	287	293	295	275.9

Table 21. Water content in sour natural gas mixtures ([b] Composition of this mixture is 90% methane + 6% ethane + 2.5% propane + 0.6% i-butane + 0.9% n-butane. [c] This mixture consists of methane and propane with a molar ratio equal to 95:5.).

T (°C)	*p* (psia)	Gas phase comp. (mol. %)			PC-SAFT AD %
		CH_4	CO_2	H_2S	
49.0	200.01	0.75[b]	0.0625	0.1875	3.58
49.0	200.01	0.75[b]	0.1875	0.0625	10.97
49.0	1499.55	0.75[b]	0.1875	0.0625	10.31
49.0	1499.55	0.75[b]	0.0625	0.1875	5.98
93.5	200.01	0.75[c]	0.1875	0.0625	1.04
93.5	200.01	0.75[c]	0.0625	0.1875	0.40
93.5	1499.55	0.75[c]	0.1875	0.0625	13.77
93.5	1499.55	0.75[c]	0.0625	0.1875	7.48
93.5	1499.55	0.75[b]	0.1875	0.0625	3.81
AAD %					6.37

Validation of Code and Model Parameters

A flash calculation program based on the PC-SAFT + NPMSA EoS model was coded on a MATLAB platform and the phase compositions were calculated by iteratively solving equations for chemical potential, pressure, and mole fractions using Trust Region nonlinear methods.[63] The code was validated for pure component data for water. Figure 43 shows the coexisting density of water in vapor-liquid region and the vapor pressure over the entire temperature range of vapor-liquid equilibrium calculated from the PC-SAFT + NPMSA EoS and compared with the VDI steam table data.[64] The results from our calculations agree with the experimental data and also correspond to the results by Herzog et al.[53] The code was further validated for NaBr and NaCl electrolyte systems over their solubility range, and the results for density that correspond to experimental data [65] as well as to the model predictions by Herzog et al are shown in Figure 44. It can be concluded from our results as well as from Herzog et al that the univalent electrolyte system behavior can be described by a PC-SAFT + NPMSA to reasonable accuracy over the solubility range and temperature range of 0 - 100 °C. The absolute average deviation for liquid densities is 0.7 percent and for the vapor pressures is 0.33 percent.

Extension to NaCl-H_2O-CO_2 system

The PC-SAFT + NPMSA EoS was then extended to NaCl-H_2O-CO_2 system to evaluate solubility of carbon dioxide in brine (0 - 6 M) at temperatures up to 120 ^oC. It was observed that the PC-SAFT + NPMSA EoS as suggested by Herzog et al grossly under predicted the solubility of CO_2 especially at higher ionic strength. It was observed that the current model overestimates the ion-water association. It should be noted that in the model proposed by Herzog et al, the cation–water association term was taken into account for hydration effects in addition to the ion-dipole interaction in the NPMSA. While this modification works well for ionic activity at lower concentration and temperature, the solubility of nonpolar molecules is under predicted.

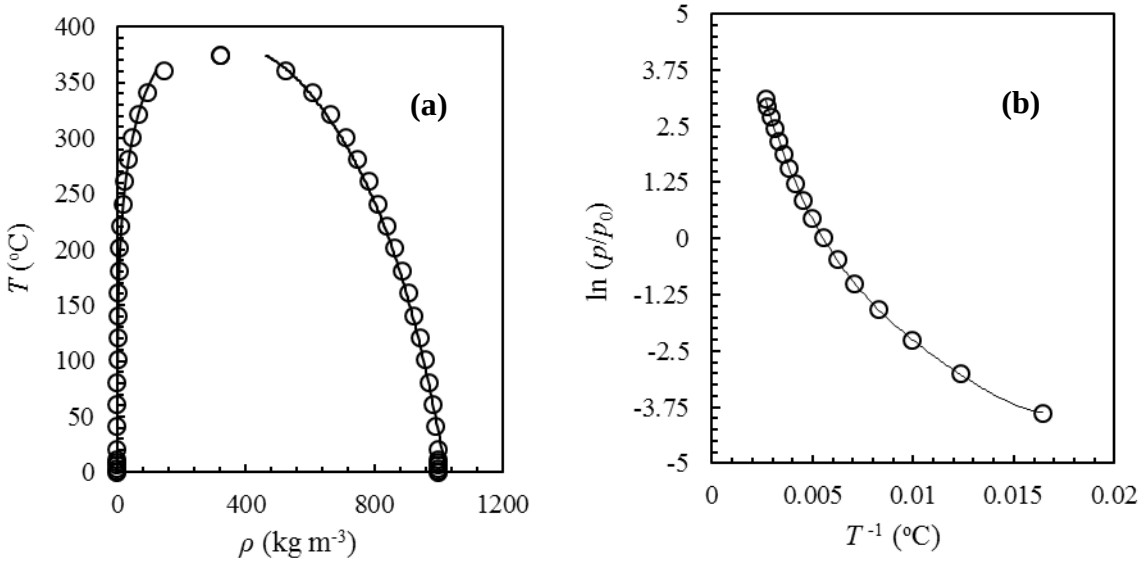

Figure 43. (a)Coexisting densities of water for the complete vapor–liquid region. (b)Vapor pressure of water for the complete vapor–liquid region. PC-SAFT + NPMSA EoS represented by line and the data from VDI steam tables represented by circles.

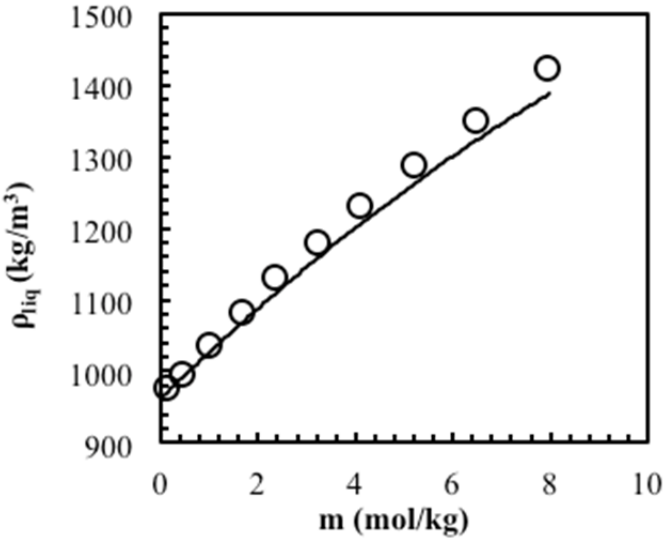

Figure 44. Liquid densities ρ for the system NaBr/H2O at T = 100 °C for the full solubility range. PC-SAFT + NPMSA EoS (line) is compared with data from Wu et al [65] (circles).

It was observed that once the explicit association sites on the cation were removed and the water-ion interactions were treated solely within the NPMSA framework, better predictions for the solubility of CO_2 in brine were obtained. Figure 45 shows that the solubility predictions from the modified PC-SAFT + NPMSA EoS for CO_2 in aqueous NaCl solutions as a function of pressure at different salt concentrations and temperatures agree well with the experimental values. The dipole moment parameter for water $\mu_{D,solv}$ (used in calculating the ion-dipole and dipole-dipole interactions in the NPMSA) was used as the concentration dependent fitting parameter along with the temperature dependent cross interaction parameter k_{ij} term (used in the Lorentz-Berthelot mixing rules for dispersion energy).

The linear dependence of the dipole moment parameter for water on the concentration of NaCl is shown in Figure 46. This is significant in view that the effective dipole moment of the solvent phase is dependent on the induced electric effects due to ionic species. Our observations agree with the simulation results from Gray et al.[66] They showed using renormalized perturbation theory calculations that the effective dipole moment of an electrolyte can be correlated as a function of density. At higher concentrations, the electric field force exerted by ions on water is significant, and induced dipoles thus cannot be neglected. This is one of the significant findings of our investigation. The concentration effects on the polar interactions in the solvent have not been studied in previous SAFT models incorporating MSA models.

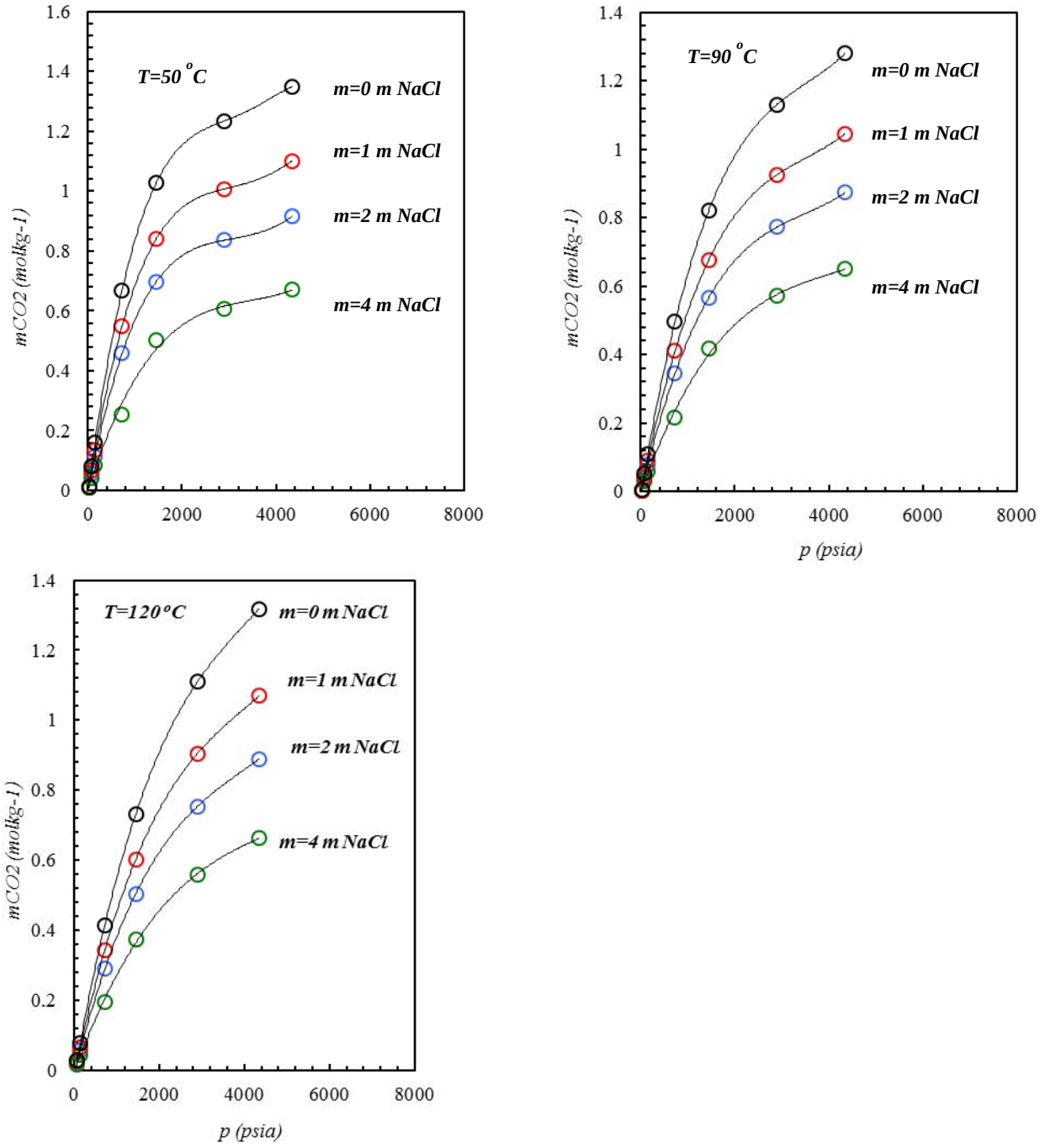

Figure 45. Solubility of CO_2 in sodium chloride solution at different temperatures and pressures for increasing salt concentration as predicted by modified PC-SAFT + NPMSA EoS (line) compared with experimental data[67] (open circles).

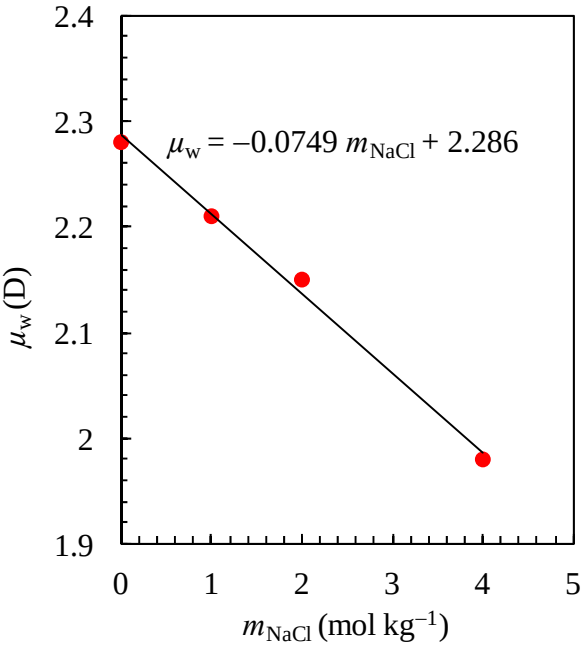

Figure 46. Effect of concentration on the dipole moment parameter for water used for calculating solubility of CO_2 in NaCl solution.

Recommendations for Phase II

The results from PC-SAFT + NPMSA EoS for solubility of acid gas in brine underscore the complexity of the problem and indicate the need for modification of existing molecular models. A more accurate thermodynamic model needs to better describe the polar contributions and the effect of ionic strength thereof, in addition to accounting the hydration effects. In Phase II of the project perturbation theory by Henderson, Blum, and Tani[68] will be used to model induced dipole-dipole and induced dipole-ion interactions. We believe that this approach will allow capturing the change in the effective dipole moment as a function of the salt concentration. This modification will necessitate re-parameterization of pure component parameters for water and ionic species. The semi-restricted MSA model uses a single ion parameter for an ion pair system. In the view of modeling mixed electrolytes, implementation of asymmetric ion parameters, i.e., non-restricted, a non-primitive MSA model along with PC-SAFT appears to be more appropriate and will be pursued in Phase II.

Simultaneous development of an alternative theory to account for the ion hydration and association will be pursued in Phase II of the project. Marshall and Chapman [69] have developed a new equation of state, in the form of a perturbation theory, within the framework of Wertheim's theory, allowing for multiple bonding over a patch.[70] We propose to extend the theory specifically to account for ion solvation by treating ions as a single large association site. Geometric integrals will be solved using Monte Carlo integration to account for ion-water association. The solvation of ions in this formalism will implicitly incorporate steric effects due to size of ion. Similarly, Monte Carlo integration of contact ion pairs with associated water can also be evaluated. Thus, specific ion effects and the size effects will be accounted. We anticipate proving that one can accurately predict the fraction of associated and solvated ion pairs through this method.

In a broader perspective, the aim of this project is to develop a comprehensive molecular level model to predict scaling and corrosion at HPHT. This necessitates the model to be able to accurately predict the activity coefficients of ionic species at HPHT in the presence polar and nonpolar molecules. The activity coefficient, which is also an indication of deviation from ideality, depends on ion-ion, solvent-ion, and solvent-solvent interactions that in turn are functions of temperature and also have contributions due to pressure. Ion speciation and specific ion parameters are important factors in the determination of the activity coefficients. Our efforts in Phase II will be directed towards concatenating information obtained from molecular theory such as activity coefficients with Gibbs free energy based classical theories such as the Unified model [71] to determine solubility indices. The solubility indices are used as engineering parameters in the field to determine the extent of scaling at the given temperature, pressure, and ionic strength. While the knowledge of thermodynamic equilibrium properties are essential to determine the corrosion and scaling conditions, the process of corrosion is dictated to a large extent by kinetic factors. Molecular simulations and kinetic models will be used as complementary tools to model the kinetic aspects of corrosion at xHPHT.

Section II – Molecular Dynamics Simulations

Introduction

Advances made in the field of computer technology and computational methods over the last few decades have enabled researchers to study complex systems at realistic conditions using techniques such as Molecular Dynamics (MD) and Monte Carlo (MC) simulations.[72,73] These simulations yield macroscopic thermodynamic properties obtained from statistical ensemble averages. In the simplest essence, MD simulations are numerical integration of Newton's equations of motion for a system of atoms defined by parameters that determine the forces (electrostatic and dispersion) acting between them. MD simulations can be used effectively to obtain a realistic picture of interactions at the atomistic length scale.

Behavior of ionic species at HPHT especially in supercritical water has been studied using molecular simulations for over two decades. Gao et al [74] showed using potential of mean force (PMF) calculations that interactions between ion pairs become successively attractive with increase in temperature with solvent-separated ion pairs becoming less probable. Chialvo et al [75] studied ion pairing at temperatures in the vicinity of the critical temperature of water using constrained MD simulations. In addition to providing a statistical mechanical interpretation of association constants, simulation results were compared to different ion association models and conductance measurement results at high temperature. Rey and Guardia [76] showed that dynamic aspects of ion pair association calculated by constrained MD simulations are in reasonable agreement with the theoretical prediction. Rasaiah et al [77] used MD simulations to study the structure and dynamics of solvent interactions with ions and neutral species in dilute aqueous solutions at supercritical temperatures. The effect of the size of univalent ions in the solution on the transport properties such as viscosity that are correlated with the structural properties of water in aqueous ionic solution was investigated. Wood et al [78] have shown that hydration free energies for ionic species at supercritical conditions can accurately be predicted using ab initio free energy perturbations in good agreement with the semi-empirical extrapolations from low temperature experimental results.

As proposed, we have employed MD simulations with the objective of understanding the hydration of ionic species at xHPHT conditions and aiding the molecular modeling and equation of state (EoS) development. In Phase I we validated well-known potential models for sodium and chloride ions along with water model by evaluating the partial molar properties at HPHT and comparing with experimental results and theoretical models. Pair-wise correlation functions were validated with those reported in the literature.[79] Formation of ion clusters in steam phase and solvent coordination numbers at HPHT conditions were also studied. Our simulations showed that partial molar volumes at infinite dilution obtained from simple MD simulations with Particle Mesh Ewald [80] (PME) summation for electrostatics yielded values in reasonable agreement with experimental results. A more rigorous integral method such as modified Kirkwood-Buff integral method [81] could also be implemented and will be pursued in Phase II. These potential models will be used in Phase II to investigate the salting out effects, interfacial properties, and solubility of gaseous species in mixed electrolytes at HPHT as a complementary tool to EoS development.

Simulation Details

An all-atom description for all molecular species was employed in the current study. Optimized Potentials for Liquid Simulations, All Atom (OPLS-AA) empirical force field parameters [82] were used to describe the sodium and chloride ions. These parameters were optimized to accurately reproduce the experimental solvation free energy and water coordination number for alkali metal ion and halide species. Water molecules were modeled using a TIP4P/2005 potential model.[83] The particular choice of water potential model is due to its ability to fairly describe the properties of water at pressures as high as 5.8X10^5 psia and temperatures up to 300 ^{o}C. The initial configurations were generated using PACKMOL[84] program by solvating a single ion with 5000 water molecules in a cubic box. This roughly corresponds to a molality of 0.01 as an approximate towards infinite dilution where partial molar properties are determined. Simulations were also performed on a system without ions. The partial molar volumes (PMV) of ionic species can be estimated simply from difference in the volume of simulation box with and without the solute species as follows:

$$\bar{v}_{NaCl}^{\infty} = V_{Na+}^{sim} + V_{Cl-}^{sim} - 2 \times V_{Water}^{sim} \tag{28}$$

The initial configurations were energy minimized using the steepest descent algorithm using GROMACS [85,86] molecular dynamics program for 10,000 steps. Isobaric-isothermal (NPT) MD simulations were carried out at 1450 psia and temperatures in the range 150-300 ^{o}C. The system was relaxed for 50 ns and data sampled every 0.5 ps following equilibration (2 ns) by integrating Newton's equations of motion over a time step of 2 fs. The electrostatic interactions were evaluated using a Particle Mesh Ewald method [80,87], and both vdW and electrostatic interactions were treated with a cut-off at a distance 10 Å. Long-range dispersion corrections for energy and pressure were included. All the bonds involving hydrogen were constrained using the LINCS [88] algorithm. SETTLE [89] algorithm was used to keep the water molecules rigid. Parrinello-Rahman barostat [90,91] and Nosé-Hoover [92,93] thermostat were respectively implemented to control the temperature and pressure.

Results and Discussion

This report presents the key results from the preliminary simulations performed on sodium chloride system in the view of their implication to the development of EoS for brine systems. The partial molar volume at infinite dilution is an important thermodynamic property indicative of the interaction of solvated species with the solvent molecules and the pressure effects. Table 22 shows the partial molar volume of sodium chloride in water at 1450 psia and temperatures of 150 - 300 ^{o}C obtained from MD Simulations. As can be seen, the results from MD simulations are in excellent agreement with those obtained from experiments and from the Unified model[71] described in the previous section. The deviation at 300 ^{o}C may be attributed to the fact that the values reported for the experimental and the theoretical model are those calculated for infinite dilution. When adjusted for the effect of the concentration (0.01 mol/kg) the results from the Unified Model shows better agreement with the simulation results. It should also be noted that the partial molar volumes were determined in a way that ion associations were not taken into the consideration. The ion-ion interactions are significant at near critical temperatures. Lee and Cummings [94] have suggested that the agreement of simulation results with experiments in the view of the approximation can in part be attributed to cancellation of errors due to inaccuracies in water-ion parameters and in part due to the fact ion-water association may not have a significant effect. However, in mixed electrolytes at HPHT ion pairing has significant effects on the volume changes and ion activities. The ion pairing effects in mixed electrolytes will be investigated in detail in Phase II.

Table 22. Partial Molar Volume (cm^3/mol) of NaCl evaluated with MD simulations compared to the values obtained from experiments at infinite dilution and from the Unified Model.

T (^{o}C)	Experimental [95]	Unified Model [71]	MD Simulations
150	11.2 ± 2	10.2 ± 1	11.8
200	-2 ± 3	-1.5 ± 1	3.9
250	-30 ± 7	-28 ± 3	-24.8
300	-118± 12	-125 ± 10	-77.4

Figure 47 shows radial distribution functions (RDF) between the ion and water oxygen pairs obtained from the simulation of single ions in water at 1450 psia and 300 ^{o}C. The principal maxima for the cation (Na^+) – water oxygen (OW) RDF occurs at 2.5 Å and that for anion (Cl^-) – water oxygen (OW) RDF occurs at 3.2 Å. These values agree well with the values reported in the literature.[77] The RDF for the cation has two distinct peaks corresponding to the hydration shells. While the positions of the peaks in Na^+- are similar to those obtained at infinite dilution at ambient conditions, the shape of the peaks are broader. This indicates a strong clustering of water around the Na^+ ions. The RDF for the Cl^--OW pair does not

show a secondary peak, and the primary peak is relatively broader when compared to the primary peak of the Na^+-OW RDF.

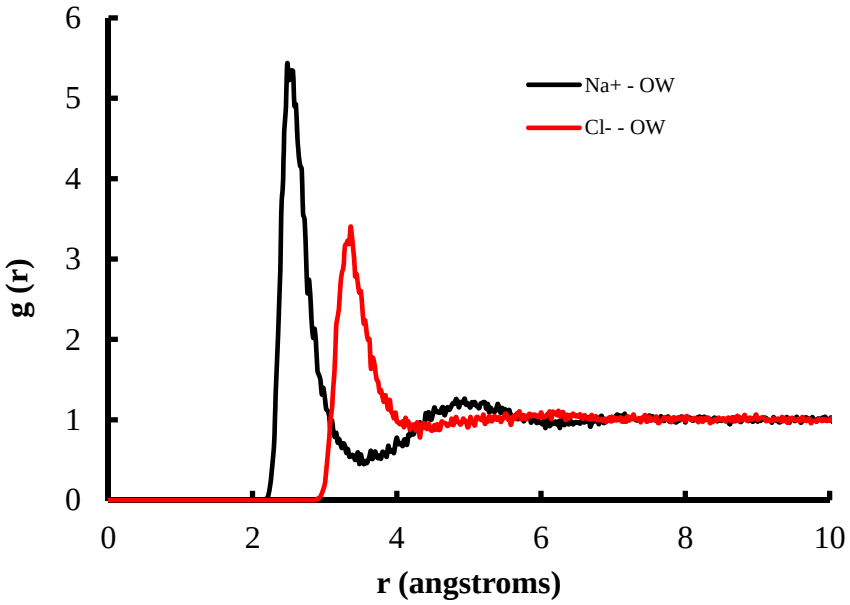

Figure 47. Radial Distribution Function for ion-water oxygen pairs at 1450 psia and 300 °C.

A key element relevant to the EoS development is the water coordination number for the ionic species. The coordination information can be obtained from the RDF [96] as:

$$N_w = \rho_w \int_0^R g_{io}(r) 4\pi r^2 dr \tag{29}$$

where ρ_w is the number density of the water, $g_{io}(r)$ is the ion-oxygen radial distribution function, and R is the position of first minima. The average number of water molecules in the first hydration shell that is associated with the ion was obtained from the numerical integration of the RDF. For the Na^+-OW distribution this number was 5.7, and for Cl^- - OW distribution the water coordination number obtained was 7.7. Within the statistical error these are close to the coordination numbers reported in the literature for ambient conditions.[79] It should be noted that even at the elevated temperature of 300 °C the density of the aqueous phase at 1450 psia was close to 0.7 g/cc. The system pressure was greater than the saturation pressure, and, as evidenced from the RDF, the ion-water associations were very dominant at these conditions. This is important information for the determination of association parameters in the SAFT model.

In oil and natural gas fields, steam, carbon dioxide, fresh water, produced salt water, seawater, and/or alkaline surfactant are used in enhanced recovery. The presence of carbon dioxide and hydrogen sulfide in the produced water and/or natural gas also create conditions conducive to corrosion. The behavior of ionic species at conditions of lower solvent density is significantly different. To further demonstrate the

utility of molecular level investigation of the ion behavior in superheated steam, 10 Na^+ and Cl^- ion pairs were simulated in a box containing 555 water molecules in a constant volume (NVT) ensemble corresponding to 1 mol/kg NaCl solution. The volume of the system was set to the density of steam at 300 ^oC (~0.046 g/cc). Other simulation parameters were the same as described in the methodology section. The initial configuration (Figure 48 (a)) shows 10 NaCl ion pairs in a relatively less dense solvent medium. Over the course of the simulation, these ions come together to form a large ion cluster (Figure Figure 48(b)). Rasaiah et al [77] have also reported the formation of ion super-clusters during simulations at high temperature and low density. The mechanism of ion association in infinitely dilute solution, as suggested by Chialvo et al,[75] involves the formation of

(i) Solvent separated ion pair,

(ii) Solvent shared ion pair, and

(iii) Contact ion pair.

In concentrated solutions at very low solvent density, however, the probability of the solvent separated and the solvent shared configurations are short lived. We observed the formation of the ion super-cluster early in the simulation, which has a long lifetime (> 20 ns). The solvent distribution around the ion cluster can be seen from the ion-water RDF. Figure 49(a) shows the RDF obtained by averaging over several equilibrium configurations (~10,000) for ion-water oxygen pairs.

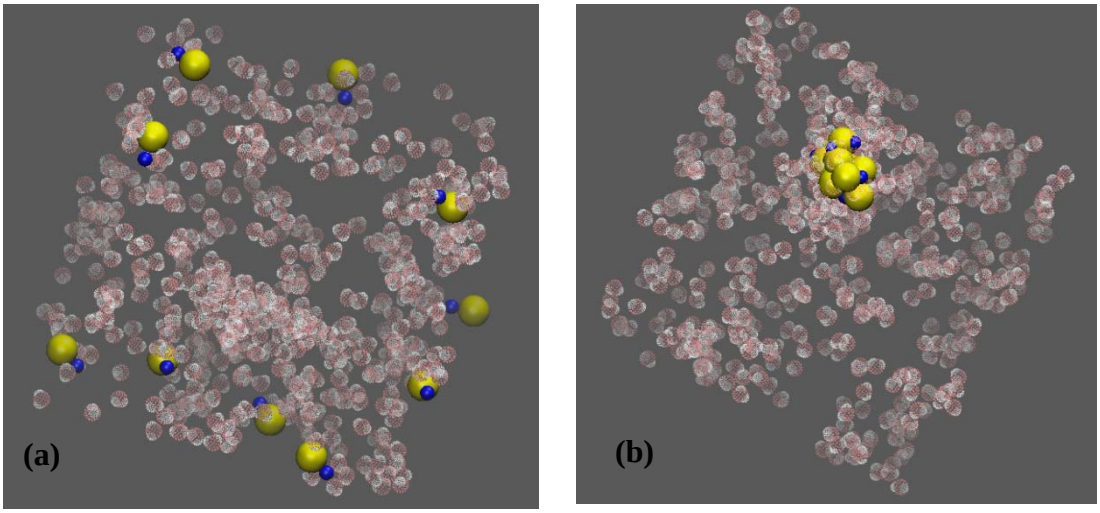

Figure 48. Snapshots from the simulation of ion pairs in saturated steam at 8.56 MPa and 300 ^oC. (a) Initial configuration with separated ion pairs. (b) a mega-cluster consisting of Na^+ and Cl^- ions formed at the end of the equilibration. The blue spheres show the Na^+ ions and the yellow show Cl^- ions. The water molecules are represented by faded red and white species.

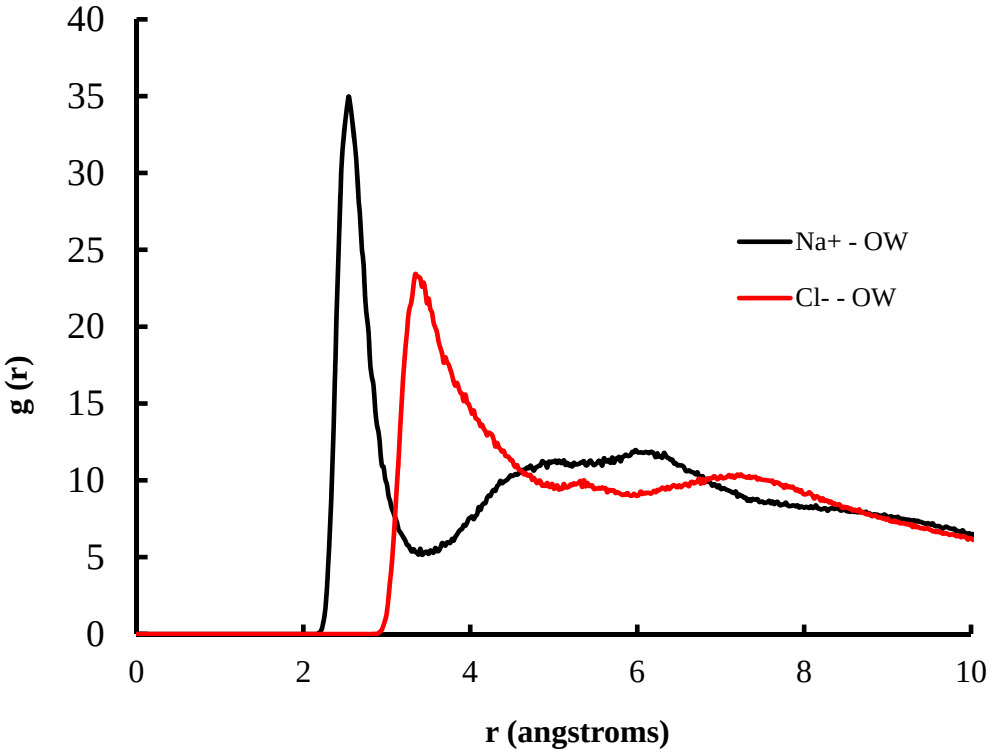

(a)

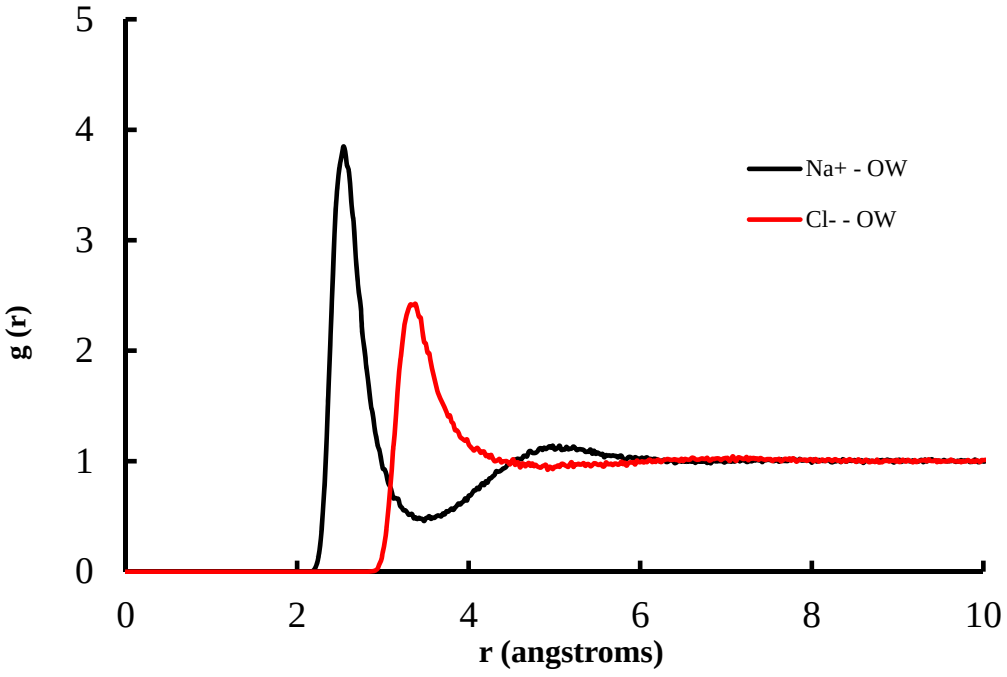

(b)

Figure 49. Radial Distribution Functions for ion-water oxygen pairs in 1 mol/kg NaCl evaluated at (a) 300 oC and density =0.046 g/cc. (b) 300 °C and density = 0.76 g/cc.

The RDF for ion–water oxygen pairs in steam is significantly different from those in the liquid phase (Figure 49(b)). The principal maxima for the Na^+ - OW and Cl^- - OW RDFs correspond to the liquid phase RDFs. However, the secondary peak for Na^+ is highly broadened. This can be attributed to the weakening of hydrogen bonding network in the continuous phase.[46] The water coordination number for Na^+ in the steam phase, obtained from the numerical integration of RDF, was 2.4. This is lower than the coordination number in the water phase (i.e., 4.3) at saturation pressure. This indicates that the cation is fairly hydrated in the liquid phase as opposed to the steam phase. The water coordination number for the anion (Cl^-) in the steam phase is 7.6 and in the liquid phase is 7.0. The higher hydration number of the anion is attributed to the formation of super-cluster and size differences where the cations are obfuscated by the surrounding water molecules. In either case, the anion water RDF does not show a strong secondary shell. These attributes of the water organization around ion clusters have broader impact on the Hoffmeister effects [97] that dictate the solubility of other species such as carbon dioxide, hydrogen sulfide, and methane in the electrolyte solutions.

Recommendations for Phase II

These preliminary results reflect the ability of MD simulations models to predict thermodynamic properties of electrolytes to reasonable accuracy and their ability to offer insights into the solvent organization around ion clusters. The solvent behavior around ion clusters and mechanisms of ion association are difficult to measure directly. MD simulations can be effectively used to understand the role of solvent in ion association under conditions of HPHT, especially in mixed electrolytes, and will significantly aid the molecular theory development. MD simulations will be used to estimate as well as to validate the association parameters for a SAFT-like model such as association number (dependence on temperature, pressure, and concentration), association strength, etc.

MD simulations for Phase II will specifically focus on understanding the solvent behavior in mixed electrolytes containing ions such as Ca^{2+}, Na^+, Ba^{2+}, Cl^-, SO_4^{2-}, CO_3^{2-}, S_2^-, etc. In addition to investigating the water-ion and ion-ion interaction, our efforts will also be focused towards quantifying kinetic factors such as diffusion coefficients. As proposed, simulations will also be used to understand crystal growth behavior for common scales, such as $CaCO_3$ and $FeCO_3$, at HPHT conditions. Furthermore, MC simulations based on the defect-generated dissolution stepwaves model developed by Luttge et al [98] will be used to model corrosion rates at HPHT in Phase II.

We also propose to employ MD simulations to understand the dissolution of nonpolar species, such as CO_2 and H_2S, in saturated brine, as well as in mixed electrolyte systems, at HPHT to investigate the mechanisms of “salting out” effects. Recently, effect of ionic strength on the interfacial tension of CO_2 and brine were studied using MD simulations.[99] We propose to extend the methodology to predict “sour gas” solubility in the presence of different ionic species at HPHT conditions. MD and MC simulations will be used as a complementary tool to validate model predictions in which experimental data is scarce and scattered. The simulations presented in this report and those proposed will be performed on Rice University’s high performance computing cluster, DAVinCI, consisting of 2304 processor cores in 192

Westmere nodes (12 processor cores per node) at 2.83 GHz with 48 GB of RAM per node (4 GB per core).

Section III – Standard State Thermodynamic Properties

The electrolytes at infinite dilutions are introduced as a reference (unperturbed) system for a SAFT model. As such their thermodynamic properties provide the foundation to a SAFT model framework. We have presented a model for prediction of the standard state (infinite dilution) thermodynamic properties of electrolytes to extreme temperatures and pressures (xHPHT). The equilibrium constants for solubility of the following important species for oil and gas industries ($CaCO_3$, $FeCO_3$, FeS, Fe_3O_4, $BaSO_4$, $CaSO_4$, and $SrSO_4$) in aqueous solution are predicted in the present study to extreme temperatures (250 °C) and pressures (24,000 psig). We also predicted and compared the first and second dissociation constants of carbonic acid with the best available corresponding literature data to very high temperatures and pressures. These constants are important for equilibrium calculation in all systems involving aqueous CO_2 at high temperatures and pressures. The equilibrium constants predicted from the present model have been compared with other available models in the literature when possible (SUPCRT 92, SOLMINEQ 88); the values for K_1 and K_2 of carbonic acid were also compared with the model of Li and Duan (2007)). Standard state partial molar volumes of electrolytes to xHPHT are also predicted; the partial molar volume is related to change of equilibrium constant with pressure.

Introduction

The thermodynamic properties of electrolyte solutions at high temperatures and pressures are of significant economic importance in the oil and gas production from natural reservoirs. Corrosion and scale problems cost the industry billions of dollars each year.[10] Finding methods to solve these problems is difficult because details of the chemistry involved in the corrosion processes are not fully understood. Effective prediction of the corrosion and scaling tendency requires a reliable thermodynamic model. The concentrations and thermodynamic properties of the aqueous electrolytes change with temperature, pressure, and phase of the solvent. A necessary step toward obtaining better corrosion and scale control is improved understanding of the chemical behavior of the substances present in the required range of pressures and temperatures, up to 24,000 psig and 250 °C. An important part of this understanding involves knowledge of chemical speciation and thermodynamic data for high temperature chemical reactions.[100]

The most useful thermodynamic information is often the standard state partial molar Gibbs free energy of aqueous ions (the chemical potentials), $G_2^\circ \equiv \mu_2^\circ$, as a function of temperature and pressure, since it is directly related to the equilibrium constant

$$\Delta_{\text{rxn}} G^\circ(T,p) = -RT \ln K(T,p) \tag{30}$$

where $\Delta_{\text{rxn}} G^\circ$ is the change in standard state Gibbs free energy for a specified chemical reaction, *R* is the ideal gas constant, and *K* is the equilibrium constant for the chemical reaction at temperature *T* and pressure *p*. The standard state adopted for the thermal properties of aqueous ions and electrolytes is infinite dilution and for free energies is unit activity of the aqueous species in a hypothetically ideal one

molal (1 mol kg^{-1}) solution referenced to infinite dilution at any temperature and pressure. The liquid standard state for H_2O is the unit activity of pure H_2O at any temperature and pressure. Normally the standard state is limited to 14.69 psig pressure, but for use above 100 ^oC in water the more general definition is more appropriate.

The need for high temperature thermodynamic data becomes apparent when one recognizes that the chemistry of aqueous electrolyte solutions at high temperature differs considerably from that at room temperature, 25 ^oC.[101,101] For example, at 25 ^oC many ion association reactions do not occur to a measurable extent, and many ionic compounds can be considered to be strong electrolytes. But as temperature increases and the dielectric constant of water decreases, ion association becomes more significant.[102] The standard state properties of ions in aqueous solutions change rapidly and in a complex way with temperature. Therefore, it is difficult to estimate their values at high temperature from those at room temperature by simple extrapolation procedures.

Previously there have been two approaches used to obtain high temperature thermodynamic information: the direct experimental determination and semi empirical or theoretical predictions. An excellent detail review of experimental measurements at high temperature and pressure can be found in Chen et al (1994).[100] The following is a short summary of the experimental methods for obtaining standard state properties of aqueous electrolytes at high temperature and pressure. The standard state properties of aqueous electrolytes are experimentally accessible from volumetric, calorimetric, or e.m.f., studies. To be useful, such studies in aqueous solutions require extrapolation of experimental data to infinite dilutions. Such high dilutions are difficult and subject to experimental uncertainties and also to the reliability of extrapolation procedures. This is particularly important in cases in which the low concentration is above the region of validity of limiting laws, such as the Debye-Huckel expression or when ionic association is important. High dilutions are required because as the dielectric constant of water decreases with increasing temperature, dissolved electrolytes show non-ideal behavior (even) at low concentrations. At low concentrations where standard state values can be obtained, the properties of ions are additive, which makes the data particularly useful.

Methods of obtaining standard state Gibbs free energy as a function of temperature and pressure using enthalpy and heat capacity measurements from reaction calorimetry and differential flow calorimetry appears to offer promise in fixing the important standard state functions for key electrolytes over wide ranges of temperature. The reaction calorimeter[103] can be used in very dilute solutions (10^{-4} – 10^{-3} mol/kg), making it possible to extrapolate to a more reliable standard state value at infinite dilution. At present, it is difficult to attempt to make measurements at high temperatures and pressures on all of the chemically stable aqueous ions. It is important, however, to characterize certain key ionic species to search for correlations and theoretical methods to reliably estimate the thermodynamic properties for a much larger set.

Many research groups have designed new instruments to study high temperature and pressure aqueous solutions. Among these are the developments of high temperature flow calorimeter and densitometer.[104,105,106,107] However, latter measurements were made in concentrations above 0.05

mol/kg from where extrapolation to a standard state (infinite dilution) condition is exceedingly difficult above 150 °C. The situation can be further complicated due to ion association at higher temperatures.

A number of empirical and theoretical treatments have been developed over the last 50 years to predict the Gibbs free energy at higher temperatures. To date, no one has succeeded in predicting, from first principles, free energies to the desired accuracy of chemical interest over the liquid range of water. However, a number of semi-empirical extrapolation procedures have been useful over a more limited temperature range.[108,109,110,111,112,113] A model for the Gibbs free energy of hydration of electrolytes in aqueous solutions for prediction of the standard state thermodynamic properties of electrolytes to extreme temperatures and pressures was recently reported.[71,114,115] This model, a unified theory of electrolytes, fits Gibbs free energies of solutions to xHPHT and accounts for all known accurate measurements of standard state partial molal entropies and volumes of electrolytes at xHPHT.

Equilibrium Constant Calculation

The unified model for the calculation of the standard state Gibbs free energies of solution at temperature T and pressure p relative to reference temperature T_r is given by: [115]

$$\begin{aligned}\Delta_{\mathrm{sol}}[G^{\circ}(T,p)\text{-}G^{\circ}(T_{\mathrm{r}},p)] &= \Delta_{\mathrm{subl}}[G^{\circ}(T,p)\text{-}F_1(D)G^{\circ}(T_{\mathrm{r}},p)] \\ &+[\Delta_{\mathrm{sol}}G^{\bullet}(T_{\mathrm{r}},p)+C_S T_{\mathrm{r}}][(F_1(D)\text{-}1] \\ &-C_S\Delta T+\nu R\ln[(\mathrm{R}dT/1000)^{T}/(\mathrm{R}d_{\mathrm{r}}T_{\mathrm{r}}/1000)^{F_1(D)T_{\mathrm{r}}}]\end{aligned} \tag{31a}$$

and

$$\Delta_{\mathrm{sol}}G^{\bullet}(T_{\mathrm{r}},p)=\Delta_{\mathrm{sol}}G^{\circ}(T_{\mathrm{r}},p)-C_H \tag{31b}$$

where C_H and C_S, respectively, represent the enthalpy and entropy loss of the solvent molecules in the primary solvation shell, d is the density of the solvent in g/cm^3, d_r is the density of the solvent at the reference temperature 25 °C, and $F_1(D)$ is a function of dielectric constant, D, of the solvent

$$F_1(D)=\frac{D(T_{\mathrm{r}},p)\cdot[D(T,p)-1]}{D(T,p)\cdot[D(T_{\mathrm{r}},p)-1]} \tag{31c}$$

The values for $\Delta_{\mathrm{subl}}G^{\circ}(T,p)$ are calculated from the Gibbs free energies of formation from standard reference tables.[116,117] Accurate dielectric properties of water as a function of temperature and pressure are required for the prediction of hydration properties from this model (equation 31). Many researchers [118,119,120,121] have analyzed the existing dielectric properties of water. In the present study the Archer and Wang (1990)[121] values are adopted for calculations from the proposed model (equation 31) up to 300 °C.

The model constants, C_H and C_S, are solute specific and are fixed from experimental data; they have been shown to be independent of T and p. [71,114] These model constants for most solutes of interest (fixed from experimental data in aqueous solutions) are known and/or can be calculated from the available

low temperature data. [122] The required value for $\Delta_{sol}G^{\circ}(T_r, p)$ in aqueous solutions is calculated from reference tables.[116]

A comparison of predicted equilibrium constants from this study (equations 17, 18) with the available literature data involving some important species ($CaCO_3$, [123] $FeCO_3$, [124,125,126,127] FeS, [127,128] Fe_3O_4, [129,130,131,127] first [127,132,133,134,135,136] and second [127,132, 136,135,137] dissociation of carbonic acid) for oil and gas industry is given in Figure . This comparison indicates good agreement with the experimental data to well within the experimental uncertainties, up to very high temperatures. In Figure the change in standard state partial molar volumes for first and second dissociation of carbonic acid as a function of temperature at p_{sat}, calculated from this study, are compared with the corresponding experimental values[138] and SUPCRT 92.[127] Comparison indicates a good agreement between the values of ΔV° for the first and second dissociation of carbonic acid calculated from this study and the corresponding experimental values reported by Sharygin and Wood.[138] However, the values of ΔV° for the first and second dissociation of carbonic acid calculated from the SUPCRT 92[127] are not in good agreement with the corresponding experimental values.[138]

Thermodynamic Properties of Barite in Aqueous Solution:

The equilibrium constants for aqueous solution of solid barium sulfate (barite)

$$BaSO_4(cr) = Ba^{2+}(aq) + SO_4^{2-}(aq) \quad (32)$$

up to 350 °C and at p_{sat} are calculated from equations 1 and 2, and the results are compared with the available literature data [127,139,140,141,142] in Figure . The model constants, C_H and C_S, are calculated from ionic additivity relationship. The required auxiliary thermodynamic data for $BaSO_4$(cr) are from JANAF tables.[117] At 150 °C the equilibrium constants predicted for barite solubility from this study differ significantly with the corresponding values reported in literature from solubility measurements, and these differences increase with temperature. However, an excellent agreement between the model prediction from this study and the corresponding values from high dilution calorimetric data is observed. The high dilution (10^{-4} mol/kg) thermodynamic properties from calorimetric data for $BaSO_4$(aq) (Table 23) were calculated by ionic additivity from other strong electrolytes:

$$X^{\circ}(BaSO_4, aq) = X^{\circ}(BaCl_2, aq) + X^{\circ}(Na_2SO_4, aq) - 2X^{\circ}(NaCl, aq) \quad (33)$$

where X° represents the standard state partial molar thermodynamic properties of interest. These properties were generated by combining the data on $BaCl_2$(aq),[143] Na_2SO_4(aq),[143] and NaCl(aq).[144] The differences between the values for the equilibrium constant for solution of barite calculated from solubility measurements in literature and the corresponding values obtained from high dilution calorimetric measurements (see above) can be attributed mainly to association between Ba^{2+}(aq) ion and SO_4^{2-}(aq) ion.

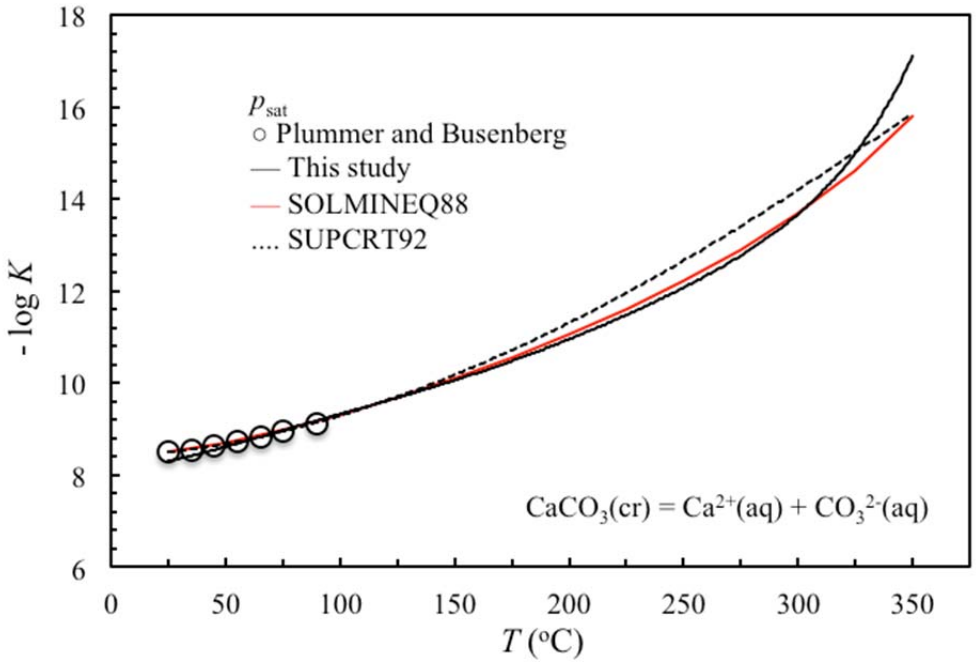
p_{sat}
Plummer and Busenberg
This study
SOLMINEQ88
.... SUPCRT92
$CaCO_3(cr) = Ca^{2+}(aq) + CO_3^{2-}(aq)$
- log K
T (°C)

(a)

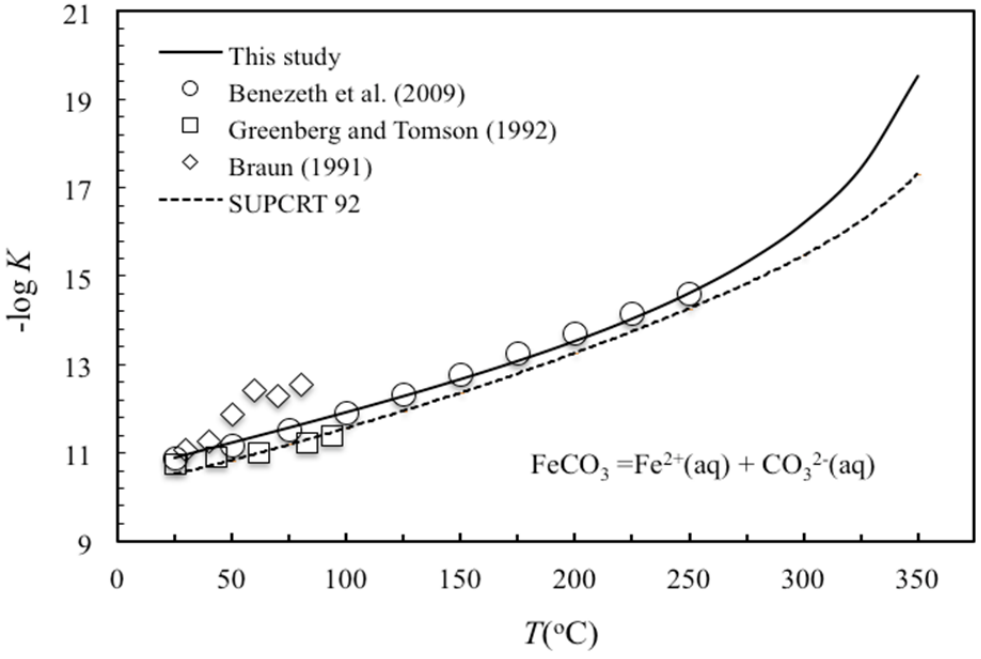
This study
Benezeth et al. (2009)
Greenberg and Tomson (1992)
Braun (1991)
SUPCRT 92
$FeCO_3 = Fe^{2+}(aq) + CO_3^{2-}(aq)$
-log K
T(°C)

(b)

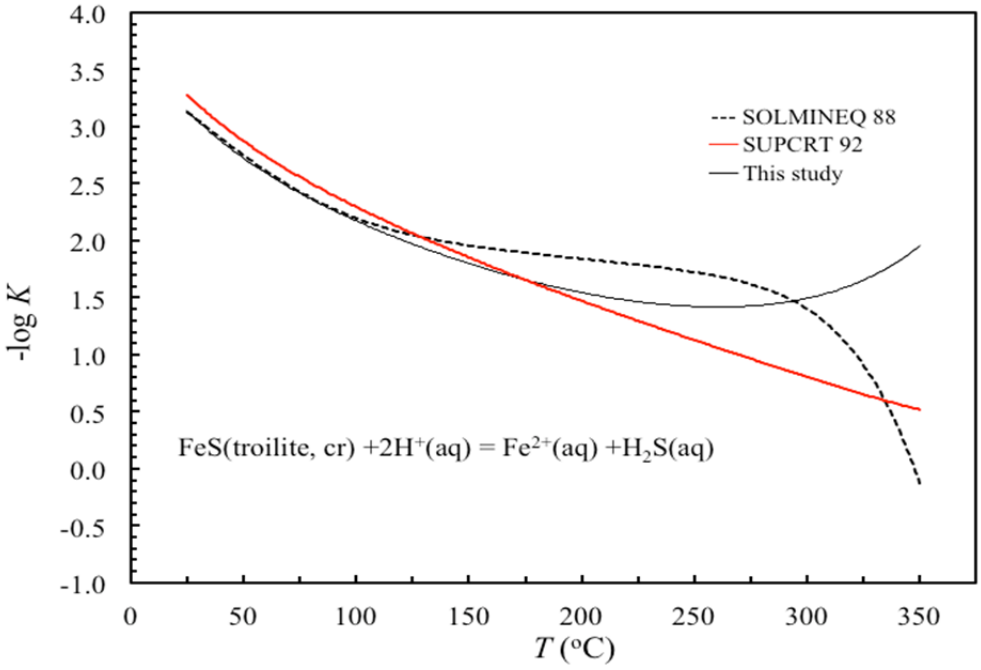
4.0
3.5
3.0
2.5
2.0
1.5
1.0
0.5
0.0
-0.5
-1.0
-log K
0
50
100
150
200
250
300
350
T (°C)
--- SOLMINEQ 88
SUPCRT 92
This study
FeS(troilite, cr) +2H+(aq) = Fe2+(aq) +H2S(aq)

(c)

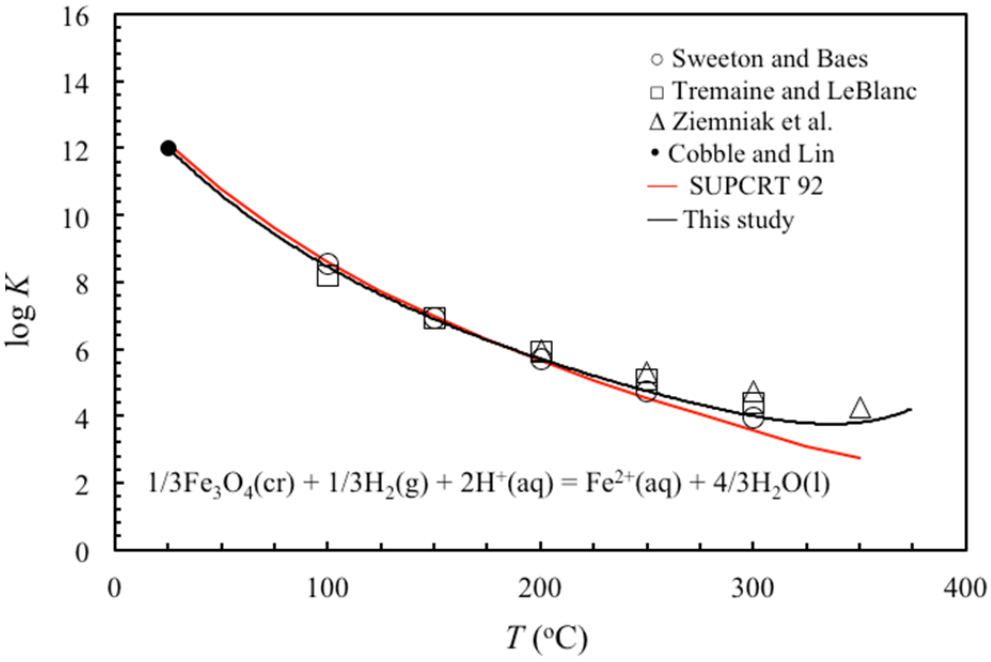
16
14
12
10
8
6
4
2
0
log K
0
100
200
300
400
T (°C)
○ Sweeton and Baes
□ Tremaine and LeBlanc
Δ Ziemniak et al.
• Cobble and Lin
SUPCRT 92
This study
1/3Fe3O4(cr) + 1/3H2(g) + 2H+(aq) = Fe2+(aq) + 4/3H2O(l)

(d)

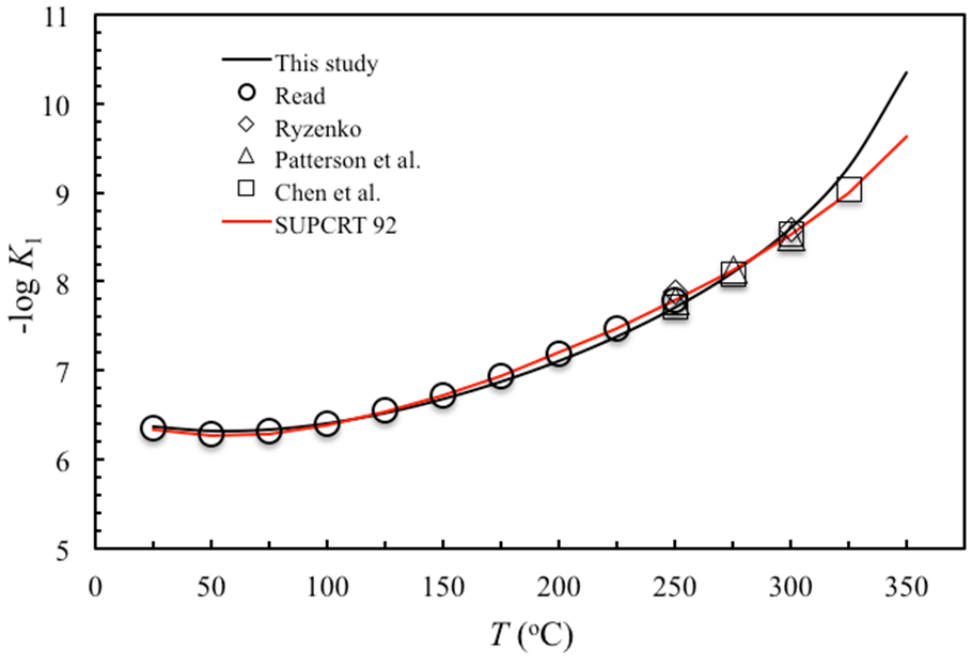

(e)

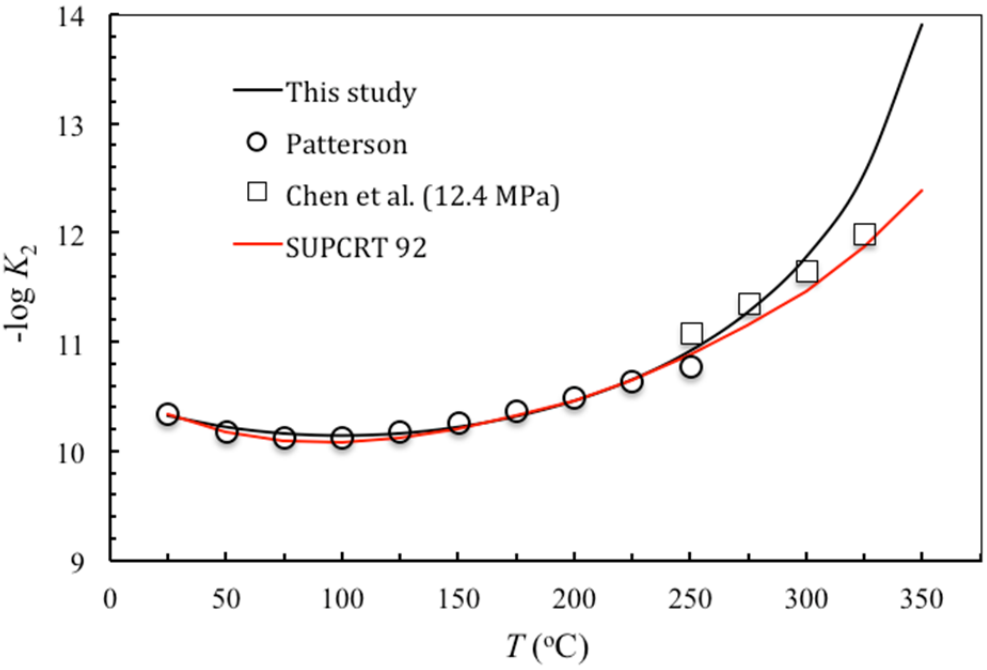

(f)

Figure 50. Comparison of equilibrium constant for the specified reaction predicted from unified theory of electrolytes [71] and the corresponding values from literature as a function of temperature and psat: $CaCO_3$ (a), $FeCO_3$ (b), FeS (c), Fe_3O_4 (d), K1 (e), and K2 (f) for carbonic acid.

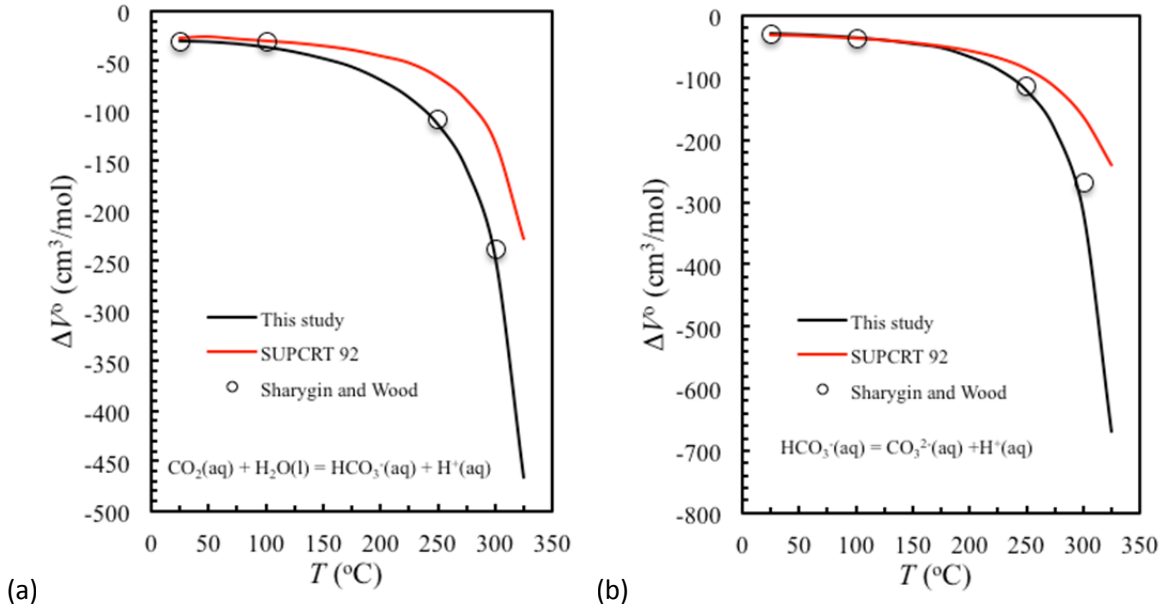

Figure 50. Comparison of change in standard state partial molar volumes for first (a) and second (b) dissociation constants of carbonic acid at p_{sat} from this study and the corresponding values reported in literature.

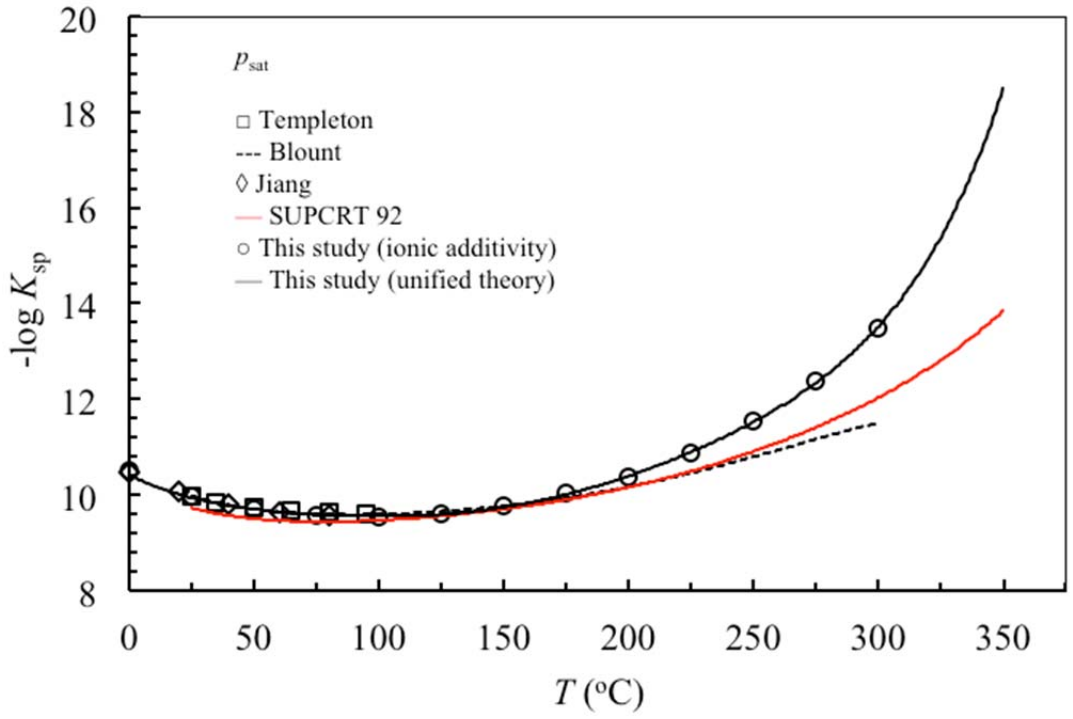

Figure 51. Comparison of log K_{sp} for solution of $BaSO_4$ calculated from unified theory of electrolytes [71] and the corresponding experimental data from literature at p_{sat}.

Table 23. Standard state partial molar enthalpies and Gibbs free energies relative to reference temperature (25 °C), change in Gibbs free energies and solubility constants for solution of barite at p_{sat}.

T (°C)	$H_2^\circ(T)-H_2^\circ(T_r)$	$G_2^\circ(T)-G_2^\circ(T_r)$	$G^\circ(T)-G^\circ(T_r)$ [a]	$\Delta_{sol}G^\circ$ [b]	$-\log K_{SP}$ [d]
25	0.000	0.000	0.000	56.900[c]	9.967
50	-7.166	-0.354	-3.410	59.956	9.690
75	-13.435	-0.192	-7.031	63.739	9.562
100	-19.934	0.418	-10.854	68.172	9.542
125	-28.032	1.503	-14.865	73.268	9.611
150	-39.364	3.175	-19.058	79.133	9.767
175	-55.852	5.642	-23.422	85.964	10.018
200	-79.576	9.191	-27.947	94.038	10.380
225	-114.054	14.205	-32.620	103.725	10.875
250	-152.530	21.164	-37.432	115.496	11.530
275	-224.577	30.676	-42.370	129.946	12.381
300	-339.268	43.555	-47.421	147.876	13.475

[a] Chase et al (1985).[117] [b] $\Delta_{sol}G^\circ = G_2^\circ - G^\circ$. [c] Wagman et al (1982).[116] [d] equation 1.

As a check of the self-consistency of the solubility data the change in Gibbs free energy for barite solubility (reaction 7) at the reference temperature, 25 °C, can be calculated from the enthalpy of the solution, $\Delta_{sol}H^\circ(T,p)$, at each experimental temperature:

$$\Delta_{sol}G^\circ(T_r,p) = T/T_r\Delta_{sol}G^\circ(T,p) + T_r\int_{Tr}^{T}\Delta_{sol}H^\circ(T,p)/T^2dT \quad (34)$$

where $\Delta_{sol}G^\circ(T,p)$ values were calculated from equation 1 and equilibrium constant reported in literature and $\Delta_{sol}H^\circ$ are from calorimetric measurements (see above). The values for $\Delta_{sol}G^\circ(T_r,p)$ for barite solution calculated from each experimental temperature at p_{sat} are plotted in Figure . While such (third law) analysis gives a better value for $\Delta_{sol}G^\circ(T_r,p)$ than can be determined from measurements at that one temperature, it is used here to check the internal consistency of the reported equilibrium constants for barite solubility as a function of temperature. From Figure a good agreement is observed with all reported data up to 150 °C, with exception of data of Malinin[142] at 25 °C. At

temperatures greater than 150 °C the equilibrium constants for solubility of barite reported by Malinin [142] and Blount [140] have large contributions from ion pair formation. Furthermore, Blount [140] did not measure solubility near p_{sat}; his reported equilibrium constant for solubility of barite at p_{sat} is estimated from higher pressure measurements.

In Figure the standard state partial molar volumes, V_2°, for $BaSO_4$(aq) from this study at p_{sat} and 14,500 psi are compared with the corresponding values reported by Blount.[140] Large differences are observed between the two sets of data at p_{sat}, and these differences increase with temperature. These large differences are perhaps partly due to ion association mentioned above and also to the fact that Blount [140] had no measurements near p_{sat}. The V_2° at p_{sat} for $BaSO_4$(aq) reported by Blount [140] are qualitatively more like a 1-1 electrolyte (see e.g., V_2° for NaCl(aq)). A better agreement between the predicted values from present study and the corresponding values for V_2° reported by Blount [140] for $BaSO_4$(aq) at 14,500 psi is observed up to 250 °C , Blount highest temperature (Blount [140] also had a single solubility measurement at 279 °C and 14,500 psia).

The equilibrium constants for solution of barite at 7,250 psia and 14,500 psia from this study are also compared with the corresponding values calculated by Blount [140] from his solubility measurements (Figure). The comparison indicates a better agreement at higher pressures and all temperatures for equilibrium constants for solution of barite predicted from this study and the correspond ones from Blount.[140] This is due to the fact that ion association decreases with increasing pressures and that most measurements of Blount [140] were near 7,250 psia and 14,500 psia.

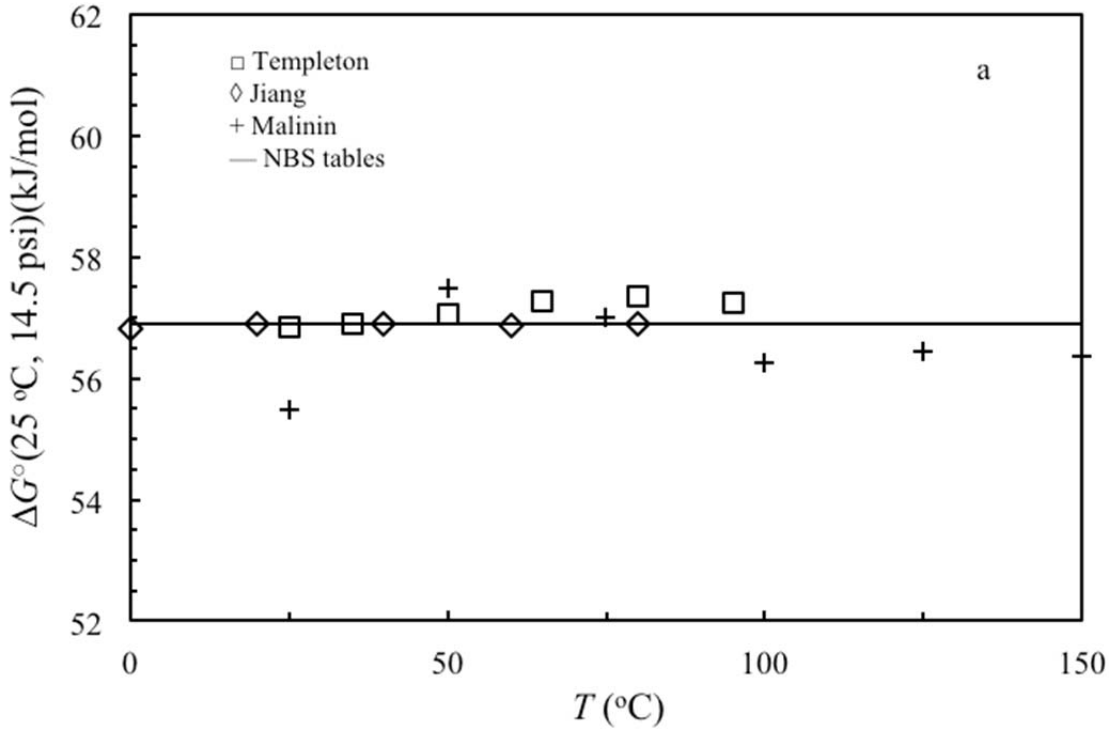

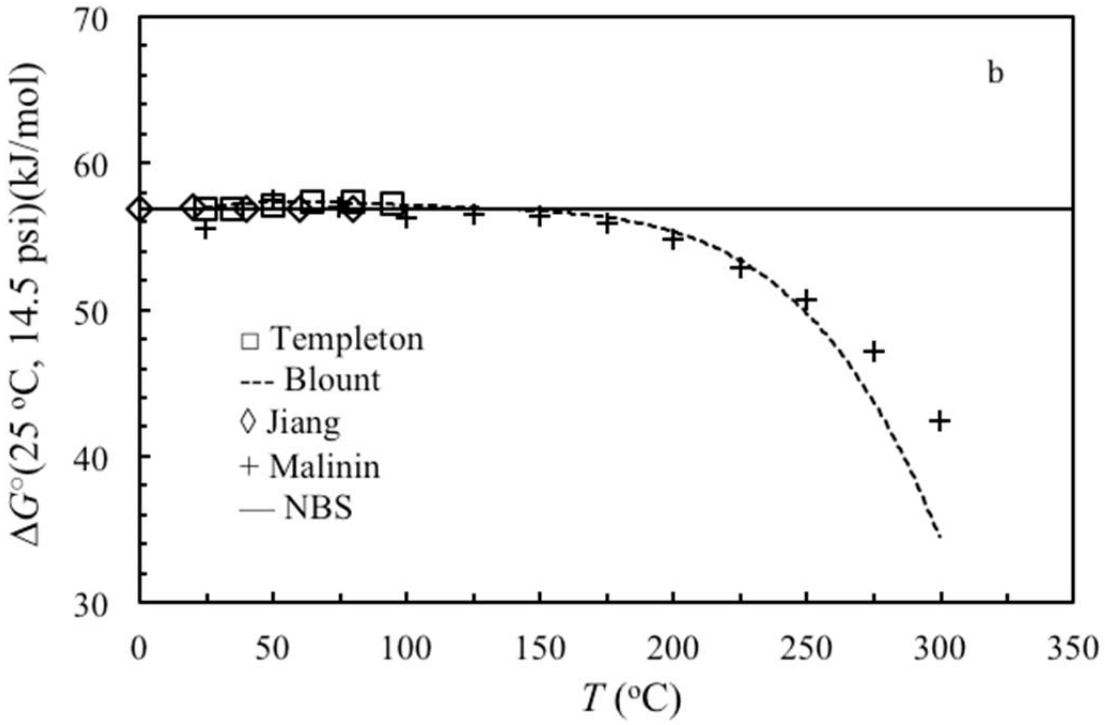

Figure 52. A third law analysis [16] of standard state Gibbs free energy for solution of barium sulfate at 25 °C and 14.5 psia calculated from each experimental data at higher temperatures (eq 34).

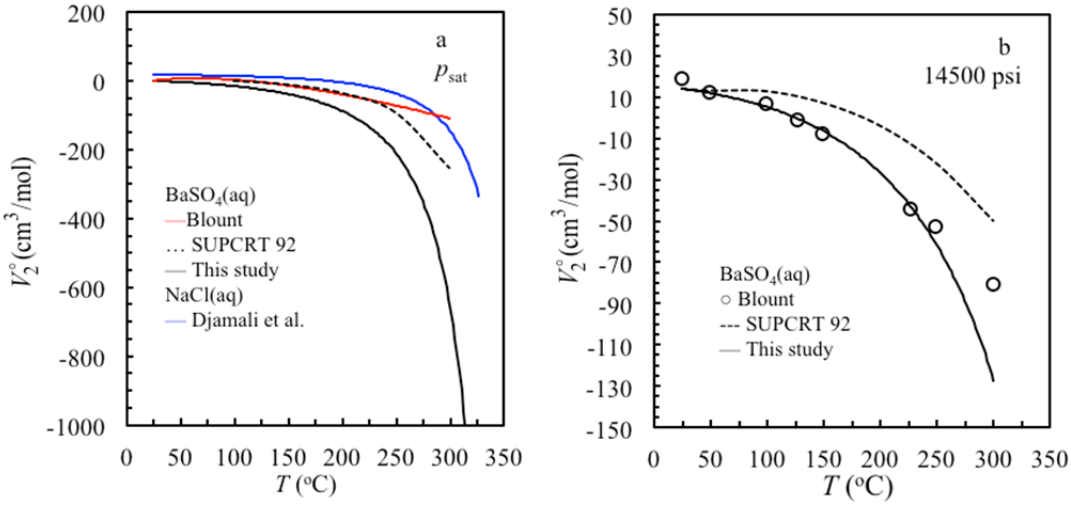

Figure 53. Comparison of standard state partial molar volumes for $BaSO_4$(aq) calculated from this study (unified theory [71]) and the corresponding values reported by Blount [140] at p_{sat} (a) and 14,500 psia (b).

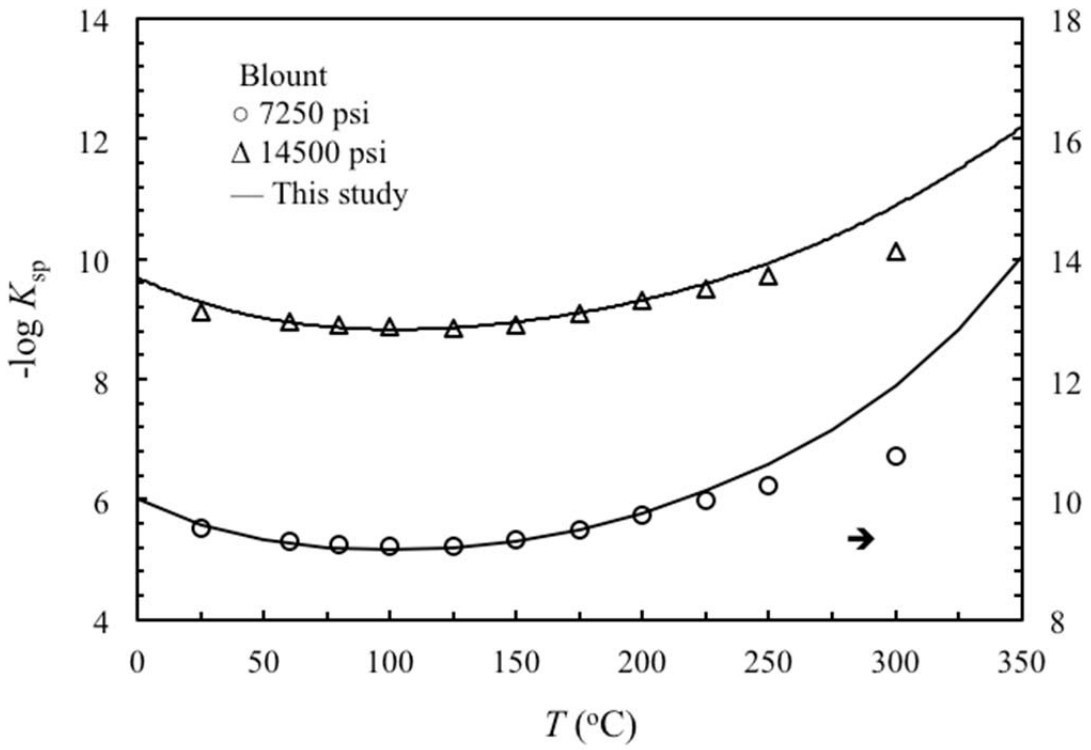

Figure 54. Comparison of log K_{sp} for $BaSO_4$ calculated from this study and the corresponding experimental data from Blount [140] at 7,250 psia and 14,500 psia.

Recommendations for Phase II

The electrolytes at infinite dilutions provide a reference (unperturbed) system for a SAFT model. As such their thermodynamic properties provide the foundation to a SAFT model framework. We have presented a model for accurate prediction of the standard state thermodynamic properties of electrolytes to xHPHT. These standard state thermodynamic properties, together with accurate solubility measurements conducted at BCS, provide an essential quantitative foundation for the development of better parameters for a SAFT model with applications to scale and corrosion at xHPHT in aqueous solutions. Experimental data for solubility of minerals in mixed electrolyte systems are limited at xHPHT. In Phase II solubility of many systems of interest to the oil and gas industry, such as $BaSO_4$, $FeCO_3$, FeS, and Fe_3O_4 scales with various brine compositions will be studied experimentally at BCS. This information is needed for a quantitative understanding of contribution of the ion-ion interactions to the thermodynamic properties for the process of scale and corrosion at xHPHT. The intrinsic equilibrium constants for the above mentioned systems as a function of temperature and pressure were predicted from the Unified model [71] to xHPHT in Phase I of this project. This provides guidance for further experimental measurements and model development. In Phase II the standard state thermodynamic properties for electrolytes to xHPHT calculated from the Unified model will be used to fix the parameters in the SAFT model, which in turn will be compared to the Pitzer model.[14, 145]

RECOMMENDATION TO PERFORM PHASE II

BCS and Rice recommend and request that BCS and Rice proceed and perform Phase II as outlined in the Statement of Work for this project. This recommendation and request is in line with the Tasks set out in the Statement of Work, contract, and Project Management Plan, both in terms of technical content and funding. Throughout this report, additional details on Phase II recommendations are contained in each Task. These recommendations provide more detail, and fit within the existing Tasks outlined in the Phase II Statement of Work. Due to the successful completion of Phase I, the progress being made to address corrosion and scale at xHPHT, and the potential impact of this work, BCS and Rice recommend and request proceeding to Phase II.

REFERENCES

1. NACE, Technical Committee Report, Techniques for Monitoring Corrosion and Related Parameters in Field Applications. *NACE Technique Committee Report* (Item no. 24203), 24203.
2. Choi, Y.-S.; Farelas, F.; Nesic, S.; Magalhães, A.; de Azevedo Andrade, C., Corrosion Behavior of Deep Water Oil Production Tubing Material under Supercritical CO2 Environment: Part I. Effect of Pressure and Temperature. *NACE* **2013**, paper no. 2380.
3. Tanupabrungsun, T.; Brown, B.; Nesic, S., Effect of pH on CO2 Corrosion of Mild Steel at Elevated Temperatures. paper no. 2348.
4. NACE/ASTM, Standard Guide for Conducting Corrosion Coupon Tests in Field Applications. *NACE Standard*, G4.
5. NACE, ASTM Standard Practice for Laboratory Immersion Corrosion Testing of Metals. In *G31-72*, ASTM International: West Conshohocken, PA, 2004; pp G31-72.
6. Dean Jr, S. W., Electrochemical methods of corrosion testing. *Paper* **1976,** (113).
7. ASTM, N., Standard Practice for Preparing, Cleaning, and Evaluating Corrosion Test Specimens. In *Standard G1-90* ASTM International: West Conshohocken, PA, 1999.
8. ASTM, N., Standard Terminology and Acronyms Relating to Corrosion. In *G193-12D*, ASTM International: West Conshohocken, PA, 2012.
9. ASTM, N., Standard Guide for Examination and Evaluation of Pitting Corrosion. In *Standard G46-94*, ASTM International: West Conshohocken, PA, 1999.
10. Brondel, D.; Edwards, R.; Hayman, A.; Hill, D.; Mehta, S.; Semerad, T., Corrosion in the oil industry. *Oilfield review* **1994,** *6* (2), 4-18.
11. Koyuncu, I.; Brant, J.; Luttge, A.; Wiesner, M. R., A comparison of vertical scanning interferometry (VSI) and atomic force microscopy (AFM) for characterizing membrane surface topography. *Journal of Membrane Science* **2006,** *278* (1-2), 410-417.
12. (a) Kan, A.; Tomson, M., Scale prediction for oil and gas production. *Spe Journal* **2012,** *17* (2), 362-378; (b) Dyer, S.; Graham, G., The effect of temperature and pressure on oilfield scale formation. *Journal of Petroleum Science and Engineering* **2002,** *35* (1), 95-107; (c) Fan, C.; Kan, A.; Zhang, P.; Lu, H.; Work, S.; Yu, J.; Tomson, M. In *Scale prediction and inhibition for unconventional oil and gas production*, SPE International Conference on Oilfield Scale, 2010; (d) Fan, C.; Kan, A.; Tomson, M. In *Barite Nucleation and Inhibition at 0-200? C, With and Without Hydrate Inhibitors*, SPE International Symposium on Oilfield Chemistry, 2009.
13. Lewis, G. N.; Randall, M., Thermodynamics; Revised by Pitzer, KS; Brewer, L. *McGraw-Hill, New York* **1961,** *377*, 84.
14. Tomson, M.; Kan, A. T., ScaleSoftPitzer. *Brine Chemistry Consortium* **2012,** *Rice University*.
15. Duan, Z.; Li, D., Coupled phase and aqueous species equilibrium of the H2O–CO2-NaCl–CaCO3 system from 0 to 250° C, 1 to 1000bar with NaCl concentrations up to saturation of halite. *Geochimica et Cosmochimica Acta* **2008,** *72* (20), 5128-5145.
16. Lewis, G.; Randall, M., Thermodynamics, revised by KS Pitzer and L. Brewer. *McGraw-Hill, New York* **1961**, 1983.
17. (a) Pitzer, K. S., Thermodynamics of electrolytes. I. Theoretical basis and general equations. *The Journal of Physical Chemistry* **1973,** *77* (2), 268-277; (b) Peiper, J. C.; Pitzer, K. S., Thermodynamics of aqueous carbonate solutions including mixtures of sodium carbonate, bicarbonate, and chloride. *The Journal of Chemical Thermodynamics* **1982,** *14* (7), 613-638; (c) Shi, W.; Kan, A. T.; Zhang, N.; Tomson, M., Dissolution of Calcite at Up to 250° C and 1450 bar and the Presence of Mixed Salts. *Industrial & Engineering Chemistry Research* **2013,** *52* (6), 2439-2448.

18. Shi, W.; Kan, A. T.; Fan, C.; Tomson, M. B., Solubility of Barite up to 250° C and 1500 bar in up to 6 m NaCl Solution. *Industrial & Engineering Chemistry Research* **2012,** *51* (7), 3119-3128.
19. Kharaka, Y. K.; Gunter, W. D.; Aggarwal, P. K.; Perkins, E. H.; DeBraal, J. D., *SOLMINEQ. 88: A computer program for geochemical modeling of water-rock interactions*. US Geological Survey Menlo Park, California: 1989.
20. Duan, Z.; Sun, R., An improved model calculating CO2 solubility in pure water and aqueous NaCl solutions from 273 to 533 K and from 0 to 2000 bar. *Chemical Geology* **2003,** *193* (3), 257-271.
21. Plummer, L. N.; Busenberg, E., The solubilities of calcite, aragonite and vaterite in CO2-H2O solutions between 0 and 90° C, and an evaluation of the aqueous model for the system CaCO3-CO2-H2O. *Geochimica et Cosmochimica Acta* **1982,** *46* (6), 1011-1040.
22. Helgeson, H. C., Thermodynamics of complex dissociation in aqueous solution at elevated temperatures. *The Journal of Physical Chemistry* **1967,** *71* (10), 3121-3136.
23. Pitzer, K. S.; Peiper, J. C.; Busey, R., *Thermodynamic properties of aqueous sodium chloride solutions*. American Chemical Society and the American Institute of Physics for the National Bureau of Standards: 1984.
24. Chapman, W. G.; Gubbins, K. E.; Jackson, G.; Radosz, M., Saft - Equation-of-State Solution Model for Associating Fluids. *Fluid Phase Equilibr* **1989,** *52*, 31-38.
25. Chapman, W. G.; Gubbins, K. E.; Jackson, G.; Radosz, M., New Reference Equation of State for Associating Liquids. *Industrial & Engineering Chemistry Research* **1990,** *29* (8), 1709-1721.
26. Chapman, W. G.; Jackson, G.; Gubbins, K. E., Phase-Equilibria of Associating Fluids Chain Molecules with Multiple Bonding Sites. *Mol Phys* **1988,** *65* (5), 1057-1079.
27. Wertheim, M. S., Fluids with Highly Directional Attractive Forces .1. Statistical Thermodynamics. *J Stat Phys* **1984,** *35* (1-2), 19-34.
28. Wertheim, M. S., Fluids with Highly Directional Attractive Forces .3. Multiple Attraction Sites. *J Stat Phys* **1986,** *42* (3-4), 459-476.
29. Jog, P. K.; Garcia-Cuellar, A.; Chapman, W. G., Extensions and applications of the SAFT equation of state to solvents, monomers, and polymers. *Fluid Phase Equilibr* **1999,** *158*, 321-326.
30. Jog, P. K.; Sauer, S. G.; Blaesing, J.; Chapman, W. G., Application of dipolar chain theory to the phase behavior of polar fluids and mixtures. *Industrial & Engineering Chemistry Research* **2001,** *40* (21), 4641-4648.
31. Sauer, S. G.; Chapman, W. G., A parametric study of dipolar chain theory with applications to ketone mixtures. *Industrial & Engineering Chemistry Research* **2003,** *42* (22), 5687-5696.
32. Barker, J. A.; Henderson, D., Perturbation theory and equation of state for fluids. II. A successful theory of liquids. *The Journal of Chemical Physics* **1967,** *47*, 4714.
33. Gross, J.; Sadowski, G., Perturbed-chain SAFT: An equation of state based on a perturbation theory for chain molecules. *Industrial & Engineering Chemistry Research* **2001,** *40* (4), 1244-1260.
34. Gross, J.; Sadowski, G., Application of the perturbed-chain SAFT equation of state to associating systems. *Industrial & Engineering Chemistry Research* **2002,** *41* (22), 5510-5515.
35. Debye, V. P.; Hückel, E., The theory of electrolytes. I. Lowering of freezing point and related phenomena. *Physikalische Zeitschrift* **1923,** *24* (185).
36. Breit, G.; Friedman, K. A.; Holt, J. M.; Seamon, R. E., Short- and Long-Range Charge Independence. *Phys Rev* **1968,** *170* (5), 1424-&.
37. Kinoshita, M.; Harada, M., Numerical-Solution of the Hnc Equation for Ionic Systems. *Mol Phys* **1988,** *65* (3), 599-618.
38. Blum, L., Solution of the Ornstein-Zernike Equation for a Mixture of Hard Ions and Yukawa Closure. *J Stat Phys* **1980,** *22* (6), 661-672.
39. Ornstein, L.; Zernike, F., The influence of accidental deviations of density on the equation of state. *Koninklijke Nederlandsche Akademie van Wetenschappen Proceedings* **1914,** *19* (2), 1312-1315.

40. Stell, G.; Lebowitz, J. L., Equilibrium Properties of a System of Charged Particles. *The Journal of Chemical Physics* **1968,** *49* (8), 3706-3717.
41. Rosenfeld, Y.; Blum, L., Statistical-Mechanics of Charged Objects - General-Method and Applications to Simple Systems. *J Chem Phys* **1986,** *85* (3), 1556-1566.
42. Adelman, S.; Deutch, J., Exact solution of the mean spherical model for strong electrolytes in polar solvents. *The Journal of Chemical Physics* **1974,** *60*, 3935.
43. Blum, L.; Vericat, F.; Fawcett, W. R., On the Mean Spherical Approximation for Hard Ions and Dipoles. *J Chem Phys* **1992,** *96* (4), 3039-3044.
44. Blum, L.; Wei, D. Q., Analytical Solution of the Mean Spherical Approximation for an Arbitrary Mixture of Ions in a Dipolar Solvent. *J Chem Phys* **1987,** *87* (1), 555-565.
45. Kontogeorgis, G. M.; Voutsas, E. C.; Yakoumis, I. V.; Tassios, D. P., An equation of state for associating fluids. *Industrial & Engineering Chemistry Research* **1996,** *35* (11), 4310-4318.
46. Mancinelli, R.; Botti, A.; Bruni, F.; Ricci, M. A.; Soper, A. K., Hydration of sodium, potassium, and chloride ions in solution and the concept of structure maker/breaker. *J Phys Chem B* **2007,** *111* (48), 13570-13577.
47. Hribar, B.; Southall, N. T.; Vlachy, V.; Dill, K. A., How ions affect the structure of water. *J Am Chem Soc* **2002,** *124* (41), 12302-12311.
48. Llanorestrepo, M.; Chapman, W. G., Bridge Function and Cavity Correlation-Function for the Soft-Sphere Fluid from Simulation - Implications on Closure Relations. *J Chem Phys* **1994,** *100* (7), 5139-5148.
49. Patel, B. H.; Paricaud, P.; Galindo, A.; Maitland, G. C., Prediction of the salting-out effect of strong electrolytes on water plus alkane solutions. *Industrial & Engineering Chemistry Research* **2003,** *42* (16), 3809-3823.
50. Behzadi, B.; Patel, B. H.; Galindo, A.; Ghotbi, C., Modeling electrolyte solutions with the SAFT-VR equation using Yukawa potentials and the mean-spherical approximation. *Fluid Phase Equilibr* **2005,** *236* (1-2), 241-255.
51. Zhao, H. G.; dos Ramos, M. C.; McCabe, C., Development of an equation of state for electrolyte solutions by combining the statistical associating fluid theory and the mean spherical approximation for the nonprimitive model. *J Chem Phys* **2007,** *126* (24).
52. Cameretti, L. F.; Sadowski, G.; Mollerup, J. M., Modeling of aqueous electrolyte solutions with perturbed-chain statistical associated fluid theory. *Industrial & Engineering Chemistry Research* **2005,** *44* (9), 3355-3362.
53. Herzog, S.; Gross, J.; Arlt, W., Equation of state for aqueous electrolyte systems based on the semirestricted non-primitive mean spherical approximation. *Fluid Phase Equilibr* **2010,** *297* (1), 23-33.
54. Sun, R.; Dubessy, J., Prediction of vapor-liquid equilibrium and PVTx properties of geological fluid system with SAFT-LJ EOS including multi-polar contribution. Part I: Application to H2O-CO2 system. *Geochimica Et Cosmochimica Acta* **2010,** *74* (7), 1982-1998.
55. Sun, R.; Dubessy, J., Prediction of vapor-liquid equilibrium and PVTx properties of geological fluid system with SAFT-LJ EOS including multi-polar contribution. Part II: Application to H2O-NaCl and CO2-H2O-NaCl System. *Geochimica Et Cosmochimica Acta* **2012,** *88*, 130-145.
56. Wu, J. Z.; Prausnitz, J. M., Phase equilibria for systems containing hydrocarbons, water, and salt: An extended Peng-Robinson equation of state. *Industrial & Engineering Chemistry Research* **1998,** *37* (5), 1634-1643.
57. Lin, Y.; Thomsen, K.; de Hemptinne, J. C., Multicomponent equations of state for electrolytes. *Aiche J* **2007,** *53* (4), 989-1005.
58. Pauling, L., *Die Natur der chemischen Bindung*. Verlag Chemie: 1962.
59. Mavroyannis, C.; Stephen, M. J., Dispersion forces. *Mol. Phys.* **1962,** *5*.

60. Lorentz, H. A., Ueber die Anwendung des Satzes vom Virial in der kinetischen Theorie der Gase. *Annalen der Physik* **1881,** *248* (1), 127-136.
61. Berthelot, D., Sur le mélange des gaz. *Comptes Rendus* **1898,** *126*, 1703-1706.
62. Ng, H.-J.; Chen, C.-J.; Schroeder, H., *Water content of natural gas systems containing acid gas*. Gas Processors Association: 2001.
63. Marquardt, D. W., An algorithm for least-squares estimation of nonlinear parameters. *Journal of the Society for Industrial & Applied Mathematics* **1963,** *11* (2), 431-441.
64. Schmidt, E., VDI Steam Tables. *Springer-Verlag, Berlin* **1963**.
65. Hamer, W. J.; Wu, Y. C., Osmotic Coefficients and Mean Activity Coefficients of Uni-univalent Electrolytes in Water at 25° C. *Journal of Physical and Chemical Reference Data* **1972,** *1*, 1047.
66. Gray, C. G.; Joslin, C. G.; Venkatasubramanian, V.; Gubbins, K. E., Induction Effects in Fluid Mixtures of Dipolar Quadrupolar Polarizable Molecules. *Mol Phys* **1985,** *54* (5), 1129-1148.
67. Duan, Z. H.; Sun, R., An improved model calculating CO2 solubility in pure water and aqueous NaCl solutions from 273 to 533 K and from 0 to 2000 bar. *Chemical Geology* **2003,** *193* (3-4), 257-271.
68. Henderson, D.; Blum, L.; Tani, A. In *Equation of state of ionic fluids*, ACS Symp. Ser, ACS Publications: 1986; pp 281-296.
69. Marshall, B. D.; Chapman, W. G., Three new branched chain equations of state based on Wertheim's perturbation theory. *J Chem Phys* **2013,** *138* (17).
70. Marshall, B. D.; Chapman, W. G., A density functional theory for patchy colloids based on Wertheim's association theory: Beyond the single bonding condition. *J Chem Phys* **2013,** *138* (4).
71. Djamali, E.; Cobble, J. W., A Unified Theory of the Thermodynamic Properties of Aqueous Electrolytes to Extreme Temperatures and Pressures. *J Phys Chem B* **2009,** *113* (8), 2398-2403.
72. Allen, M. P.; Tildesley, D. J., *Computer simulation of liquids*. Oxford university press: 1989.
73. Frenkel, D.; Smit, B.; Ratner, M. A., Understanding molecular simulation: from algorithms to applications. *Physics Today* **1997,** *50*, 66.
74. Gao, J. L., Simulation of the Na+Cl- Ion-Pair in Supercritical Water. *J Phys Chem-Us* **1994,** *98* (24), 6049-6053.
75. Chialvo, A. A.; Cummings, P. T.; Cochran, H. D.; Simonson, J. M.; Mesmer, R. E., Na+-Cl- Ion-Pair Association in Supercritical Water. *J Chem Phys* **1995,** *103* (21), 9379-9387.
76. Rey, R.; Guardia, E., Dynamic Aspects of the Na+-Cl- Ion-Pair Association in Water. *J Phys Chem-Us* **1992,** *96* (11), 4712-4718.
77. Koneshan, S.; Rasaiah, J. C., Computer simulation studies of aqueous sodium chloride solutions at 298 K and 683 K. *J Chem Phys* **2000,** *113* (18), 8125-8137.
78. Liu, W. B.; Wood, R. H.; Doren, D. J., Sodium chloride in supercritical water as a function of density: Potentials of mean force and an equation for the dissociation constant from 723 to 1073 K and from 0 to 0.9 g/cm(3). *J Phys Chem B* **2008,** *112* (24), 7289-7297.
79. Koneshan, S.; Rasaiah, J. C.; Lynden-Bell, R. M.; Lee, S. H., Solvent structure, dynamics, and ion mobility in aqueous solutions at 25 degrees C. *J Phys Chem B* **1998,** *102* (21), 4193-4204.
80. Darden, T.; York, D.; Pedersen, L., Particle Mesh Ewald - an N.Log(N) Method for Ewald Sums in Large Systems. *J Chem Phys* **1993,** *98* (12), 10089-10092.
81. Ferrario, M.; Ciccotti, G.; Spohr, E.; Cartailler, T.; Turq, P., Solubility of KF in water by molecular dynamics using the Kirkwood integration method. *J Chem Phys* **2002,** *117* (10), 4947-4953.
82. Jensen, K. P.; Jorgensen, W. L., Halide, ammonium, and alkali metal ion parameters for modeling aqueous solutions. *J Chem Theory Comput* **2006,** *2* (6), 1499-1509.
83. Abascal, J. L. F.; Vega, C., A general purpose model for the condensed phases of water: TIP4P/2005. *J Chem Phys* **2005,** *123* (23).
84. Martinez, L.; Andrade, R.; Birgin, E. G.; Martinez, J. M., PACKMOL: A Package for Building Initial Configurations for Molecular Dynamics Simulations. *J Comput Chem* **2009,** *30* (13), 2157-2164.

85. Hess, B.; Kutzner, C.; van der Spoel, D.; Lindahl, E., GROMACS 4: Algorithms for highly efficient, load-balanced, and scalable molecular simulation. *J Chem Theory Comput* **2008,** *4* (3), 435-447.
86. Pronk, S.; Pall, S.; Schulz, R.; Larsson, P.; Bjelkmar, P.; Apostolov, R.; Shirts, M. R.; Smith, J. C.; Kasson, P. M.; van der Spoel, D.; Hess, B.; Lindahl, E., GROMACS 4.5: a high-throughput and highly parallel open source molecular simulation toolkit. *Bioinformatics* **2013,** *29* (7), 845-854.
87. Essmann, U.; Perera, L.; Berkowitz, M. L.; Darden, T.; Lee, H.; Pedersen, L. G., A Smooth Particle Mesh Ewald Method. *J Chem Phys* **1995,** *103* (19), 8577-8593.
88. Hess, B.; Bekker, H.; Berendsen, H. J. C.; Fraaije, J. G. E. M., LINCS: A linear constraint solver for molecular simulations. *J Comput Chem* **1997,** *18* (12), 1463-1472.
89. Miyamoto, S.; Kollman, P. A., SETTLE: an analytical version of the SHAKE and RATTLE algorithm for rigid water models. *J Comput Chem* **1992,** *13* (8), 952-962.
90. Parrinello, M.; Rahman, A., Polymorphic Transitions in Single-Crystals - a New Molecular-Dynamics Method. *J Appl Phys* **1981,** *52* (12), 7182-7190.
91. Bussi, G.; Donadio, D.; Parrinello, M., Canonical sampling through velocity rescaling. *J Chem Phys* **2007,** *126* (1).
92. Nose, S., A Molecular-Dynamics Method for Simulations in the Canonical Ensemble. *Mol Phys* **1984,** *52* (2), 255-268.
93. Hoover, W. G., Canonical Dynamics - Equilibrium Phase-Space Distributions. *Phys Rev A* **1985,** *31* (3), 1695-1697.
94. Lee, S. H.; Cummings, P. T., Molecular dynamics simulation of limiting conductances for LiCl, NaBr, and CsBr in supercritical water. *J Chem Phys* **2000,** *112* (2), 864-869.
95. Lvov, S. N.; Rakhmilevich, Y. D.; Dibrov, I. A., Thermoelectric Study of Electrolyte Aqueous-Solutions .3. Standard Importance of Partial Molar Entropy and Heat-Capacity of Chlorine Ions at 283-353-K. *Zh Fiz Khim+* **1984,** *58* (9), 2240-2244.
96. Rempe, S. B.; Pratt, L. R., The hydration number of Na(+) in liquid water. *Fluid Phase Equilibr* **2001,** *183*, 121-132.
97. Baldwin, R. L., How Hofmeister ion interactions affect protein stability. *Biophysical Journal* **1996,** *71* (4), 2056-2063.
98. Arvidson, R. S.; Luttge, A., Kinetic Monte Carlo modeling of calcite dissolution kinetics. *Geochimica Et Cosmochimica Acta* **2004,** *68* (11), A125-A125.
99. Li, X. S.; Ross, D. A.; Trusler, J. P. M.; Maitland, G. C.; Boek, E. S., Molecular Dynamics Simulations of CO2 and Brine Interfacial Tension at High Temperatures and Pressures. *J Phys Chem B* **2013,** *117* (18), 5647-5652.
100. Chen, X. M.; Izatt, R. M.; Oscarson, J. L., Thermodynamic Data for Ligand Interaction with Protons and Metal-Ions in Aqueous-Solutions at High-Temperatures. *Chem Rev* **1994,** *94* (2), 467-517.
101. Cobble, J. W., Thermodynamics. *Annu Rev Phys Chem* **1966,** *17*, 15-&.
102. Lindsay, W. T. L., C., High Temperature Pressure Electrochemistry in Aqueous Solution. In *NACE-4*, Houston, TX, 1977.
103. Djamali, E.; Turner, P. J.; Murray, R. C.; Cobble, J. W., A high-temperature high-pressure calorimeter for determining heats of solution up to 623 K. *Rev Sci Instrum* **2010,** *81* (7).
104. Rogers, P. S. Z.; Pitzer, K. S., Volumetric Properties of Aqueous Sodium-Chloride Solutions. *Journal of Physical and Chemical Reference Data* **1982,** *11* (1), 15-81.
105. Zimmerman, G. H.; Gruszkiewicz, M. S.; Wood, R. H., New Apparatus for Conductance Measurements at High-Temperatures - Conductance of Aqueous-Solutions of Licl, Nacl, Nabr, and Csbr at 28 Mpa and Water Densities from 700 to 264 Kg M(-3). *J Phys Chem-Us* **1995,** *99* (29), 11612-11625.
106. Hynek, V.; Obsil, M.; Majer, V.; Quint, J.; Grolier, J. P. E., A vibrating tube flow densitometer for measurements with corrosive solutions at temperatures up to 723 K and pressures up to 40 MPa. *Int J Thermophys* **1997,** *18* (3), 719-732.

107. Hnedkovsky, L.; Hynek, V.; Majer, V.; Wood, R. H., A new version of differential flow heat capacity calorimeter; tests of heat loss corrections and heat capacities of aqueous NaCl from T=300 K to T=623 K. *J Chem Thermodyn* **2002,** *34* (6), 755-782.
108. Helgeson, H. C.; Kirkham, D. H., Theoretical Prediction of Thermodynamic Properties of Aqueous Electrolytes at High-Pressures and Temperatures .3. Equation of State for Aqueous Species at Infinite Dilution. *Am J Sci* **1976,** *276* (2), 97-240.
109. Tremaine, P. R.; Goldman, S., Calculation of Gibbs Free-Energies of Aqueous-Electrolytes to 350-Degrees-C from an Electrostatic Model for Ionic Hydration. *J Phys Chem-Us* **1978,** *82* (21), 2317-2321.
110. Sen, U., Study of Electrolytic Solution Process Using the Scaled-Particle Theory .3. Effects of Thermal Dilution on Standard Thermodynamic Functions. *J Chem Soc Farad T 1* **1981,** *77*, 2883-2899.
111. Anderson, G. M.; Castet, S.; Schott, J.; Mesmer, R. E., The Density Model for Estimation of Thermodynamic Parameters of Reactions at High-Temperatures and Pressures. *Geochimica Et Cosmochimica Acta* **1991,** *55* (7), 1769-1779.
112. Shock, E. L.; Oelkers, E. H.; Johnson, J. W.; Sverjensky, D. A.; Helgeson, H. C., Calculation of the Thermodynamic Properties of Aqueous Species at High-Pressures and Temperatures - Effective Electrostatic Radii, Dissociation-Constants and Standard Partial Molal Properties to 1000-Degrees-C and 5-Kbar. *J Chem Soc Faraday T* **1992,** *88* (6), 803-826.
113. Sedlbauer, J.; O'Connell, J. P.; Wood, R. H., A new equation of state for correlation and prediction of standard molal thermodynamic properties of aqueous species at high temperatures and pressures. *Chemical Geology* **2000,** *163* (1-4), 43-63.
114. Djamali, E.; Cobble, J. W., Thermodynamic Properties of Aqueous Polyatomic Ions at Extreme Temperatures and Pressures. *J Phys Chem B* **2010,** *114* (11), 3887-3893.
115. Djamali, E.; Kan, A. T.; Tomson, M. B., A Priori Prediction of Thermodynamic Properties of Electrolytes in Mixed Aqueous-Organic Solvents to Extreme Temperatures. *J Phys Chem B* **2012,** *116* (30), 9033-9042.
116. Wagman, D. D.; Evans, W. H.; Parker, V. B.; Schumm, R. H.; Halow, I. *The NBS tables of chemical thermodynamic properties. Selected values for inorganic and C1 and C2 organic substances in SI units*; DTIC Document: 1982.
117. Chase Jr, M.; Davies, C.; Downey Jr, J.; Frurip, D.; McDonald, R.; Syveraud, A., JANAF thermodynamic tables. *J. Phys. Chem. Ref. Data* **1985,** *14* (Suppl 1).
118. Helgeson, H. C.; Kirkham, D. H., Theoretical Prediction of Thermodynamic Behavior of Aqueous Electrolytes at High Pressures and Temperatures .1. Summary of Thermodynamic-Electrostatic Properties of Solvent. *Am J Sci* **1974,** *274* (10), 1089-&.
119. Bradley, D. J.; Pitzer, K. S., Thermodynamics of Electrolytes .12. Dielectric Properties of Water and Debye-Huckel Parameters to 350-Degrees-C and 1-Kbar. *J Phys Chem-Us* **1979,** *83* (12), 1599-1603.
120. Uematsu, M.; Franck, E. U., Static Dielectric-Constant of Water and Steam. *Journal of Physical and Chemical Reference Data* **1980,** *9* (4), 1291-1306.
121. Archer, D. G.; Wang, P. M., The Dielectric-Constant of Water and Debye-Huckel Limiting Law Slopes. *Journal of Physical and Chemical Reference Data* **1990,** *19* (2), 371-411.
122. Djamali, E. An experimental and theoretical study of the thermodynamic properties of aqueous electrolytes at very high temperatures and pressures. University of California, San Diego and San Diego State University, 2005.
123. Plummer, L. N.; Busenberg, E., The Solubilities of Calcite, Aragonite and Vaterite in Co2-H2o Solutions between 0-Degrees-C and 90-Degrees-C, and an Evaluation of the Aqueous Model for the System Caco3-Co2-H2o. *Geochimica Et Cosmochimica Acta* **1982,** *46* (6), 1011-1040.
124. Benezeth, P.; Dandurand, J. L.; Harrichoury, J. C., Solubility product of siderite (FeCO3) as a function of temperature (25-250 degrees C). *Chemical Geology* **2009,** *265* (1-2), 3-12.

125. Greenberg, J.; Tomson, M., Precipitation and Dissolution Kinetics and Equilibria of Aqueous Ferrous Carbonate Vs Temperature. *Appl Geochem* **1992,** *7* (2), 185-190.
126. Braun, R. D., Solubility of Iron(Ii) Carbonate at Temperatures between 30 and 80-Degrees. *Talanta* **1991,** *38* (2), 205-211.
127. Johnson, J. W.; Oelkers, E. H.; Helgeson, H. C., Supcrt92 - a Software Package for Calculating the Standard Molal Thermodynamic Properties of Minerals, Gases, Aqueous Species, and Reactions from 1-Bar to 5000-Bar and 0-Degrees-C to 1000-Degrees-C. *Comput Geosci* **1992,** *18* (7), 899-947.
128. Kharaka, Y. K. G., W. D.; Aggarwal, P. K.; Perkins, E. H.; DeBraal, J. D., SOLMINEQ.88; a computer program for geochemical modeling of water-rock interactions. U.S. Geological Survey: 1988.
129. Ziemniak, S. E.; Jones, M. E.; Combs, K. E. S., Magnetite Solubility and Phase-Stability in Alkaline Media at Elevated-Temperatures. *J Solution Chem* **1995,** *24* (9), 837-877.
130. Tremaine, P. R.; Leblanc, J. C., The Solubility of Magnetite and the Hydrolysis and Oxidation of Fe2+ in Water to 300-Degrees-C. *J Solution Chem* **1980,** *9* (6), 415-442.
131. Sweeton, F. H.; Baes Jr, C. F., The solubility of magnetite and hydrolysis of ferrous ion in aqueous solutions at elevated temperatures. *The Journal of Chemical Thermodynamics* **1970,** *2* (4), 479-500.
132. Ryzhenko, B., Determination of dissociation constants of carbonic acid and the degree of hydrolysis of the CO3 and HCO3 ions in solutions of alkali carbonates and bicarbonates at elevated temperatures. *Geochemistry* **1963,** *1963*, 151-164.
133. Read, A. J., First Ionization-Constant of Carbonic-Acid from 25 to 250 Degreesc and to 2000 Bar. *J Solution Chem* **1975,** *4* (1), 53-70.
134. Patterson, C. S.; Slocum, G. H.; Busey, R. H.; Mesmer, R. E., Carbonate Equilibria in Hydrothermal Systems - 1st Ionization of Carbonic-Acid in Nacl Media to 300-Degrees-C. *Geochimica Et Cosmochimica Acta* **1982,** *46* (9), 1653-1663.
135. Chen, X. M.; Gillespie, S. E.; Oscarson, J. L.; Izatt, R. M., Calorimetric Determination of Thermodynamic Quantities for Chemical-Reactions in the System Co2-Naoh-H2o from 225-Degrees to 325-Degrees-C. *J Solution Chem* **1992,** *21* (8), 825-848.
136. Li, D. D.; Duan, Z. H., The speciation equilibrium coupling with phase equilibrium in the H2O-CO2-NaCl system from 0 to 250 degrees C, from 0 to 1000 bar, and from 0 to 5 molality of NaCl. *Chemical Geology* **2007,** *244* (3-4), 730-751.
137. Patterson, C. S.; Busey, R. H.; Mesmer, R. E., 2nd Ionization of Carbonic-Acid in Nacl Media to 250-Degrees-C. *J Solution Chem* **1984,** *13* (9), 647-661.
138. Sharygin, A. V.; Wood, R. H., Densities of aqueous solutions of sodium carbonate and sodium bicarbonate at temperatures from (298 to 623) K and pressures to 28 MPa. *J Chem Thermodyn* **1998,** *30* (12), 1555-1570.
139. Templeton, C. C., Solubility of Barium Sulfate in Sodium Chloride Solutions from 25° to 95° C. *Journal of Chemical & Engineering Data* **1960,** *5* (4), 514-516.
140. Blount, C. W., Barite Solubilities and Thermodynamic Quantities up to 300-Degrees-C and 1400-Bars. *Am Mineral* **1977,** *62* (9-10), 942-957.
141. Jiang, C. F., Solubility and solubility constant of barium sulfate in aqueous sodium sulfate solutions between 0 and 80 degrees C. *J Solution Chem* **1996,** *25* (1), 105-111.
142. Malinin, S. D. U., N. Ye.; Khitarov, N. I., *Geokhimlya* **1969,** *8* 927.
143. Djamali, E.; Chen, K.; Murray, R. C.; Turner, P. J.; Cobble, J. W., Standard State Thermodynamic Properties of Ba2+(aq), Co2+(aq), and Cu2+(aq) up to 598.15 K, and Temperature Effect on Ligand Field. *J Phys Chem B* **2009,** *113* (8), 2404-2408.
144. Djamali, E.; Chen, K.; Cobble, J. W., Standard State Thermodynamic Properties of Completely Ionized Aqueous Sodium Sulfate Using High Dilution Calorimetry up to 598.15 K. *J Phys Chem B* **2009,** *113* (34), 11688-11695.

145. Pitzer, K. S.; Peiper, J. C.; Busey, R. H., Thermodynamic Properties of Aqueous Sodium-Chloride Solutions. *Journal of Physical and Chemical Reference Data* **1984,** *13* (1), 1-102.
146. Boublik, T., Hard-Sphere Equation of State. *J Chem Phys* **1970,** *53* (1), 471-&.
147. Mansoori, G.; Carnahan, N.; Starling, K.; Leland Jr, T., Equilibrium thermodynamic properties of the mixture of hard spheres. *The Journal of Chemical Physics* **1971,** *54*, 1523.
148. Chen, S. S.; Kreglewski, A., Applications of the Augmented van der Waals Theory of Fluids.: I. Pure Fluids. *Berichte der Bunsengesellschaft für physikalische Chemie* **1977,** *81* (10), 1048-1052.
149. Carnahan, N. F.; Starling, K. E., Equation of State for Nonattracting Rigid Spheres. *J Chem Phys* **1969,** *51* (2), 635-&.
150. Michelsen, M. L.; Hendriks, E. M., Physical properties from association models. *Fluid Phase Equilibr* **2001,** *180* (1-2), 165-174.

APPENDIX – 7.2

Glossary of symbols

A	Helmholtz free energy
A_1	Helmholtz free energy of first-order perturbation term
A_2	Helmholtz free energy of second-order perturbation term
$a_j(m)$	functions defined by eqs A.18
$b_j(m)$	functions defined by eqs A.14 and A.15
d_i	temperature-dependent segment diameter
g^{hc}	average radial distribution function of hard-chain fluid
$g^{hc}_{\alpha\beta}$	site-site radial distribution function of hard-chain fluid
I_1, I_2	abbreviations defined by eqs A.14-17
k	Boltzmann constant
k_{ij}	binary interaction parameter
m	number of segments per chain
$\overline{m}$	mean segment number in the system, defined in eq 6
M_i	number of association sites per molecule
N	total number of molecules
P	pressure
R	gas constant
r	radial distance between two segments
T	temperature
$\overline{v^{\infty}}$	partial molar volume at infinite dilution

x_i	mole fraction of component i
X^{Ai}	the mole fraction of molecules that are not bonded at site A
Z	compressibility factor

Greek Letters

ε	depth of pair potential
η	packing fraction, $\eta = \zeta_3$
μ	chemical potential
μ_D	dipole moment
μ_{red}	reduced dipole moment
ρ	total number density of molecules
σ	segment diameter
ζ_n	abbreviation (n=0, ..., 3) defined by eqs 6 and A.3

Superscripts

assoc	contribution due to dispersive association
CC	contribution due to ion-ion interaction in MSA
CD	contribution due to ion-dipole interaction in MSA
DD	contribution due to dipole-dipole interaction in MSA
disp	contribution due to dispersive attraction
exp	experimental property

hc	residual contribution of hard-chain system
hs	residual contribution of hard-sphere system
id	ideal gas contribution
NPMSA	contribution due to mean spherical approximation
polar	property at saturation condition
res	residual property
Sim	simulation result

Subscripts

ion	refers to ion
solv	refers to solvent (water)

Equations related to free energy and dispersion theory

In PC-SAFT formulation, the residual Helmholtz free energy A^{res} is written as a sum of following contributions[33]

$$A^{res} = A - A^{id} = A^{hs} + A^{disp} + A^{chain} + A^{assoc} \quad \text{A.1}$$

The compressibility factor can be written as

$$Z = Z^{id} (\equiv 1) + Z^{hs} + Z^{hc} + Z^{disp} + Z^{assoc} \quad \text{A.2}$$

The hard-sphere reference fluid contribution can be written in terms of equations from Boublik[146] and Carnahan et al[147] as

$$\frac{A^{hs}}{NkT} = \frac{1}{\zeta_0}\left[\frac{3\zeta_1\zeta_2}{(1-\zeta_3)} + \frac{\zeta_2^3}{\zeta_3(1-\zeta_3)^2} + \left(\frac{\zeta_2^3}{\zeta_3^2} - \zeta_0\right)\ln(1-\zeta_3)\right] \quad \text{A.3}$$

where ζ_n is term describing the density or packing of system and is defined as

$$\zeta_n = \frac{\pi}{6}\rho\sum_i x_i m_i d_i^n \qquad n \in \{0,1,2,3\} \quad \text{A.4}$$

where d_i is the temperature dependent diameter of segment of component *i* given by a Barker and Henderson[32] perturbation theory –

$$d_i(T) = \sigma_i\left[1 - 0.12\exp\left(-3\frac{\varepsilon_i}{kT}\right)\right] \quad \text{A.5}$$

For a mixture of hard spheres, the hard sphere contribution to the compressibility factor can be written as

$$Z^{hs} = \frac{\zeta_3}{(1-\zeta_3)} + \frac{3\zeta_1\zeta_2}{\zeta_0(1-\zeta_3)^2} + \frac{3\zeta_2^3 - \zeta_3\zeta_2^3}{\zeta_0(1-\zeta_3)^3} \quad \text{A.6}$$

For a hard sphere system governed by a modified square-well potential given by Chen and Kreglewski,[148] the radial distribution function for segments of component i is

$$g_{ij}^{hs} = \frac{1}{(1-\zeta_3)} + \left(\frac{d_i d_j}{d_i + d_j}\right)\frac{3\zeta_2}{(1-\zeta_3)} + \left(\frac{d_i d_j}{d_i + d_j}\right)^2 \frac{2\zeta_2^2}{(1-\zeta_3)^3} \qquad \text{A.7}$$

The hard chain reference contribution can be written as contributions from hard sphere terms from individual segments as

$$A^{hc} = \bar{m}A^{hs} - \sum_i x_i (m_i - 1)\ln g_{ii}^{hs}(\sigma_{ii}) \qquad \text{A.8}$$

where $\bar{m}$ is mean segment number in the mixture and is defined as

$$\bar{m} = \sum_i x_i m_i \qquad \text{A.9}$$

Similarly, the contribution to compressibility factor is given as

$$Z^{hc} = \bar{m}Z^{hs} - \sum_i x_i (m_i - 1)(g_{ii}^{hs})^{-1} \rho \frac{\partial g_{ii}^{hs}}{\partial \rho} \qquad \text{A.10}$$

The Helmholtz free energy contribution, A^{disp}, is given as a sum of first and second order perturbation contributions

$$\frac{A^{disp}}{NkT} = \frac{A_1}{NkT} + \frac{A_2}{NkT} \qquad \text{A.11}$$

Gross and Sadowski[33] derived a set of equations appropriate for square-well potential function

$$\frac{A^{disp}}{NkT} = -2\pi\rho I_1(\eta, \bar{m})\overline{m^2\varepsilon\sigma^3} - \pi\rho\bar{m}C_1 I_2(\eta, \bar{m})\overline{m^2\varepsilon^2\sigma^3} \qquad \text{A.12}$$

and

$$C_i = \left(1 + Z^{hc} + \rho\frac{\partial Z^{hc}}{\partial \rho}\right)^{-1} \qquad \text{A.13}$$

The value of $\mathbf{C_1}$ represents the compressibility of the hard chain fluid, I_1 (η,$\bar{m}$) and I_2 (η,$\bar{m}$) are power series in density where the coefficients are functions of the chain length and the packing fraction, η, which is equivalent to ζ_3 and are given as

$$I_1(\eta,\bar{m}) = \sum_{j=0}^{6} a_j(\bar{m})\eta^j \qquad \text{A.14}$$

$$I_2(\eta,\bar{m}) = \sum_{j=0}^{6} b_j(\bar{m})\eta^j \qquad \text{A.15}$$

$$\overline{m^2\varepsilon\sigma^3} = \sum_i\sum_j x_i x_j m_i m_j \left(\frac{\varepsilon_{ij}}{kT}\right)\sigma_{ij}^3 \qquad \text{A.16}$$

$$\overline{m^2\varepsilon^2\sigma^3} = \sum_i\sum_j x_i x_j m_i m_j \left(\frac{\varepsilon_{ij}}{kT}\right)^2\sigma_{ij}^3 \qquad \text{A.17}$$

Lorentz-Berthelot[60,61] combining rules are used for determining the parameters for a pair of unlike segments.

$$\sigma_{ij} = \frac{1}{2}\left(\sigma_i + \sigma_j\right) \qquad \text{A.18}$$

$$\varepsilon_{ij} = \sqrt{\varepsilon_i\varepsilon_j}\left(1-k_{ij}\right) \qquad \text{A.19}$$

The dispersion contribution to the compressibility factor is written as

$$Z^{disp} = -2\pi\rho\frac{\partial\eta I_1(\eta,\bar{m})}{\partial\eta}\overline{m^2\varepsilon\sigma^3} - \pi\rho\bar{m}\left[C_1\frac{\partial\left(\eta I_2(\eta,\bar{m})\right)}{\partial\eta} + I_2(\eta,\bar{m})\frac{\partial C_1}{\partial\eta}\right]\overline{m^2\varepsilon^2\sigma^3} \qquad \text{A.20}$$

The chemical potential can also be written as sum of contributions as

$$\mu_i^{res} = \mu_i^{hs} + \mu_i^{chain} + \mu_i^{disp} + \mu_i^{assoc} \qquad \text{A.21}$$

Alternately,

$$\frac{\mu_k^{res}}{RT} = \frac{A^{res}}{RT} + (Z-1) + \frac{1}{NkT}\left[\left(\frac{\partial A^{res}}{\partial x_k}\right)_{T,v,x_{i\neq k}} - \sum_{j=1}^{N}\left[x_i\left(\frac{\partial A^{res}}{\partial x_j}\right)_{T,v,x_{i\neq j}}\right]\right] \qquad \text{A.23}$$

The derivative of Carnahan-Starling[149] packing fraction term can written as

$$\zeta_{n,x_k}=\left(\frac{\partial\zeta_n}{\partial x_k}\right)_{T,\rho,x_{j\neq k}}=\frac{\pi}{6}\rho m_k\left(d_k\right)^n \qquad \text{A.24}$$

The derivative of the hard chain Helmholtz free energy can be obtained as

$$\left(\frac{\partial A^{hc}}{\partial x_k}\right)_{T,\rho,x_{j\neq k}}=m_k A^{hs}+\bar{m}\left(\frac{\partial A^{hs}}{\partial x_k}\right)_{T,\rho,x_{j\neq k}}-\sum_i x_i\left(m_i-1\right)\left(g_{ii}^{hs}\right)^{-1}\left(\frac{\partial g_{ii}^{hs}}{\partial x_k}\right)_{T,\rho,x_{j\neq k}} \qquad \text{A.25}$$

with

$$\left(\frac{\partial A^{hs}}{\partial x_k}\right)_{T,\rho,x_{j\neq k}}=-\frac{\zeta_{0,x_k}}{\zeta_0}A^{hs}+\frac{1}{\zeta_0}\left[\begin{array}{l}\dfrac{3\left(\zeta_{1,x_k}\zeta_2+\zeta_1\zeta_{2,x_k}\right)}{\left(1-\zeta_3\right)}+\dfrac{3\zeta_1\zeta_2\zeta_{3,x_k}}{\left(1-\zeta_3\right)^2}+\\ \dfrac{3\zeta_2^2\zeta_{2,x_k}}{\zeta_3\left(1-\zeta_3\right)^2}+\dfrac{\zeta_2^3\zeta_{3,x_k}\left(3\zeta_3-1\right)}{\zeta_3^2\left(1-\zeta_3\right)^3}+\\ \left(\dfrac{3\zeta_2^2\zeta_{2,x_k}\zeta_3-2\zeta_2^3\zeta_{3,x_k}}{\zeta_3^3}-\zeta_{0,x_k}\right)\ln(1-\zeta_3)+\\ \left(\zeta_0-\dfrac{\zeta_2^3}{\zeta_3^2}\right)\dfrac{\zeta_{3,x_k}}{\left(1-\zeta_3\right)}\end{array}\right] \qquad \text{A.26}$$

$$\left(\frac{\partial g^{hs}}{\partial x_k}\right)_{T,\rho,x_{j\neq k}}=\left[\begin{array}{l}\dfrac{\zeta_{3,x_k}}{\left(1-\zeta_3\right)^2}+\left(\dfrac{d_i d_j}{d_i+d_j}\right)\left(\dfrac{3\zeta_{2,x_k}}{\left(1-\zeta_3\right)^2}+\dfrac{6\zeta_2\zeta_{3,x_k}}{\left(1-\zeta_3\right)^3}\right)+\\ \left(\dfrac{d_i d_j}{d_i+d_j}\right)^2\left(\dfrac{4\zeta_2\zeta_{2,x_k}}{\left(1-\zeta_3\right)^3}+\dfrac{6\zeta_2^2\zeta_{3,x_k}}{\left(1-\zeta_3\right)^4}\right)\end{array}\right] \qquad \text{A.27}$$

The derivative of dispersion contribution to Helmholtz free energy can be derived as

$$\left(\frac{\partial A^{disp}}{\partial x_k}\right)_{T,\rho,x_{j\neq k}}=-2\pi\rho\left[I_{1,x_k}\overline{m^2\varepsilon\sigma^3}+I_1\overline{\left(m^2\varepsilon\sigma^3\right)}_{x_k}\right]-\pi\rho\left\{\begin{array}{l}\left[m_k C_1 I_2+\bar{m}C_{1,x_k}I_2+\bar{m}C_1 I_{2,x_k}\right]\\ \overline{m^2\varepsilon^2\sigma^3}+\bar{m}C_1 I_2\overline{\left(m^2\varepsilon^2\sigma^3\right)}_{x_k}\end{array}\right\} \qquad \text{A.28}$$

$$\overline{\left(m^2\varepsilon\sigma^3\right)}_{x_k}=2m_k\sum_i\sum_j x_j m_j\left(\frac{\varepsilon_{kj}}{kT}\right)\sigma_{kj}^3 \qquad \text{A.29}$$

$$\overline{\left(m^2\varepsilon^2\sigma^3\right)}_{x_k} = 2m_k\sum_i\sum_j x_j m_j\left(\frac{\varepsilon_{kj}}{kT}\right)^2\sigma_{kj}^3 \qquad \text{A.30}$$

The association chemical potential can be written as given by Michelsen et al.[150]

$$\frac{\mu_i^{assoc}}{RT} = \sum_{A_i}\ln X^{A_i} - \sum_k\sum_j\rho_k\rho_j\sum_{A_k}\sum_{B_j}X_{A_k}X_{B_j}\frac{\partial\Delta^{A_kB_j}}{\partial\rho_i} \qquad \text{A.31}$$

where the derivative of the association strength is written as

$$\left(\frac{\partial\Delta^{A_kB_j}}{\partial\rho_i}\right)_{T,\rho_{l\neq i}} = d_{kj}^3\left(\frac{\partial g_{kj}\left(d_{kj}\right)^{hs}}{\partial\rho_i}\right)_{T,\rho_{l\neq i}}\left[\exp\left(\frac{\varepsilon^{A_kB_j}}{kT}\right)-1\right]\kappa^{A_jB_k} \qquad \text{A.32}$$

and

$$\left(\frac{\partial g_{kj}(d_{kj})^{hs}}{\partial\rho_i}\right)_{T,\rho_{l\neq i}} = \frac{\pi N}{6}m_i\left\{\begin{array}{l}\dfrac{d_{ii}^3}{(1-\zeta_3)^2}+3\dfrac{d_{kk}d_{jj}}{d_{kk}+d_{jj}}\left[\dfrac{d_{ii}^2}{\left(1-\zeta_3\right)^2}+\dfrac{2d_{ii}^3\zeta_2}{\left(1-\zeta_3\right)^3}\right] \\ +2\left(\dfrac{d_{kk}d_{jj}}{d_{kk}+d_{jj}}\right)^2\left[\dfrac{2d_{ii}^2\zeta_2}{\left(1-\zeta_3\right)^3}+\dfrac{3d_{ii}^3\left(\zeta_3\right)^2}{\left(1-\zeta_3\right)^4}\right]\end{array}\right\} \qquad \text{A.33}$$

The association term contribution to the compressibility factor is then given as

$$Z^{assoc} = \sum_i x_i\frac{\mu_i^{assoc}}{RT} - \frac{A^{assoc}}{RT} \qquad \text{A.34}$$

With respect to the parameters defined in equations 12 and 13 of the report for the Semi-restricted non-primitive MSA,[53] further auxiliary parameters are defined as

$$\beta_3 = 1+\frac{b_2}{3} \qquad \text{A.35}$$

$$\beta_6 = 1-\frac{b_2}{6} \qquad \text{A.36}$$

$$\beta_{12} = 1+\frac{b_2}{12} \qquad \text{A.37}$$

$$\lambda = \frac{\beta_3}{\beta_6} \quad \text{A.38}$$

$$\Delta = \frac{b_1^2}{4} + \beta_6^2 \quad \text{A.39}$$

$$y_1 = \frac{\beta_6}{\beta_{12}^2} \quad \text{A.40}$$

$$D_F = 0.5\left(\beta_6\left(1+b_0\right) - \frac{b_1^2\sigma_{solv}}{12\sigma_{ion}}\right) \quad \text{A.41}$$

$$a_1 = \frac{1}{2D_F^2}\left(\Delta - 2D_F\beta_6\right) \quad \text{A.42}$$

$$a_2 = \frac{-b_1}{2\beta_6 D_F^2}\left(\frac{\Delta}{2} + D_F\beta_3\frac{\sigma_{ion}}{\sigma_{solv}}\right) \quad \text{A.43}$$

$$\Lambda = 0.5(1+b_0) + \frac{\beta_6\sigma_{solv}}{6\sigma_{ion}} \quad \text{A.44}$$

$$k_{10} = \frac{\sigma_{solv}}{\sigma_{ion}}\cdot\frac{b_1}{2\Delta}\left(1+a_1\Lambda\right) \quad \text{A.45}$$

$$k_{11} = 1 - \frac{1}{\Delta}\left(\beta_3 - a_2 b_1 \Lambda\frac{\sigma_{sol}}{2\sigma_{ion}}\right) \quad \text{A.46}$$

The equations are iteratively solved to obtain the MSA parameters b_0, b_1, and b_2 corresponding respectively to the ion-ion, ion-dipole, and dipole-dipole interactions. The excess Helmholtz free energy contributions due to ion-ion (A^{CC}), ion-dipole (A^{CD}), and dipole-dipole (A^{DD}) are given as

$$\frac{A^{CC}}{NkT} = \frac{1}{12\pi\rho\sigma_{ion}^3}\left(2d_0^2 b_0 - \left[Q_{ii}^{'}\right]^2\right) \quad \text{A.47}$$

$$\frac{A^{CD}}{NkT} = \frac{1}{12\pi\rho\sigma_{ion}^3}\left(-2d_0 d_1 b_0\frac{\sigma_{ion}}{\sigma_{solv}} - \left[1+\left(\frac{\sigma_{ion}}{\sigma_{solv}}\right)\right]\left(\frac{\sigma_{ion}}{\sigma_{solv}}\right)\left[Q_{id}^{'}\right]^2\right) \quad \text{A.48}$$

$$\frac{A^{DD}}{NkT}=\frac{-1}{12\pi\rho\sigma_{solv}^{3}}\left(\left[Q_{dd}^{'}\right]^{2}+2(q^{'})^{2}\right) \quad \text{A.49}$$

where the auxiliary parameters are defined as

$$Q_{ii}^{'}=-a_1-2+\frac{\beta_6}{D_F} \quad \text{A.50}$$

$$D=1+\frac{b_1^2}{4\beta_6^2} \quad \text{A.51}$$

$$Q_{id}^{'}=\frac{b_1}{\beta_6^2 D}\left[\beta_3+a_1\left(3\Lambda-2D_F\right)\right] \quad \text{A.52}$$

$$Q_{dd}^{'}=\frac{2}{\Delta}\left(\beta_3^2-\left(\frac{\sigma_{solv}}{2\sigma_{ion}}\right)b_1a_2\left(3\Lambda-2D_F\right)\right)-2 \quad \text{A.53}$$

$$q^{'}=\frac{b_2\left(1-\frac{b_2}{24}\right)}{\beta_{12}^2} \quad \text{A.54}$$

The Helmholtz free energy contribution due to MSA can then be written as

$$\frac{A^{npMSA}}{NkT}=\frac{A^{CC}}{NkT}+\frac{A^{CD}}{NkT}+\frac{A^{DD}}{NkT} \quad \text{A.55}$$

The chemical potential contribution of solvent due to electrostatic interactions can be written in terms of a reduced dipole moment defined as

$$\mu_{red}=\frac{\mu_D}{\sqrt{\left(kT\sigma_{solv}^{3}\right)}} \quad \text{A.56}$$

$$\mu_{solv}=\frac{-\mu_{red}^2}{3}\left(2b_2+\frac{d_0b_1\left(\frac{\sigma_{solv}}{\sigma_{ion}}\right)^2}{d_2}\right) \quad \text{A.57}$$